

Study of Perfluoropolymer as an Alignment Layer for Nematic Liquid Crystals

A Thesis submitted for the award of the degree of
Doctor of Philosophy in Physics

by

Tatipamula Arun Kumar

06PHPH11



School of Physics
University of Hyderabad
P.O. Central University
Hyderabad, India

March 2012

To
My Parents

Declaration

I, **Tatipamula Arun Kumar**, hereby declare that this thesis entitled “**Study of Perfluoropolymer as an Alignment Layer for Nematic Liquid Crystals**” submitted by me under the guidance and supervision of **Dr. Surajit Dhara** is a bonafide research work. I also declare that it has not been submitted previously in part or in full to this University or any other University or Institution for the award of any degree or diploma.

(Tatipamula Arun Kumar)
Reg. No. 06PHPH11.

Date:

Place: Hyderabad

Certificate

This is to certify that the thesis entitled “**Study of Perfluoropolymer as an Alignment Layer for Nematic Liquid Crystals**” submitted by **Tatipamula Arun Kumar** bearing Reg. No. 06PHPH11 in fulfillment of the requirements for the award of Doctor of Philosophy in Physics is a bonafide work carried out by him under my supervision and guidance.

This thesis has not been submitted previously in part or in full to this or any other University or Institution for the award of any degree or diploma.

Dr. Surajit Dhara
Thesis Supervisor.
School of Physics,
University of Hyderabad.

Dean,
School of Physics,
University of Hyderabad.

Acknowledgements

I am indebted to my supervisor Dr. Surajit Dhara for his continuous support during the course of my research work. His guidance, motivation and enthusiasm has immensely helped me all through. His meticulous planning in establishing experimental set up has influenced me much.

I would like to thank my Ph.D Doctoral Committee member, Professor V. S. S. Sastry, for his teaching, encouragement, insightful comments and thought provoking questions. I am also grateful to Professor K. P. N. Murthy for fruitful discussions.

I wish to thank Professor Madhusudana, for imbibing in me the mathematical skills in interpreting experimental results. His logical way of thinking fascinates me.

I would like to express my heartfelt thanks to Professor Hideo Takezoe and his group, for giving me an opportunity to work in his laboratory at Tokyo Institute of Technology, Japan.

I thank my lab-mate Sathyanarayana who extended his cooperation in setting up of several experiments. His vast knowledge in computer programming helped me a lot. I also thank Ananthaiah for his friendly support. I wish him all the best.

I would like to extend my warm thanks to all my other lab-mates Eswara Reddy, Madhuri, Venkata Sai and Uday for their assistance.

I am happy to acknowledge Dr. Trivikram Rao and Dr. Rajeshwari for their support and guidance.

Special thanks are due to my other group members Dr. Sai Preeti, Dr. Jayasri, Kamala Latha, Suman Kalyan, Siva and Regina Jose for their cheerful company.

I thank former Dean, Professor Vipin Srivatsava and present Dean, Professor C. Bansal, for providing needful facilities and all the other faculty members of School of Physics for their enlightening suggestions.

I want to express my gratitude to my good friend Devaraju and his family for their hospitality and endless support.

I thank Yugandhar, Sudha Nirmala, Anand and Dr. Cholleti Srinivas, for not only their excellent comments, but also for listening to me whenever I was excited about a new idea.

I extend my warm regards to my batch-mates Bheemalingam, Shankaraiah, Vaasu, Rambabu, Parthasarathy, Sadik Ali, Sita, Balaji, Vijayan, Venkaiah, Anil and Dr. Deepak, for their nice company.

I express my deep gratitude to my seniors, well wishers and friends.

I also thank Dr. Srinath and his students, Sendil and Suresh, for necessary support.

I am lucky to have friends like Ramaraju-Srujana, Chanakya, Namani

Srinivas, Mamatha Nagaraj, Sithara Pavithran, Malleshwari, Kavitha, Ajay, Venkata Ratnam, TRL Rao, Subbaiah, Chaitanya and Manohar Madeppa for their motivation and support.

I wish to thank Mrs. Hiromi Takahashi, Dr. Khoa Van Le, Guo Lingfeng, Satoshi Aya, Nirmalangshu Chakraborty, Rahul Deb and Maruthi Manoj who made my stay enjoyable at Tokyo Institute of Technology, Japan.

I thank T. Abraham, Shailaja, Prasad and other non-teaching staff for their help and support.

Financial support provided by University of Hyderabad and CAS-BSR is gratefully acknowledged. I also thank DST-PURSE grant for giving me an opportunity to attend 23rd International Liquid Crystal Conference, Krakow, Poland. Collaborative work carried out at Tokyo Institute of Technology, Japan through Global Center of Excellence (G-COE) program is gratefully acknowledged.

I also thank MAMA, my cousins Sathish, Praveen and Shyam Sunder, and my brother-in-laws Srinivas, Anjaneyulu and Devendhar. I also greatly acknowledge help from Gattu's family, and other family friends. I wish all the best to Chintu and Sony.

Last but the MOST, I would like to express my deep sense of gratitude to my parents and siblings, for their unconditional love and encouragement throughout.

Preface

Liquid crystal (LC) represents the state of matter in which the degree of molecular order is intermediate between the crystalline solid and isotropic liquid. Such intermediate phase exhibits solid like properties namely optical birefringence, anisotropic conductivity, dielectric and diamagnetic susceptibilities in addition to liquid like properties such as viscosity and surface tension. Liquid crystals are broadly divided into two types (i) thermotropic liquid crystals (ii) lyotropic liquid crystals. In thermotropic liquid crystals, the liquid crystalline phase is manifested by virtue of temperature whereas in lyotropic liquid crystals it is by concentration. In this thesis we study the alignment properties of mostly rod like and some bent core molecules on unconventional and conventional alignment layers.

The alignment of liquid crystal molecules on the treated surfaces of solid substrate is of great importance for the technological applications as well as basic understanding of the interfacial phenomena. The interfacial properties strongly influence the electro-optic properties of liquid crystal displays (LCDs). It is well known that weak anchoring of the liquid crystal director (the average alignment direction of the molecules) at the interface with appropriate alignment layer in principle can reduce the operating voltage and improve the steepness of the electro-optic response of LCDs. Uniform orientation of director is also essential to measure the physical properties of liquid crystals. The uniform orientation can be achieved by coating substrates with the appropriate aligning agents. In this thesis we have used perfluoropolymer as an aligning agent for liquid crystals.

Perfluoropolymer is a poly [perfluoro-(4-vinyloxy-1-butene)] (PPFVB), commercially known as CYTOP. It is used widely for antireflective coatings and in optical fibers because of its low refractive index ($n = 1.34$). It also has high transmittance over a wide wavelength range (200nm to 2 μ m). High solubility of CYTOP in fluorinated solvent makes it suitable for easy coating on substrate for various applications in photonics such as nano-imprint lithography (NIL), organic light-emitting diodes (OLEDs), lasing, and in

biological applications. It has been reported that the nematic liquid crystal 4'-butyl-4-heptyl-bicyclohexyl-4-carbonitrile (CCN-47) which has the negative dielectric anisotropy and exhibits anchoring transition i.e. the director changes its orientation from planar to homeotropic as the temperature decreases in CYTOP treated cells. By using this anchoring transition they have also demonstrated bistability in dye-doped liquid crystals. In case of smectics it was shown that CYTOP can also provide a shock-free homeotropic alignment of the director. The above interesting results opened up the opportunities to carry out further studies on anchoring transitions and alignment behavior of various liquid crystals in CYTOP treated cells. Hence, we have chosen CYTOP as an aligning agent for some liquid crystals throughout our work. This thesis comprises of seven chapters, of which the first chapter explains various types of liquid crystals and their physical properties. In second chapter much of the emphasis is laid on the preparation of cell and the measurement of cell thickness. In addition to that design and fabrication of a rubbing machine and a heater is also discussed in detail.

In third and fourth chapters we discuss the effect of electric field on the discontinuous anchoring transition and on the defects. Here we first show the observation of texture made under a optical polarizing microscope in the absence of an electric field. The compound (CCN-47) exhibits a planar texture with mostly $\pm 1/2$ strength and a few ± 1 strength defects when it is cooled below the isotropic to nematic transition temperature. As the temperature is lowered further some dark domains are nucleated at about 48°C in a few locations of the sample and spread with time even if the temperature is held fixed. In the dark domains the director is normal to the substrate, i.e., the alignment is homeotropic. Thus at the anchoring transition the director rotates by 90°, from planar to homeotropic, discontinuously. On further cooling to $\simeq 46^\circ\text{C}$, the entire texture turns completely dark. We studied the effect of electric field on the transition as well as on the textures. The variation of anchoring transition temperature, i.e., the temperature at which the nucleation of dark domain starts at some locations, is measured as a function of the applied field from the microscope observation. The anchoring transition temperature decreases with increasing electric field with

a change in slope at $E_{co} \simeq 0.1V/\mu m$, corresponding to the crossover from discontinuous to continuous anchoring transition. Below E_{co} , the transition is discontinuous from planar to homeotropic and the transition temperature decreases quadratically with the field. Above E_{co} , the transition is continuous from planar to tilted and the transition temperature decreases essentially linearly with rms field as shown in Figure 1.

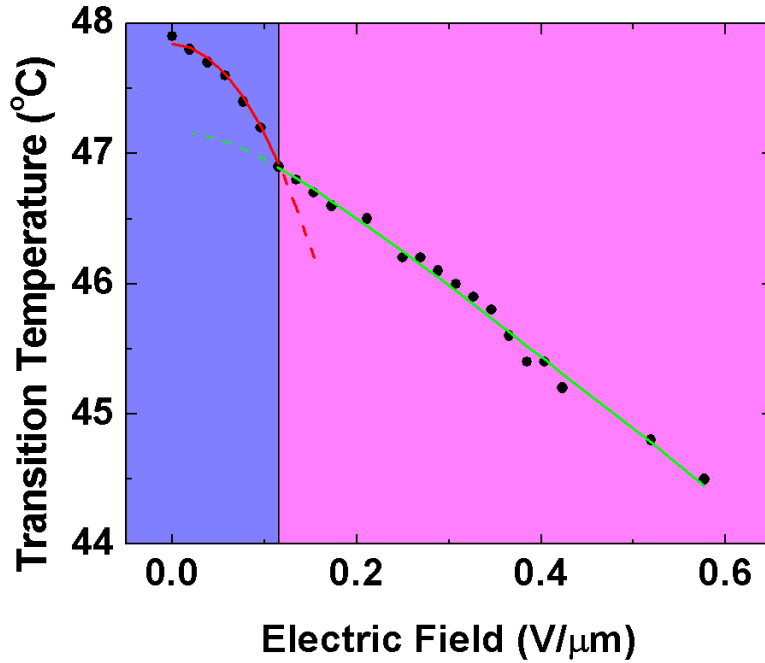


Figure 1: Variation of anchoring transition temperature with applied electric field. Continuous lines are best fit to the theoretical equations.

We developed a simple model to account for these results and show that the higher field regime corresponds to a temperature driven inverse Fredericksz transition in which the director orientation starts tilting at the weakly anchored surfaces while the tilt angle remains zero at the midplane of the cell as shown in Figure 2.

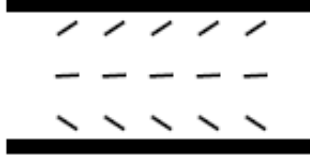


Figure 2: Schematic diagram illustrating the director orientations near the two surfaces and the midplane of the cell below the anchoring transition of type 2 corresponding to the odd solutions of $\psi(z)$.

The fourth chapter is the extension of the third chapter and describes the effect of electric field on defects in the same system i.e CCN-47 in CYTOP treated cells. Beyond the critical field (E_{co}) two like half-strength defects are merged to form integer strength (± 1) defects and two unlike half-strength defects get annihilated when the director tilts away from the planar alignment. The tilting occurs below the anchoring transition temperature under applied electric fields which are large enough to change the transition to a continuous one. We show that the defects of strength 1 which are seen just below this temperature have a new structure as shown in Figure 3, with either a + or a - point defect located at the midplane of the sample, and associated with two boojums lying at the two surfaces. Their number density decreases as the temperature is reduced. At a temperature $\sim 6^\circ$ below the anchoring transition temperature, the application of a sufficiently large field leads to the formation of umbilics. We also find that these field-induced defects follow the dynamic scaling laws found earlier for both umbilic and schlieren defects near the nematic-isotropic transition temperature.

The fifth chapter describes the anchoring transition in the same nematic liquid crystal (CCN-47) doped with chiral dopants. We have used several chiral dopants such as CB15, S811 and d-2. The first two chiral dopants are obtained from Merck Ltd., Japan and d-2 is an imine-based chiral dopant. We have prepared several cholesteric liquid crystals by adding chiral dopants in various concentrations. We noticed that these cholesteric liquid crystals also show anchoring transition in CYTOP treated cells. The coexistence of fan shape and finger print texture in a nematic liquid crystal added with

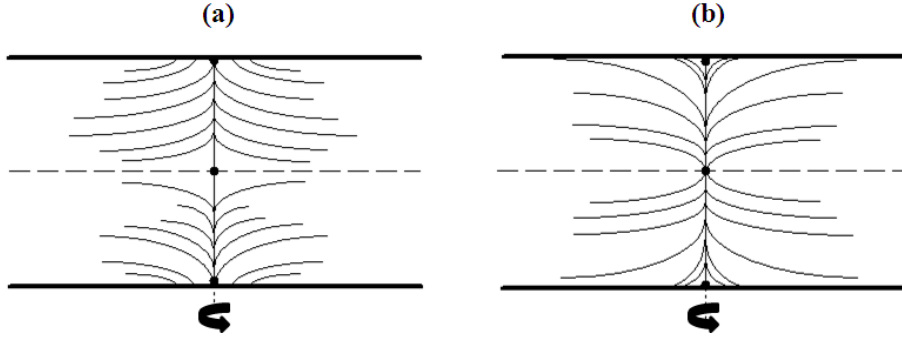


Figure 3: (a) Schematic representation of two possible director configurations with opposite tilts at the two surfaces in the case of +1 defect.

0.5 wt% of d-2 is shown in Figure 4(a). As the sample is cooled further the finger print texture turns to homeotropic state as shown in Figure 4(b). This means that the director changes its orientation from tilted to homeotropic. As a result the helix of cholesteric liquid crystal changes below the anchoring transition temperature.

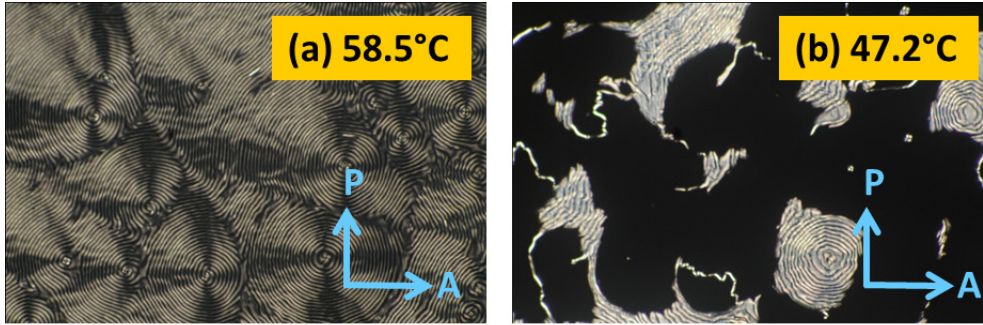


Figure 4: Photomicrographs showing textures of CCN-47 doped with 0.5wt% of d-2 (a) the coexistence of fan shape and finger print texture at temperature 57°C (b) transition from finger print texture to homeotropic state 47.2°C.

We also measured the helical twisting power (HTP) of d-2 by measuring the pitch of the cholesteric phase made of various concentrations of chiral dopants with CCN-47. We found $HTP \simeq 70\mu m^{-1}$ which is almost half the

	$A(\times 10^{-4} \text{ J/m}^2)$	α (deg)	γ_1 (Pa s)
CYTOP	1.0	2	0.08
AL-1254	18.3	1	0.10

Table 1: Summary of the physical properties of ZLI-2293 on both alignment layer, CYTOP and AL-1254.

value found in 4'-hexyloxy-4-biphenylcarbonitrile (6OCB) liquid crystal host. In the sixth chapter we discuss the measurement of some surface and bulk properties such as anchoring energy (A), pretilt angle (α) and rotational viscosity (γ_1) of a room temperature nematic liquid crystal mixture (ZLI-2293) in CYTOP treated cells and compared the results with AL-1254 treated cells. We first discuss the experimental techniques of the above measurements in detail in this chapter. We found that the pretilt angle and rotational viscosities are comparable on both the alignment layers. On the other hand the anchoring energy of ZLI-2293 on CYTOP is almost 18 times less than on AL-1254. Table 1 represents the summery of the results on both alignment layers. The low anchoring energy is attributed to the low surface free energy and is supported by the fact that CYTOP provides larger contact angle than the other alignment layers for liquid crystals.

The seventh chapter deals with the alignment properties of some unconventional nematic liquid crystals such as bent-core, T-shaped and hockey stick-shaped molecules on planar (AL-1254) and homeotropic (JALS-204, SE-1211) alignment layers. Irrespective of the sign of dielectric anisotropy ($\Delta\epsilon$) and molecular structure, uniform planar alignment of the director is observed in AL-1254 coated cells whereas no stable homeotropic alignment of bent-core compounds with $\Delta\epsilon < 0$ is observed in cells coated with JALS-204 or SE-1211. Alignment properties of these two types ($\Delta\epsilon > 0$ and $\Delta\epsilon < 0$) of unconventional nematic liquid crystals are explained considering the steric, short-range dipolar and long-range van der Waals interactions at the interface. A bent-core compound ($\Delta\epsilon < 0$) which has no higher-order liquid crystalline phase except for the nematic exhibits a narrow temperature range of homeotropic state (on JALS-204) while cooling from the isotropic phase

followed by an anchoring transition to a planar state as the temperature is further lowered. The measured polar anchoring energy of this compound on JALS-204 is significantly lower than many known calamitic liquid crystals and is responsible for the anchoring transition observed.

Contents

List of Figures	xxv
------------------------	------------

1 Introduction	1
1.1 Liquid Crystals	1
1.2 Classification of Liquid Crystals	1
1.3 Some Common Liquid Crystalline Phases	2
1.3.1 Nematic Phase	2
1.3.2 Cholesteric Phase	3
1.3.3 Smectic Phase	4
1.3.4 Smectic A Phase	4
1.3.5 Smectic C Phase	4
1.3.6 Smectic C* Phase	5
1.4 Bent-Core Liquid Crystals	6
1.5 Defects in Nematic Liquid Crystals	6
1.6 Umbilic defects	8
1.7 Properties of Nematic Liquid Crystals	10
1.7.1 Orientational Order Parameter	10
1.7.2 Birefringence	11
1.7.3 Dielectric Constant	12
1.7.4 Curvature Elasticity	14
1.7.5 Pretilt Angle	15
1.7.6 Anchoring Energy	15

1.7.7	Rotational Viscosity	16
1.8	Alignment of Liquid Crystals	17
1.8.1	Freedericksz' transition in nematic liquid crystal with strong surface anchoring	17
	References	19
2	Instrumentation	23
2.1	Introduction	23
2.2	Preparation of Liquid Crystal Cell	23
2.3	Design and Construction of Rubbing machine	26
2.4	Design and Construction of Heater for sample preparation . .	27
2.5	Measurement of Cell Thickness	28
3	Temperature and electric field induced inverse Freedericksz transition in a nematogen with weak surface anchoring	31
3.1	Introduction	31
3.2	Experimental	36
3.3	Results and Discussion	36
3.4	Conclusions	50
	References	50
4	Effect of an electric field on defects in a nematic liquid crystal with variable surface anchoring	55
4.1	Introduction	55
4.2	Experimental	57
4.3	Results and Discussion	57

CONTENTS

4.3.1	Textures without an electric field	57
4.3.2	Textures with electric field	59
4.3.3	Dynamics of umbilic defects	67
4.4	Conclusions	73
	References	73
5	Anchoring transition in a nematic liquid crystal doped with chiral agents	79
5.1	Introduction	79
5.2	Experimental	83
5.3	Results and Discussion	84
5.3.1	CLCs doped with CB15	84
5.3.2	CLCs doped with S811	91
5.3.3	CLCs doped with d-2	95
5.4	Conclusions	101
	References	102
6	Perfluoropolymer as planar alignment layer for liquid crystal mixtures	105
6.1	Introduction	105
6.2	Experimental	106
6.2.1	Measurement of Polar Anchoring Energy	106
6.2.2	Measurement of Pretilt Angle:	109
6.2.2.1	Incident Angle Correction	110
6.2.3	Measurement of Rotational Viscosity	112

CONTENTS

6.3	Results and Discussion	114
6.4	Conclusions	124
	References	124
7	Alignment of unconventional nematic liquid crystals	127
7.1	Introduction	127
7.2	Experimental	129
7.3	Results and Discussion	131
7.4	Conclusions	142
	References	142
	List of Publications	147
	Curriculum Vitae	149

List of Figures

1	Variation of anchoring transition temperature with applied electric field. Continuous lines are best fit to the theoretical equations.	xv
2	Schematic diagram illustrating the director orientations near the two surfaces and the midplane of the cell below the anchoring transition of type 2 corresponding to the odd solutions of $\psi(z)$	xvi
3	(a) Schematic representation of two possible director configurations with opposite tilts at the two surfaces in the case of +1 defect.	xvii
4	Photomicrographs showing textures of CCN-47 doped with 0.5wt% of d-2 (a) the coexistence of fan shape and finger print texture at temperature 57°C (b) transition from finger print texture to homeotropic state 47.2°C.	xvii
1.1	Schematic representation of molecular arrangement in the calamitic nematic phase.	2
1.2	Schematic representation of molecular arrangement in the cholesteric phase. The arrows indicate the orientation of director \hat{n}	3
1.3	Schematic representation of the molecular arrangement in the Smectic A phase.	4
1.4	Schematic representation of the molecular arrangement in the smectic C phase. The molecules are tilted with respect to the layer normal \hat{k}	5
1.5	Schematic representation of molecular arrangement in the SmC* phase. The tilt direction rotates between successive layers as represented by arrows.	5

LIST OF FIGURES

1.6	The chemical structure of a typical bent-core liquid crystal [10].	6
1.7	Director configurations of some defects.	8
1.8	Director configurations of various umbilic defects (a) side view (b) top view.	9
1.9	Schematic representation of optical indicatrix of a uniaxial system.	11
1.10	A schematic representation of parallel (ϵ_{\parallel}) and perpendicular (ϵ_{\perp}) components of dielectric constant of a nematic. The molecule is assumed to possess a dipole moment μ at an angle β with its long axis giving the longitudinal μ_l and transverse μ_t components. The measuring electric field E can be either parallel ($E \parallel \hat{n}$) or perpendicular ($E \perp \hat{n}$) to the director. . . .	13
1.11	A Schematic representation of the splay, twist and bend de- formations.	14
1.12	Schematic representation of pretilt angle (α) of liquid crystals on a substrate surface.	15
1.13	Schematic representation of surface anchoring of liquid crystal on a substrate surface.	16
1.14	Schematic representation of homogeneous and homeotropic alignment of the director on ITO substrates.	18
1.15	Schematic representation of director configuration is shown (a) below and (b) above the threshold field respectively.	19
2.1	Photograph of patterned sticker and schematic diagram of glass plate with patterned ITO.	24
2.2	photographs of (a) spin coater, (b) optical adhesive and (c) ultrasonic soldering unit.	25
2.3	Schematic diagram and a photograph of LC cell made up of ITO glass plates.	25

LIST OF FIGURES

2.4	Drawing of the rubbing machine.	26
2.5	Photograph of rubbing machine.	27
2.6	Photograph of a heater.	28
2.7	Schematic diagram of the Ocean optic spectrometer.	29
3.1	Variation of tilt angle as a function of temperature as determined from the intensity data. The insert is a semi-log plot of tilt angle against the square root of the reduced temperature. Here T_c correspond to the onset of the homeotropic transition temperature. (adopted from ref. [7]).	32
3.2	The Chemical structures of: (a) CCN-47 and (b) perfluoropolymer.	34
3.3	Photomicrographs of the textures showing anchoring transitions in CCN-47 under crossed polarizers (white crossed arrows): (a) CCN-47 at 50°C; (b) CCN-47 during the discontinuous anchoring transition; (c) CCN-47 at 40°C (adopted from ref. [14]).	34
3.4	(a) Transmitted light intensity of an orientated sample of CCN-47 between crossed polarizers as a function of temperature. (b) Calculated birefringence obtained from (a). Data for cooling and heating processes are shown by squares and circles, respectively. A large hysteresis in temperature is observed. Data corresponding to triangles are measured using homogeneous alignment agent AL-1254, which shows no anchoring transition (adopted from ref. [14]). It may be mentioned that a small shift in the NI transition temperature is due to uncalibrated heater. The correct temperature is reported in ref. [15].	35

3.5	Photomicrographs of the textures around the anchoring transition temperature in CCN-47 between crossed polarizers, at (a) 52.2°C (b) 48°C (c) 46°C., all under zero field. Textures in the same region under an electric field of $0.29\text{V}/\mu\text{m}$, as photographed at (d) 47.2°C (e) 46.8°C (f) 29°C. White dotted lines in Figure 3.5(d) enclose a domain with tilted director. Thickness of the cell is $5.2\ \mu\text{m}$	38
3.6	Schematic drawings of (a) the sideview and (b) the topview (say in the upper half of the cell) of the director orientation across boundary between the untilted and tilted regions. In (b) the length of the line is a measure of the projection of the director in the plane of the plate. Regions in (I) and (III) represent tilted and (II) and (IV) represent planar director orientations. (c) Part of the texture taken from Figure 3.5(e) including a half-defect connected by a inversion wall and the superimposed director orientations across the boundary between the regions with tilted and planar alignments of the director.	41
3.7	Variation of anchoring transition temperature with applied electric field. Continuous lines are best fit to the theoretical equation 3.4 and equation 3.13 with fit parameter $u = 1.6 \times 10^{-6}\text{J}/\text{m}^2\text{K}$. The type 2 and type 1 transitions, shown by the dashed lines are superceded by transitions of the other type occuring at a higher temperatures.	44
3.8	Schematic diagram illustrating the director orientations near the two surfaces and the midplane of the cell below the anchoring transition of type 2 corresponding to (a) the even and (b) the odd solutions of $\psi(z)$	44
4.1	(a) Photomicrographs of the texture at 52.2°C (b) during discontinuous anchoring transition at 47.5°C (c)homeotropic texture at 45.4°C. All the above observations were made in the absence of an electric field in a $5.2\ \mu\text{m}$ thick cell.	58

LIST OF FIGURES

- 4.2 Photomicrographs showing discontinuous anchoring transition on heating the sample from homeotropic state (a) homeotropic texture at 50°C (b) during the discontinuous anchoring transition at 50.6°C (c) planar texture at 52.4°C and (d) at 54.2°C. All the above observations were made in the absence of an electric field a 5.2 μm thick cell. 59
- 4.3 Photomicrographs showing anchoring transition under an applied ac voltage of 0.9V (above cross-over field) and frequency 3.11 KHz during cooling (a) at 52.6°C (b) showing a continuous anchoring transition at 46.6°C (c) at 46.4°C (d) dark field of view with a few four brush defects at 31.9°C. Cell thickness 5.2 μm 61
- 4.4 Schematic representation of director orientations of a +1 defect line: (a) top view (b) side view. 62
- 4.5 Schematic representation of director orientations in the top view of a -1 disclination line. 62
- 4.6 Merging of $\pm 1/2$ defects under the applied ac voltage of 1.5V (a) pairs of half-strength defects are shown with enclosed dotted white lines at 44.1°C some of the half-strength defects have already merged to form integer-strength defects; (b) one pair of unlike defects (enclosed with dotted lines at the left) annihilated at 44°C (c) both the unlike and like half-strength defects approach each other (d) like half-strength defects merge to form an integer defect and unlike half-strength defects are annihilated. White wispy lines pointed by green arrows are inversion walls. 64
- 4.7 (a) Schematic representation of two possible director configurations with opposite tilts at the two surfaces in the case of +1 defect. 65

LIST OF FIGURES

4.8	Some cross sections of the director configuration of -1 disclination, with opposite tilts at the two surfaces.	66
4.9	Textures (at 42°C) showing umbilic defects under an applied voltage of amplitude 4V and frequency 3.11 KHz: elapsed time after the application of the field: (a) 1 sec (b) 7 sec (c) 13 sec (d) 25 sec; cell thickness $d = 5.2\mu m$	70
4.10	Schematic representation of director field of an umbilic defect of +1 strength generated by an electric field. Note the absence of boojums.	70
4.11	(a) Time evolution of defect density $\rho(t)$. The continuous line is the best fit to the theoretical equation 4.1 with the exponent $\nu = 1.1 \pm 0.05$. (b) Time evolution of defect pair separation $D(t)$. The continuous line is the best fit to the theoretical equation 4.2 with the exponent $\alpha = 0.55 \pm 0.01$	72
5.1	Schematic diagram showing various orientations of CLCs: (a)&(b) with planar boundary conditions and (c)&(d) with homeotropic boundary conditions [1].	80
5.2	Textures of cholesteric phase under planar anchoring conditions: (a) oily streaks texture with a pitch of $P = 2\mu m$, such that the colour observed is not due to selective reflection, (b) fan-like texture of a short pitch cholesteric phase (c) fan-shaped focal conic texture of a short pitch cholesteric phase (d) cholesteric polygonal (fingerprint) texture with a relatively long pitch, such that the helical N* superstructure is resolved by polarizing microscopy. (adopted from reference [5]).	81

LIST OF FIGURES

5.3	Textures of cholesteric phase under homeotropic anchoring conditions: (a) fingerprint texture owing to the identity period $L = P/2$ of the cholesteric phase, the pitch can be determined as twice the distance between two dark lines, (b) fingerprint texture with pitch P approaching the cell gap d (c) coexistence of a cholesteric fingerprint texture with so-called cholesteric fingers (bright lines in the center) and a pseudo-isotropic region with a homeotropic nematic director configuration (black) (d) sample with a diverging cholesteric pitch exhibiting so called cholesteric fingers. In the strongly distorted director configuration, the dark areas represent a pseudo-isotropic, homeotropically aligned nematic (adopted from reference [5]).	82
5.4	Chemical structures of chiral agents CB 15, S811 and d-2. . .	84
5.5	The evolution of textures in CCN-47 doped with 5wt% of CB15: (a) fan-shaped texture, (b)-(d) fan-shaped to finger print on cooling, and (e) and (f) finger print to fan-shaped on heating. Even in (a) fine fringes are seen (inset).	86
5.6	Photomicrographs of CCN-47 doped with 3wt% of CB15 on cooling: (a) planar state, (b) planar to tilting transition, (c) & (d) finger print texture with some homeotropic regions, (e) texture with more homeotropic regions, (f) homeotropic state with a few thin bright lines.	87
5.7	Photomicrographs of CCN-47 doped with 3wt% of CB15 on heating: (a) transition from homeotropic to finger print, (b)-(d) finger print texture, (e)&(f) finger print to tilted state, and (g)&(h) tilted state with reduced brightness.	88
5.8	Photomicrographs of CCN-47 doped with 5wt% of S811 on cooling: (a)-(c) Textures of fan like shape, (d)&(e) transition from fan-like shape to finger print, and (f)-(h) finger print to homeotropic state.	89

LIST OF FIGURES

5.9	Photomicrographs of CCN-47 doped with 5wt% of S811 on heating: (a) the transition from homeotropic to finger print texture, (b)-(e) finger print texture, (f) transition from finger print to tilted state, and (g&h) fan-like shape texture.	90
5.10	Photomicrographs of CCN-47 doped with 1wt% of S811 on cooling:(a)-(c) fan shape texture, (d)–(f) fan shape texture slowly changes to finger print texture, (g)&(h) transition from finger print to homeotropic state.	92
5.11	Photomicrographs showing alignment of CCN-47 doped with 1wt% of S811 in a CYTOP treated rubbed cell on cooling: (a) tilted state, (b) tilted state with increased brightness, (c) anchoring transition from planar to homeotropic state, (d&e) anchoring transition, and (f) homeotropic state.	93
5.12	Photomicrographs showing alignment of CCN-47 doped with 1wt% of S811 in a CYTOP treated rubbed cell on heating: (a) homeotropic state, (b)&(c) anchoring transition from homeotropic to planar state, and (d) tilted state with reduced brightness.	94
5.13	Textures with selective reflection on cooling in CYTOP treated rubbed cell with 5wt% of d-2: (a) isotropic to cholesteric phase transition, (b) selective reflection with Grandjean steps, (c) selective reflection of blue colour, (d) blue colour is changing to cyan, and (e)&(f) selective reflections in cyan colour.	96
5.14	Photomicrographs of CLCs made from 0.5wt% of d-2: (a) focal conic texture (b) a discontinuous anchoring transition from tilted to homeotropic occurs at 47.2°C on cooling, (c) anchoring transition from homeotropic to planar occurs at 53.0°C, and (d) tilted state.	97
5.15	Schematic illustration of the wedge cell for the determination of the pitch. Where S is the distance between two Grandjean lines and P is the pitch of the cholesteric.	97

LIST OF FIGURES

5.16	Photomicrographs of Grandjean steps observed in wedge cell with 5wt% concentration of d-2 in CCN-47. An arrow in the picture denotes the rubbing direction.	98
5.17	Variation of pitch (P) as a function of temperature for the concentration 5wt% of d-2.	99
5.18	Photomicrographs of Grandjean steps observed in wedge cell with 0.7wt% concentration of d-2 in CCN-47. An arrow in the picture denotes the rubbing direction.	99
5.19	Variation of pitch (P) as a function of temperature for the concentration 0.7wt% of d-2.	100
5.20	Variation of inverse of the pitch (P) as a function of molar fraction of d-2.	100
6.1	Propagation of incident light through air, glass and liquid crystal medium respectively.	111
6.2	Measurement of pretilt angle of 5CB in SE 7492 treated cells. The open circles represent the experimental data points and the solid line denotes the best fit to the equation 6.11.	111
6.3	Photograph of (a) bare and CYTOP coated ITO glass plates (b) transmission spectrum of bare and CYTOP coated ITO glass plates (adopted from reference [13]).	115
6.4	The green and red dots on the right corners of the ITO glass plates represents the coating of AL-1254 and CYTOP respectively.	115
6.5	The atomic force microscope pictures of CYTOP coated ITO glass plates: (a) before (b) after rubbing.	116
6.6	Photomicrographs of CYTOP coated cell with ZLI-2293 sample is at room temperature. An arrow in the picture denotes the rubbing direction (a) rubbing direction $\psi = 0^\circ$ and (b) rubbing direction $\psi = 45^\circ$	117

LIST OF FIGURES

6.7	Schematic diagram of experimental setup for measuring retardation and capacitance.	117
6.8	Photograph of experimental set up for measuring retardation and capacitance.	118
6.9	The variation of intensity as a function of voltage in CYTOP cell at room temperature.	118
6.10	Variation of normalized retardation (R/R_0) and the ratio of the sample capacitance to the empty cell capacitance (C/C_0) as a function of voltage in a CYTOP coated cell at room temperature.	119
6.11	The variation of R/R_0 versus $1/CV$ in AL-1254 and CYTOP coated cells at room temperature. The data are well fitted to equation 6.10.	119
6.12	Schematic diagram of pretilt angle measurement setup.	121
6.13	Photograph of experimental set up of pretilt angle measurement.	121
6.14	Transmitted intensity versus incident angle for ZLI-2293 in a CYTOP coated cell at room temperature. The circles represent the experimental data points and the solid line denotes the best fit to the equation 6.11.	122
6.15	The variation of intensity as a function of time in CYTOP cell at room temperature.	123
6.16	$\ln [\delta(0)/\delta(t)]$ versus time t for ZLI-2293 at room temperature. The open circles represent the experimental data for both alignment layers and the solid lines represent the best fit to the equation $\ln [\delta(0)/\delta(t)] = -2t/\tau_0$. Cell thickness $d = 9.5 \pm 0.5 \mu m$ (AL-1254) and $10.6 \pm 0.5 \mu m$ (CYTOP) respectively. . . .	123

LIST OF FIGURES

- 7.1 (a) Molecular structure and phase transition temperatures of compound C1 ($\Delta\epsilon > 0$). Textures observed in (b) planar and (c) homeotropic cells at a temperature 170°C. An arrow in Figure (b) denotes the rubbing directions. Cell thickness; 6.9 μm and 8 μm for planar and homeotropic cells respectively. . . 132
- 7.2 (a) Molecular structure and phase transition temperatures of compound C2 ($\Delta\epsilon > 0$) with hockey-stick shaped molecule. Textures observed in (b) planar and (c) homeotropic cells at a temperature 120 °C. An arrow in Figure (b) denotes the rubbing directions. Cell thickness; 7.1 μm and 4.2 μm for planar and homeotropic cells respectively. 133
- 7.3 (a) Molecular structure and phase transition temperatures of compound C3 ($\Delta\epsilon > 0$) with branched (T-shaped) molecules. Textures observed in (b) planar and (c) homeotropic cell at a temperature 117°C. An arrow in Figure (b) denotes the rubbing direction. Cell thickness: 5.2 μm and 6 μm for planar and homeotropic cells respectively. 134
- 7.4 (a) Molecular structure and phase transition temperatures of compound C4 ($\Delta\epsilon < 0$). Textures observed in (b) planar and (c),(d) homeotropic cells at a temperature 117°C. An arrow in Figure (b) denotes the rubbing directions. Cell thickness: 5.4 μm for planar and 5.7, 5.3 μm for homeotropic cells respectively. 135
- 7.5 (a) Molecular structure and phase transition temperatures of compound C5 ($\Delta\epsilon < 0$). Texture observed in (b) planar and (c), (d) homeotropic cells at a temperature 207°C. An arrow in Figure (b) denotes the rubbing direction. Cell thickness: 5.3 μm for planar and 4.5, 5 μm for homeotropic cells respectively. 136

LIST OF FIGURES

- 7.6 a) Molecular structure and phase transition temperatures of the compound C6 ($\Delta\epsilon < 0$). Textures observed in (b) planar and (c) homeotropic cell at 72°C. Arrow in Figure (b) denote the rubbing direction. Cell thickness: 7.1 μm for planar and 5.2 μm for homeotropic cells respectively. 137
- 7.7 Textures observed in homeotropic cell (JALS-204) at various temperatures when rubbing direction is parallel (a(i)-a(iv)) and rotated by 45° (b(i)-b(iv)) with respect to the polarizer. Arrows in the Figure denote the rubbing direction. Cell thickness: 5.2 μm . 138
- 7.8 Schematic representation of bent-core molecules. The direction of resultant dipole moment and the large polarisability directions are denoted by D and P respectively. (a) Both D and P are parallel in materials with $\Delta\epsilon > 0$ (b) D and P are mutually perpendicular in materials with $\Delta\epsilon < 0$. (c) Homeotropic alignment of the director with $\Delta\epsilon > 0$. (d) planar alignment of the director with $\Delta\epsilon < 0$ 140
- 7.9 a) Retardation as a function of applied voltage measured in the homeotropic cell (at 72°C) (b) sample capacitance as a function of applied voltage at 72°C. (c) normalized retardation R/R_o as a function of $1/CV_{rms}$ at 72°C. Continuous line is the theoretical fit to equation 7.1. Cell thickness; 6.1 μm 141

Introduction

1.1 Liquid Crystals

Organic compounds that exhibit the intermediate state of matter of crystalline solid and isotropic liquid are called Liquid Crystals (LCs). In 1888, an Austrian botanist Fredrich Reinitzer first observed this state of matter and later the name liquid crystal was suggested by Lehmann in 1889. This intermediate phase exhibits liquid like properties such as viscosity and surface tension. In addition to that they also exhibit solid like properties namely, optical birefringence, anisotropic conductivity, dielectric and diamagnetic susceptibilities [1, 2]. There are two types of liquid crystals *viz.*, thermotropic and lyotropic. In thermotropic, the liquid crystalline phase is manifested by virtue of temperature whereas in lyotropic, it is by concentration [3, 4]. In this thesis we study the alignment properties of some thermotropic liquid crystals on unconventional and conventional alignment layers.

1.2 Classification of Liquid Crystals

Shape anisotropy is an essential requirement for exhibiting liquid crystalline phase. Depending on the shape of the constituent molecules, thermotropic liquid crystals are classified into three categories [5, 6]:

- Calamitic liquid crystals: made of rod like molecules
- Discotic liquid crystals: made of disc like molecules
- Bent-core liquid crystals: made of bent-shape molecules

1.3 Some Common Liquid Crystalline Phases

1.3.1 Nematic Phase

Nematic (N) is the simplest phase among all known liquid crystalline phases. Molecules in this phase exhibit long range orientational order and the center of mass of the molecules are randomly distributed. In calamitic nematic, on an average the long axes of the molecules point in a particular direction as shown schematically in Figure 1.1. This direction is represented by a dimensionless unit vector called director (\hat{n}). The director \hat{n} is apolar i.e \hat{n} and $-\hat{n}$ are physically indistinguishable [1]. Some discotic and bent-core liquid crystals also exhibit nematic phase.

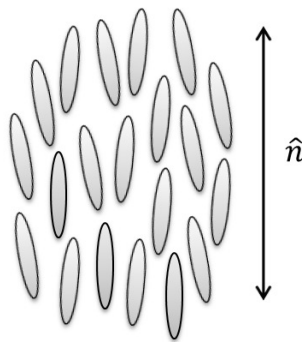


Figure 1.1: Schematic representation of molecular arrangement in the calamitic nematic phase.

1.3 Some Common Liquid Crystalline Phases

1.3.2 Cholesteric Phase

Cholesteric phase (N^*) is formed when the constituents of the liquid crystal molecules are either intrinsically chiral or chiral dopants are added to nematic. The chirality of the system leads to a helical distortion, in which the director \hat{n} rotates continuously in space along the z -direction with a spatial period of π/p . Here p is the pitch of the cholesteric helix which can be right or left handed, and strongly depends on temperature. A schematic representation of orientation of director \hat{n} is shown schematically in Figure 1.2. The pitch of common cholesterics is of the order of a several thousands Angstroms (\AA), and is comparable to the wavelength of visible light.

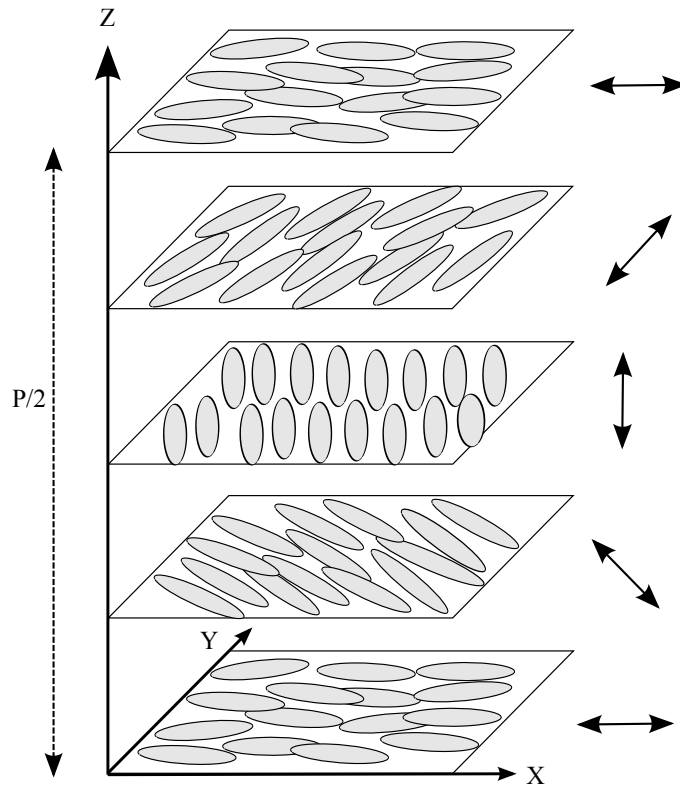


Figure 1.2: Schematic representation of molecular arrangement in the cholesteric phase. The arrows indicate the orientation of director \hat{n} .

1.3.3 Smectic Phase

In smectic liquid crystals the molecules are arranged in layers and possess one degree of translational order. There are several types of smectic liquid crystals depending on the molecular arrangement within the layer.

1.3.4 Smectic A Phase

In smectic A (SmA), the average orientation of the long axes of the molecules is along the layer normal whereas the centers of the molecules in each layer are arranged randomly as shown schematically in Figure 1.3. It can be considered as a one-dimensional crystal and two-dimensional liquid.

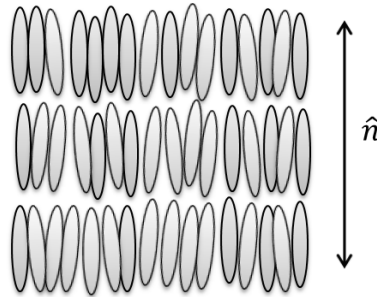


Figure 1.3: Schematic representation of the molecular arrangement in the Smectic A phase.

1.3.5 Smectic C Phase

Smectic C (SmC) is similar to smectic A except that the molecules are tilted with respect to the layer normal as shown schematically in Figure 1.4. This tilted orientation gives rise to optical biaxiality of the smectic C phase.

1.3 Some Common Liquid Crystalline Phases

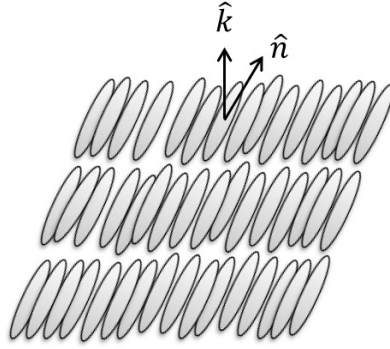


Figure 1.4: Schematic representation of the molecular arrangement in the smectic C phase. The molecules are tilted with respect to the layer normal \hat{k} .

1.3.6 Smectic C* Phase

If a smectic C phase is composed of chiral molecules, the chiral interactions lead to the formation of helical structure and the phase is called Smectic C* (SmC^*). The helix is formed by precession of the tilt direction about an axis perpendicular to the layers with a characteristic pitch as shown schematically in Figure 1.5. The helix can be either right or left handed depending on the

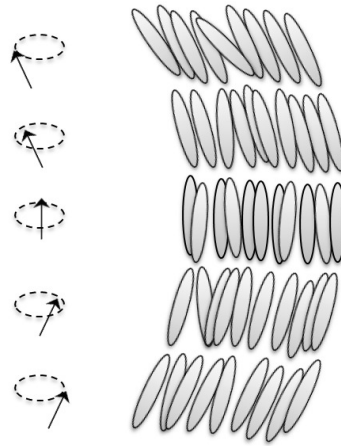


Figure 1.5: Schematic representation of molecular arrangement in the SmC^* phase. The tilt direction rotates between successive layers as represented by arrows.

chirality of the constituent molecules. The helix of the smectic C* can be unwound either by surface interactions or by the application of strong electric or magnetic fields.

1.4 Bent-Core Liquid Crystals

Bent core liquid crystals were first synthesized by Vorlander [7]. Initially these molecules were termed as "Bad Rods" and the liquid crystals were not characterized further. In 1996 Niori *et al.* [8] first observed ferroelectric switching behavior in a compound composed of achiral bent-core molecules. The bent-core molecules are strongly polar and biaxial in shape and thus deviate from the cylindrical symmetry. Bent-core molecules exhibit a new class of liquid crystalline phases such as B_1, B_2, \dots, B_8 [9]. In addition to that sometimes they also exhibit calamitic liquid crystalline phases such as nematic, smectic A etc. In the last chapter of this thesis we discuss alignment properties of bent-core nematic liquid crystals. The chemical structure of a typical bent-core molecule is shown in Figure 1.6.

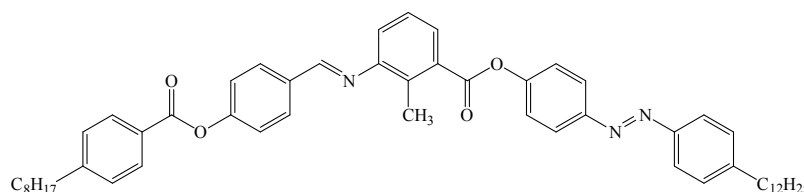


Figure 1.6: The chemical structure of a typical bent-core liquid crystal [10].

1.5 Defects in Nematic Liquid Crystals

When the nematic liquid crystal is confined between two untreated substrates, the director varies slowly in the space and schlieren textures are observed between crossed polarizers. Schlieren textures often exhibit characteristic sets of curved dark brushes. These dark brushes correspond to the extinction

1.5 Defects in Nematic Liquid Crystals

of the nematic director field $\hat{n}(r)$ coinciding with the direction of either the polarizer or the analyzer. The brushes come together in a singular point and it can be commonly two or fourfold. These singularities are called disclinations with defect strength s . The absolute value of the strength of the disclinations are found by dividing the number of brushes by four. The sign of the defect can be found by looking at the sense of rotation of the brushes with respect to the polarizers' rotation. If the dark brushes rotate in the same direction as that of polarizers then it is called a plus (+) defect, otherwise it is a minus (-) defect. In any case these point singularities do not move and the rotation of the brushes is continuous, due to continuous variation of the director field $\hat{n}(r)$. Generally each defect is connected to a defect of same strength but opposite sign and is called antidefect. Normally any given sample have equal no of defects and antidefects. Defects of same strength but opposite sign can attract each other and eventually annihilate to yield a uniform, defect free sample. On the other hand, two defects with same strength and sign may form a different singularity with the strength being the sum of the two original defects.

Considering a planar structure in which the director is confined to the xy plane. The components of the director can be written as $n_x = \cos \phi$, $n_y = \sin \phi$, $n_z = 0$. Assuming that the medium is elastically isotropic, i.e., $K_{11} = K_{22} = K_{33} = K$ and for static deformation, the free energy density is given by [1]

$$F_d = \frac{1}{2}K(\nabla\phi)^2, \quad (1.1)$$

Minimizing the above free energy density, we get

$$\nabla^2\phi = 0, \quad (1.2)$$

The solutions of equation (1.2) are $\phi = 0$, which is of no interest, and

$$\phi = s\alpha + c. \quad (1.3)$$

where $\alpha = \tan^{-1}(y/x)$ and c is a constant. This equation describes the director configuration around a disclination line as shown schematically in

Figure 1.7. The singular line is along the z axis and the director orientation changes by $2\pi s$ on going round the line. If the orientational order is apolar, a rotation of $m\pi$ (where m is an integer) in the director orientation ϕ should correspond to a rotation of 2π in the polar angle α . On the other hand, for a polar medium a change of $2m\pi$ in ϕ should correspond to a change of 2π in α . More generally for apolar medium $s = \pm 1/2, \pm 1, \pm 3/2 \dots$, with $0 < c < \pi$ where as for polar medium $s = \pm 1, \pm 2, \pm 3 \dots$, with $0 < c < 2\pi$.

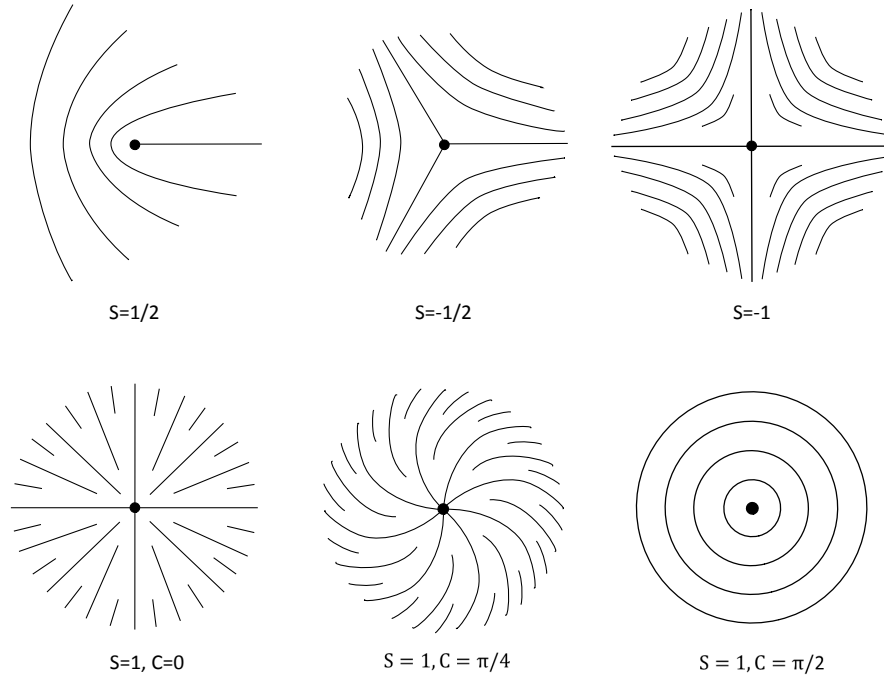


Figure 1.7: Director configurations of some defects.

1.6 Umbilic defects

Consider a nematic liquid crystal with negative dielectric anisotropy ($\epsilon_a < 0$) aligned homeotropically between two glass plates. If an electric field is applied along the z axis i.e parallel to director, a distortion takes place when the field

1.6 Umbilic defects

exceeds the Freedericksz threshold value and is given by

$$E_c = \frac{\pi}{d} \left[\frac{K_{33}}{\epsilon_a} \right]^{1/2}, \quad (1.4)$$

where d is the thickness of the sample and K_{33} is the bend elastic constant. Two possible types of distortions are depicted in Figure 1.8. In the distorted state the perpendicular component \hat{n}_\perp is degenerate in the xy plane. Therefore, there can be defects in the \hat{n}_\perp field, and because of the symmetry in the xy plane, only defects of integral strength can occur. Such defects have been observed and are called umbilics. They are somewhat similar to the $s = \pm 1$ of the schlieren texture but differ in details. Over a distance r [2]

$$r \sim \frac{d}{\pi} \left[\frac{E_c^2}{(E^2 - E_c^2)} \right]^{1/2} \quad (1.5)$$

from the center of the defect, the director gradually tilts towards the z axis, the tilt angle becoming exactly zero at $r = 0$. It means that, umbilics have a collapsed core, but the structure is not exactly the same as that of the $s = \pm 1$ defects [1, 2].

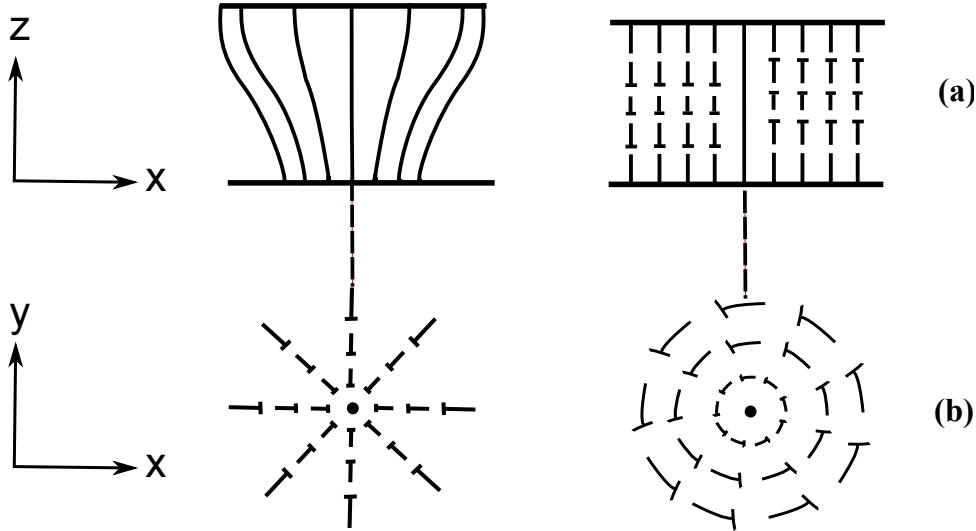


Figure 1.8: Director configurations of various umbilic defects (a) side view (b) top view.

1.7 Properties of Nematic Liquid Crystals

1.7.1 Orientational Order Parameter

The order parameter is a measure of order in the relevant phases. In nematic liquid crystal the orientational order parameter describes the average orientation of the long axes of the molecules along the director. To define the local orientation at a point $\vec{r}=(x, y, z)$, following de Jeu [4], let us assume that the molecule is a rigid rod with a unit vector \hat{a} along the long axis. Now consider the thermal average of the relevant tensor that are composed of \hat{a} , over a microscopic volume around \vec{r} . The first choice is a vector order parameter $\langle \hat{a} \rangle$, where the angular brackets denote the ensemble average. The unit vector \hat{a} will be zero in the nematic phase because of \hat{n} and $-\hat{n}$ are physically equivalent. The next choice of order parameter is a second rank tensor S , the elements of which are given by

$$S_{\alpha\beta} = \langle a_{\alpha}a_{\beta} \rangle - \frac{1}{3}\delta_{\alpha\beta}, \quad \alpha, \beta = x, y, z. \quad (1.6)$$

Notice that the addition of Kronecker delta ensures that $S_{\alpha\beta}$ is zero in the isotropic phase where $\langle a_{\alpha}^2 \rangle = \frac{1}{3}$. The tensor order parameter is symmetric and traceless and has five independent elements. In the principal coordinate system the above tensor can be written in diagonal form. For the uniaxial case, the most general form of order parameter field in the nematic phase is given by

$$S_{\alpha\beta}(\vec{r}) = S \left(n_{\alpha}(\vec{r})n_{\beta}(\vec{r}) - \frac{1}{3}\delta_{\alpha\beta} \right), \quad (1.7)$$

where S is a measure of the degree of alignment of the long axis of the molecules along $\hat{n}(\vec{r})$ and the expression in the parenthesis describes the spatial variation of $\hat{n}(\vec{r})$ from point to point. \hat{n} is independent of \vec{r} in a well-aligned nematic. For cylindrically symmetric molecules the scalar order

1.7 Properties of Nematic Liquid Crystals

parameter is defined as [1]

$$S = \frac{3\langle \cos^2 \theta - 1 \rangle}{2}, \quad (1.8)$$

where the angular brackets represents the ensemble average and θ is the angle made by the molecule with the director. In a perfectly aligned sample $S=1$, whereas in the isotropic phase $S=0$. Usually the value of S in a nematic liquid crystal varies from $\simeq 0.3$ to 0.8 with temperature. The order parameter can be directly related to certain experimentally determined quantities, for example diamagnetic and dielectric anisotropy, birefringence etc [3].

1.7.2 Birefringence

The electric vector of incident plane polarized light entering a birefringent medium is splitted into two mutually perpendicular components called the ordinary (o) and extraordinary (e) rays. The electric field of the o-ray is always perpendicular to the optic axis, so its refractive index n_o is constant and it is independent of propagation direction. In the case of a nematic or a uniaxial smectic liquid crystal the optical axis is parallel to the director and is given by $n_e = n_{\parallel}$ and $n_o = n_{\perp}$ where the parallel and perpendicular directions are defined in relation to the director as shown schematically in Figure 1.9. The birefringence is given by $\Delta n = n_e - n_o = n_{\parallel} - n_{\perp}$. In most

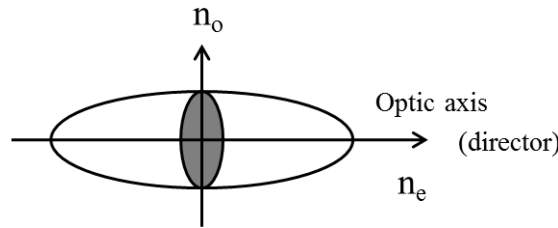


Figure 1.9: Schematic representation of optical indicatrix of a uniaxial system.

calamatic liquid crystals Δn is usually positive and typically varies from 0.01 to 0.2 [4, 11]. Δn data can directly be used to calculate the approximate

order parameter S of nematic liquid crystals using the relation [1]

$$S \approx \frac{\Delta n}{\Delta n_0}, \quad (1.9)$$

where Δn_0 is the birefringence in the perfectly aligned state. This approximation is highly justifiable if Δn is very small.

1.7.3 Dielectric Constant

The dielectric constant ϵ is a measure of the response of the material to an external electric field. It depends on the intrinsic properties of the material like distribution of charges in the molecules as well as intermolecular interactions. The dielectric constant depends on temperature as well as frequency of the applied electric field. For mesogens with polar molecules in addition to the induced polarization an orientational polarization occurs due to the tendency of the permanent dipole moments to orient parallel to the electric field. The orientational polarization in liquid crystals can contribute significantly to the dielectric constant [4, 11]. On the other hand, in a solid crystal the orientational polarization does not contribute significantly to the permittivity due to the fixed orientations of the molecules. In liquid crystals, the dielectric constants ϵ_{\parallel} and ϵ_{\perp} are measured with electric field parallel and perpendicular to the director (\hat{n}) respectively as shown schematically in Figure 1.10. The parallel and perpendicular components of the dielectric constant according to Maier and Meire's theory are written as [12]

$$\epsilon_{\parallel} = 1 + 4\pi \frac{N_A \rho h F}{M} \left[\bar{\alpha} + \frac{2}{3} \Delta\alpha S + \frac{F p^2}{3 k_B T} (1 - (1 - 3 \cos^2 \beta) S) \right], \quad (1.10)$$

$$\epsilon_{\perp} = 1 + 4\pi \frac{N_A \rho h F}{M} \left[\bar{\alpha} - \frac{1}{3} \Delta\alpha S + \frac{F p^2}{3 k_B T} \left(1 + \frac{1}{2} (1 - 3 \cos^2 \beta) S \right) \right], \quad (1.11)$$

where $\Delta\alpha (= \alpha_l - \alpha_t)$ is the anisotropy of polarizability of a perfectly oriented medium, N_A is the Avagadro number, ρ density, M the molecular weight,

1.7 Properties of Nematic Liquid Crystals

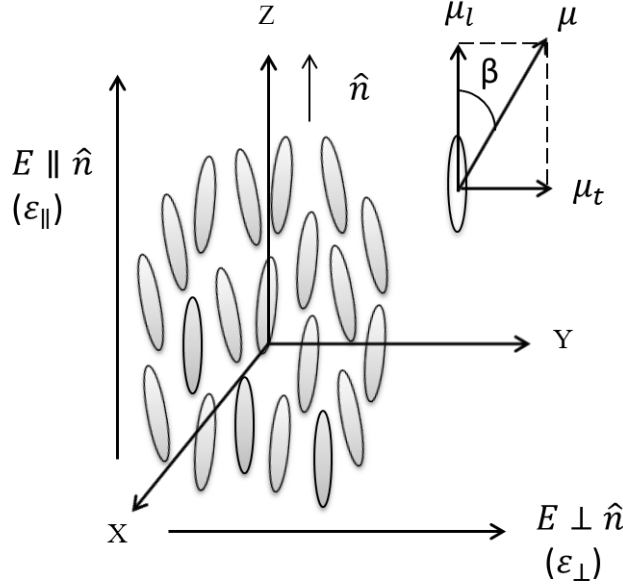


Figure 1.10: A schematic representation of parallel (ϵ_{\parallel}) and perpendicular (ϵ_{\perp}) components of dielectric constant of a nematic. The molecule is assumed to possess a dipole moment μ at an angle β with its long axis giving the longitudinal μ_l and transverse μ_t components. The measuring electric field E can be either parallel ($E \parallel \hat{n}$) or perpendicular ($E \perp \hat{n}$) to the director.

$h = \frac{3\bar{\epsilon}}{2\bar{\epsilon}+1}$, is the cavity field factor and $F = \frac{1}{(1-f\bar{\alpha})}$ where $f = \frac{(\bar{\epsilon}-1)}{[2\pi\bar{\alpha}^3(2\bar{\epsilon}+1)]}$ is the reaction field factor for spherical cavity and $\bar{\alpha}$, is the average polarizability, p is the molecular dipole moment. β is the angle between the direction of the dipole moment and the long axis of the molecule. The average dielectric constant $\bar{\epsilon}$ and the dielectric anisotropy ($\Delta\epsilon$) are given by

$$\bar{\epsilon} = 1 + \frac{4\pi N_A \rho h F}{M} \left(\bar{\alpha} + \frac{F p^2}{3k_B T} \right), \quad (1.12)$$

$$\Delta\epsilon = \epsilon_{\parallel} - \epsilon_{\perp} = \frac{4\pi N_A \rho h F}{M} \left[\Delta\alpha - F \left(\frac{p^2}{2k_B T} \right) (1 - 3\cos^2 \beta) \right] S. \quad (1.13)$$

The relative magnitude of the two terms within the square brackets of equation 1.13 determines the sign of $\Delta\epsilon$. When $\beta < 55^\circ$, the two terms add up and the

compound exhibits a positive dielectric anisotropy. For $\beta \simeq 55^\circ$, the second term vanishes and only $\Delta\alpha$ contributes to $\Delta\epsilon$. For $\beta > 55^\circ$, $\Delta\epsilon > 0$ or < 0 , depending on whether the dipolar contribution is less or more than the contribution due to polarizability anisotropy.

1.7.4 Curvature Elasticity

In nematic liquid crystal the director orientation varies in space. All these deformations that causes elastic distortions can be considered to be the combinations of three basic curvature elastic deformations. They are called splay, twist and bend. A schematic representation of these deformations are shown in Figure 1.11. The deformation free energy density (F_d) is given by [1, 2]

$$F_d = \frac{1}{2}K_{11}(\nabla \cdot \hat{n})^2 + \frac{1}{2}K_{22}(\hat{n} \cdot \nabla \times \hat{n})^2 + \frac{1}{2}K_{33}(\hat{n} \times \nabla \times \hat{n})^2, \quad (1.14)$$

where K_{11} , K_{22} and K_{33} are the splay, twist and bend elastic constants respectively. The elastic constants are positive and usually $K_{33} > K_{11} > K_{22}$. The elastic constants are of the order of $k_B T/a$, where k_B is the Boltzmann constant and a is the typical molecular dimension. The typical magnitude of these constants are $\sim 10^{-12}$ N.

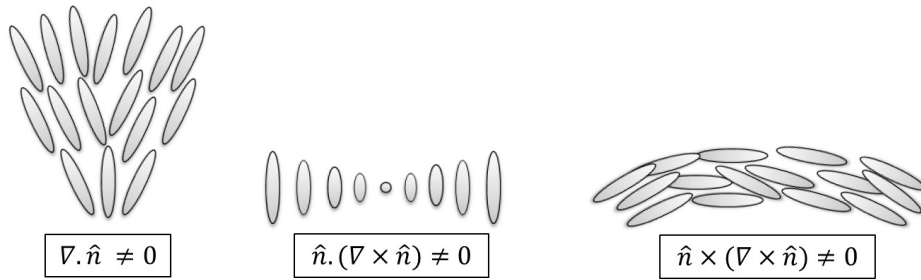


Figure 1.11: A Schematic representation of the splay, twist and bend deformations.

1.7 Properties of Nematic Liquid Crystals

1.7.5 Pretilt Angle

In the absence of external fields in planar cell the director is oriented uniformly along the easy axis that makes an angle α with respect to the x axis. The angle α defines the minimum of the surface anchoring potential and is called the pretilt angle (α). A schematic representation of pretilt angle is shown in the Figure 1.12. Pretilt angle is one of the important parameter for liquid crystal display (LCDs) because it strongly influences the performance of the devices [13, 14]. In order to optimize display performance, it is important to measure pretilt angle. There are several methods for measuring the pretilt angle *viz.*, (i) crystal rotation method (CRM) (ii) capacitive method and (iii) magnetic null method. Frequently the crystal rotation method is used because it is simple, precise and rapid [15]. However, CRM cannot be used if the pretilt angle is higher than 10° because it is difficult to determine the symmetry point.

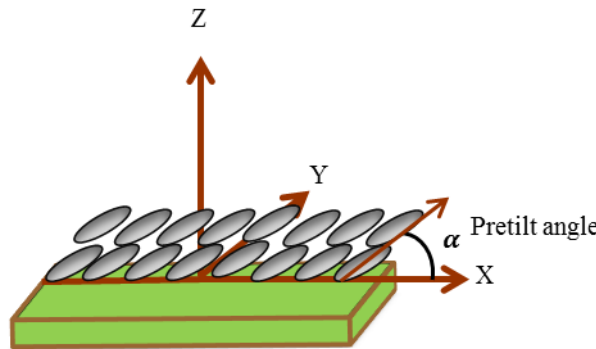


Figure 1.12: Schematic representation of pretilt angle (α) of liquid crystals on a substrate surface.

1.7.6 Anchoring Energy

The surface normally imposes some preferred orientational directions, called anchoring directions, or, simply, easy direction as discussed above. The easy axis is then the direction of spontaneous orientation of \hat{n} on the surface. The

director orientation at the interface is defined in terms of a polar surface angle, ψ_s , and of an azimuthal angle, ϕ_s as shown in Figure 1.13. The anchoring energy can be physically interpreted as the work which must be done to rotate the director from the easy direction to the actual one. There are two anchoring energies namely polar and azimuthal anchoring energies. These anchoring energies can be measured by several different experimental techniques [16–19]. According to Rapini-Papoular [20] the surface free energy per unit area is given by

$$F_s = \frac{1}{2} A \sin^2 \psi_s, \quad (1.15)$$

where ψ_s is the tilt angle of the \hat{n} with respect to the surface and A is the anchoring energy per unit area. Typical experimental values of A is of the order of 10^{-7} to 10^{-4} J/m^2 .

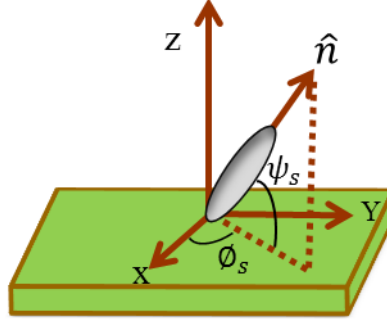


Figure 1.13: Schematic representation of surface anchoring of liquid crystal on a substrate surface.

1.7.7 Rotational Viscosity

Rotational viscosity (γ_1) is one of the most important parameter of liquid crystal devices because it determines the electro-optical switching speed. The magnitude of γ_1 depends on temperature, inter molecular interactions, and

1.8 Alignment of Liquid Crystals

the molecular structure. For a LC slab of thickness d , γ_1 is given by [21, 22]

$$\gamma_1 = \frac{\tau_0 K_{11} \pi^2}{d^2} \quad (1.16)$$

where K_{11} is the splay elastic coefficient and τ_0 is the relaxation time. Thus the relaxation time (τ_0) of the LC device is linearly proportional to γ_1 .

1.8 Alignment of Liquid Crystals

Alignment of liquid crystals on substrate is very important from technological point of view [23, 24]. The uniform orientation of director also enables us to measure the several physical properties such as birefringence, dielectric and elastic constants. Commonly there are two types of director orientations are preferred namely planar or homogeneous and vertical or homeotropic. The homogeneous and homeotropic alignment of liquid crystal director can be achieved by coating substrates with appropriate polyimide as shown schematically in the Figure 1.14. In case of homogeneous alignment the surface is rubbed in specific direction and the director is parallel to the rubbing direction. On the other hand for homeotropic alignment, the alignment layer orients the director perpendicular to the substrate. Schematic representation of homogeneous and homeotropic alignment of the director is shown in Figure 1.14(a)&(b).

1.8.1 Freedericksz' transition in nematic liquid crystal with strong surface anchoring

The dielectric displacement \vec{D} in a nematic liquid crystal is given by [25, 26]

$$\vec{D} = \epsilon_0 \epsilon_{\perp} \vec{E} + \epsilon_0 \Delta \epsilon (\hat{n} \cdot \vec{E}) \hat{n}, \quad (1.17)$$

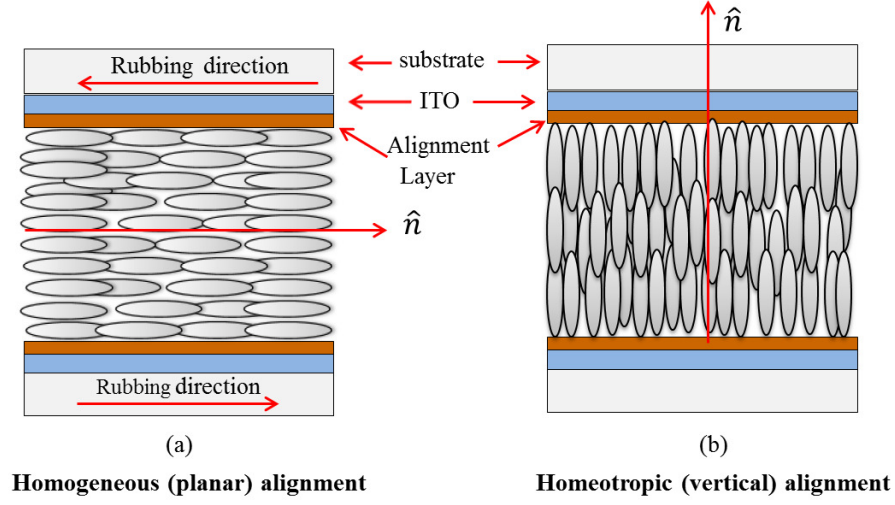


Figure 1.14: Schematic representation of homogeneous and homeotropic alignment of the director on ITO substrates.

and the dielectric energy density of a nematic is given by

$$W_{diel} = - \int_0^E \vec{D} \cdot d\vec{E} = -\frac{1}{2} \epsilon_0 \epsilon_{\perp} \vec{E}^2 - \frac{1}{2} \epsilon_0 \Delta\epsilon (\hat{n} \cdot \vec{E})^2. \quad (1.18)$$

It is noted that the dielectric energy is lowered by an alignment of \hat{n} with respect to E , which depends on the sign of the $\Delta\epsilon$.

In a uniformly aligned sample when an electric field is applied to the director a distortion takes place only when the strength of applied field exceeds a certain well defined threshold value. This is called Freedericksz transition [11]. The threshold voltage is given by

$$V_{th} = \pi \sqrt{\frac{K_{11}}{\epsilon_0 \Delta\epsilon}}, \quad (1.19)$$

where K_{11} is the splay elastic constant. Consider a sample with positive dielectric anisotropy taken between two ITO coated glass plates aligned homogeneously as shown schematically in Figure 1.15(a). When an electric field is applied to the sample, the molecules tend to align parallel to the electric field as shown schematically in Figure 1.15(b).

REFERENCES

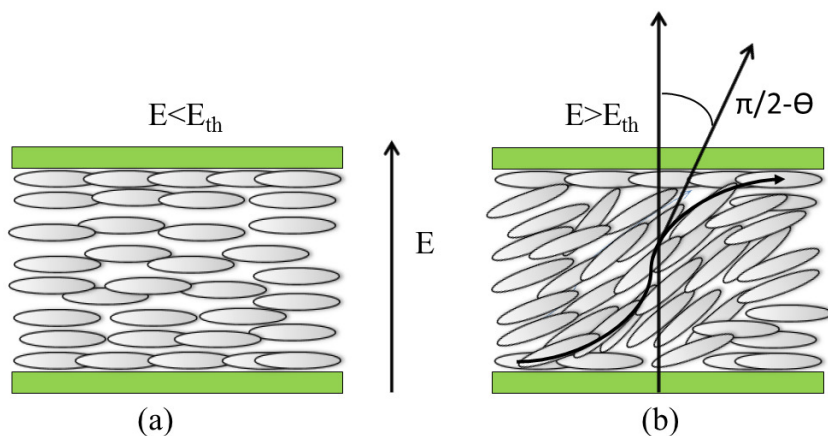


Figure 1.15: Schematic representation of director configuration is shown (a) below and (b) above the threshold field respectively.

References

- [1] P. G. de Gennes and J. Prost, *The physics of liquid crystals*, 2nd Ed. Clarendon, Oxford, 1993.
- [2] S. Chandrasekhar, *Liquid crystals*, Cambridge University Press, Cambridge, 1992.
- [3] P. J. Collings and M. Hird, *Introduction to liquid crystals chemistry and physics*, Taylor & Francis, 1997.
- [4] W. H. de Jeu, *Physical properties of liquid crystals*, 2nd Ed. Cambridge University Press, Cambridge, 1992.
- [5] G. Friedel, *Ann. Phys. Paris.*, **18**, 273 (1922).
- [6] M. J. Stephen and J. P. Straley, “ Physics of liquid crystals”, *Rev. Mod. Phys.*, **46**, 617 (1974).
- [7] D. Vorlander and A. Apel, *Ber. Dtsch. Chem. Ges*, **65**, 1101 (1932).

REFERENCES

- [8] T. Niori, T. Sekine, J. Watanabe, T. Furukuwa and H. Takezoe, “Distinct ferroelectric smectic liquid crystals consisting of banana shaped achiral molecules”, *J. Mater. Chem.*, **6**, 1231 (1996).
- [9] H. Takezoe and Y. Takanishi, “Bent-core liquid crystals: Their mysterious and attractive world”, *Jpn. J. Appl. Phys.*, **45**, 597 (2006).
- [10] B. Senyuk, H. Wonderly, M. Mathews, Q. Li, S. V. Shiyankovskii, and O. D. Lavrentovich, “Surface alignment, anchoring transitions, optical properties, and topological defects in the nematic phase of thermotropic bent-core liquid crystal A131”, *Phys. Rev. E* **82**, 041711 (2010).
- [11] L. M. Blinov, V. G. Chigrinov, *Electrooptic effects in liquid crystals*, Springer-Verlag, New York, 1996.
- [12] W. Maier and G. Meier, *Z. Naturforsch.*, **16a**, 262 (1961).
- [13] P. Yeh and C. Gu, *Optics of liquid crystal displays*, John Wiley and Sons, Inc., 1999.
- [14] I. C. Khoo and S. T. Wu, *Optics and nonlinear optics of liquid crystals*, vol.1, World Scientific, 2007.
- [15] T. J. Scheffer and J. Nehring, “Accurate determination of liquid-crystal tilt bias angles”, *J. Appl. Phys.*, **48**, 1783 (1977).
- [16] H. Yokoyama and H. A. van Sprang, “A novel method for determining the anchoring energy function at a nematic liquid crystal wall interface from director distortions at high fields”, *J. Appl. Phys.*, **57**, 10 (1985).
- [17] Y. A. Nastishin, R. D. Polak, S. V. Shiyankovskii, V. H. Bodnar and O. D. Lavrentovich, “Nematic polar anchoring strength measured by electric field techniques”, *J. Appl. Phys.*, **86**, 8 (1995).
- [18] X. Nie, Y. H. Lin, T. X. Wu, H. Wang, Z. Ge and S. T. Wu, “Polar anchoring energy measurement of vertically aligned liquid crystal cells”, *J. Appl. Phys.*, **98**, 013516 (2005).

REFERENCES

- [19] M. Vilfan and M. Copic, “Azimuthal and zenithal anchoring of nematic liquid crystals”, *Phys. Rev. E* **68**, 031704 (2003).
- [20] A. Rapini, M. Papoular, “Distortion d’une lamelle nématique sous champ magnétique conditions d’ancrage aux parois”, *J. Phys. Colloq. France* **30**, C4-54 (1969).
- [21] S. T. Wu and C. S. Wu, “Experimental confirmation of the Osipov-Terentjev theory on the viscosity of nematic liquid crystals”, *Phys. Rev. A* **42**, 2219 (1990).
- [22] M. L. Dark, M. H. Moore, D. K. Shenoy and R. Shashidhar, “Rotational viscosity and molecular structure of nematic liquid crystals”, *Liq. Cryst.*, **33**, 1 (2006).
- [23] A. A. Sonin, *The surface physics of liquid crystals*, Gordon and Breach Publishers, 1995.
- [24] K. Takato, M. Sakamoto, R. Hasegawa, M. Kodan, N. Itoh and M. Hasegawa, *Alignment technology and applications of liquid crystal devices*, CRC Press, 2005.
- [25] H. J. Deuling, “Deformation of nematic liquid crystals in an electric field”, *Mol. Cryst. Liq. Cryst.*, **19**, 123 (1972).
- [26] H. Gruler and G. Meier, “Electric field induced deformations in oriented liquid crystals of the nematic type”, *Mol. Cryst. Liq. Cryst.*, **16** 299 (1972).

2

Instrumentation

2.1 Introduction

Liquid crystals are confined in cells, which are generally made up of two Indium-Tin-Oxide (ITO) coated glass plates. Appropriate alignment layers are spin coated on the ITO plates for preferred orientation of liquid crystal director. Construction of LC cell involves several steps inside the clean room. The procedure for fabrication of LC cell, design and construction of rubbing machine as well as a heater are discussed in this chapter.

2.2 Preparation of Liquid Crystal Cell

Procedure for making LC cell is as follows: we use ITO coated glass plates for fabricating LC cell which are obtained from Macwin India Pvt. Ltd. The thickness of ITO film is $\simeq 1500\text{\AA}$ and resistivity is $\simeq 15\text{-}20\text{ ohm}/\text{cm}^2$. In order to get circularly patterned ITO plates, we have designed a pattern made up of soft sticky tape as shown in Figure 2.1(a). After cutting ITO glass plates into desired size we stick the pattern on the ITO glass plates. Then we etch the ITO plates in the presence of dilute HCl and Zinc powder. Etching removes the unwanted ITO and leaves only the desired circular geometry of ITO as shown in Figure 2.1(b). Such type of patterned ITO plates are

rinsed with soap water and cleaned thoroughly with water. Then the ITO plates are sonicated for 10 min each in the presence of Acetone and distilled water respectively. After sonication, Nitrogen gas is used to blow off the water droplets if any on the glass plates before spin coating. Depending upon our requirement different alignment layers are used i.e homogeneous or homeotropic for spin coating. The thickness of the film can be controlled by setting the speed of the spin coater (Delta spin-1, Delta Scientific Equipment Pvt. Ltd., India). After coating, glass plates were kept in the oven for baking at specific temperature for a fixed duration. Depending upon the choice of alignment layer the plates are rubbed antiparallel way. We use glass beads (Micropearl SI type, SEKISUI Chemicals CO. Ltd., Japan) or mylar sheets to achieve desired uniform thickness of the LC cell. A paste is made with spacer and optical adhesive (Norland Optical Adhesive 81, Norland Products Inc., Cranbury, NJ 08512) for sealing the glass plates near the edges. Finally, the cell is exposed to UV light (365 nm) (HLU-30, Hychem Laboratories) for 2 min for sealing. The electrical connections to the cell were made by using ultrasonic soldering machine (SUNBONDER, USM IV, Kuroda Techno Co., Ltd.) with cerasolzer. The photographs of spin coater, optical adhesive and ultrasonic soldering are presented in Figure 2.2. The schematic diagram and a photograph of a LC cell is shown in Figure 2.3.

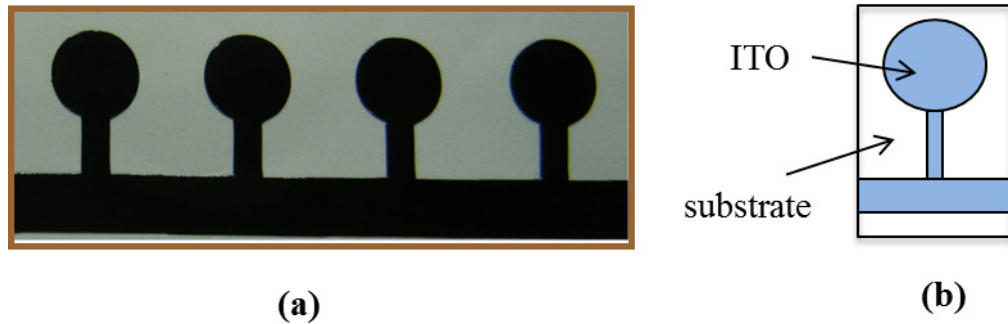


Figure 2.1: Photograph of patterned sticker and schematic diagram of glass plate with patterned ITO.

2.2 Preparation of Liquid Crystal Cell

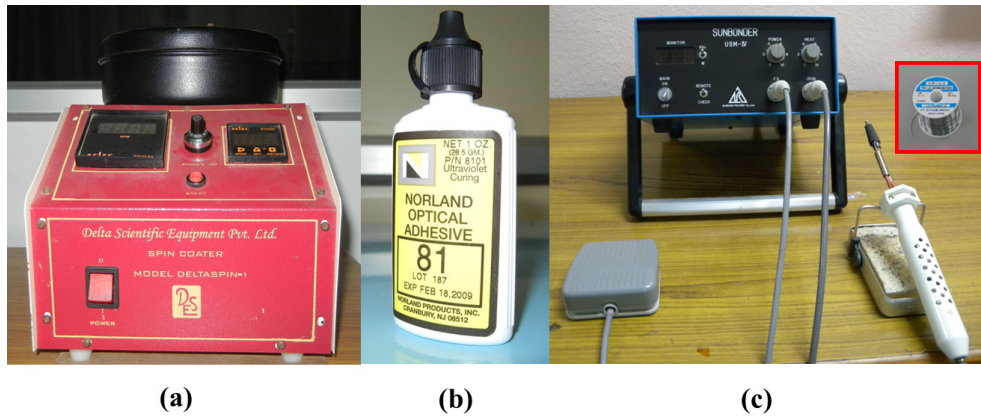


Figure 2.2: photographs of (a) spin coater, (b) optical adhesive and (c) ultrasonic soldering unit.

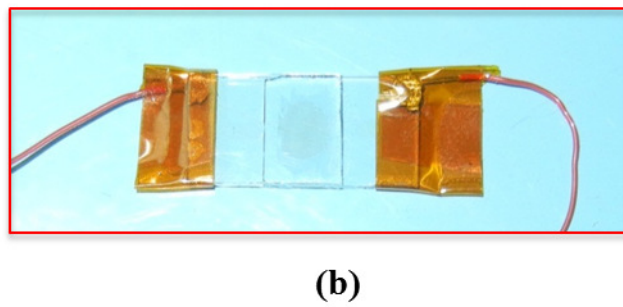
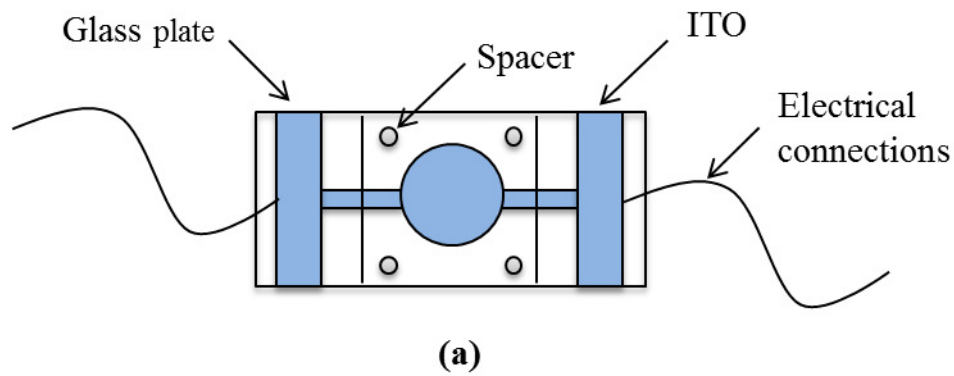


Figure 2.3: Schematic diagram and a photograph of LC cell made up of ITO glass plates.

2.3 Design and Construction of Rubbing machine

A bench top rubbing machine was designed and constructed by us with the help of Holmarc, Opto-Mechatronics Pvt. Ltd, India. The drawing of the machine is shown in Figure 2.4. The construction of the rubbing machine is as follows: As shown in Figure 2.5, the spindle is made of steel rod and is placed on two supporting metal blocks. The spindle is rotated by a DC motor and its speed ranges from 300 rpm to 3000 rpm. This spindle is wrapped with a soft velvet cloth so that gentle rubbing can be made on glass plates. In

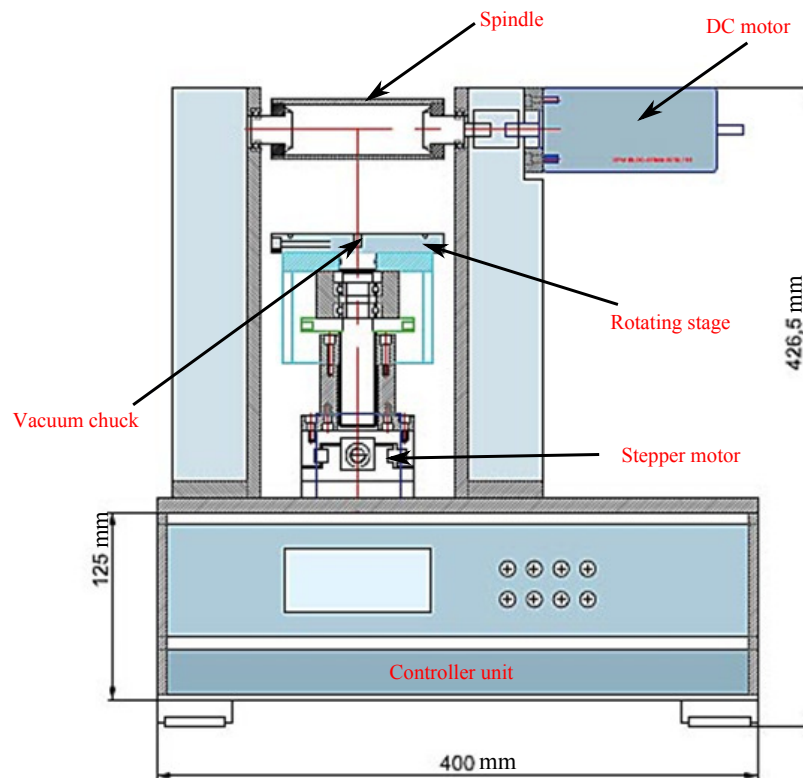


Figure 2.4: Drawing of the rubbing machine.

order to hold the glass plate while being rubbed, a vacuum chuck is provided on rotating stage. This vacuum holds the glass plate which is connected to a vacuum pump (Minivac, model No. SV 75S) and can provide $\simeq 1$ bar of vacuum. The rotating stage is a circular disc and can be rotated 180° .

2.4 Design and Construction of Heater for sample preparation

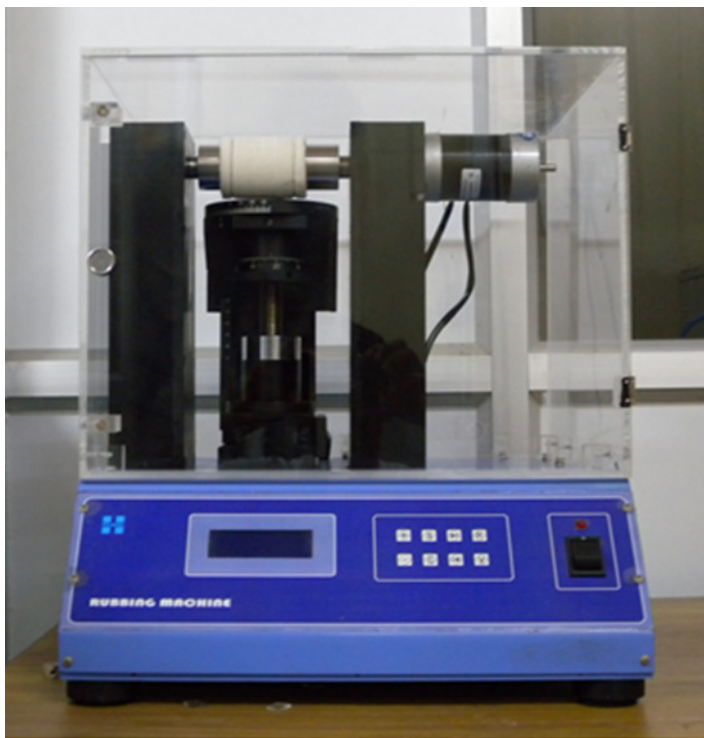


Figure 2.5: Photograph of rubbing machine.

Rubbing pressure can be controlled by adjusting the height of the rotating stage using a knob which is placed just below the stage. The rotating stage can also be moved horizontally to and fro with the help of a stepper motor. The distance the rotating stage can move is at least 70 to 80mm and the speed ranges from 0.1 mm/sec to 10 mm/sec. This rubbing machine is provided with programmable control unit with LCD display. Every function of the machine can be controlled from the front panel.

2.4 Design and Construction of Heater for sample preparation

A heater was designed for physical mixing of more than two liquid crystals. This heater consists of a Variac, temperature controller, thermocouple and

aluminium sample holder. The photograph of a heater is shown in Figure 2.6. Variac can supply the voltage of 230-260V with 2A current. The voltage from Variac is supplied to the heater (40V) through a ON and OFF controller (model ST-48 of range 200-1600°C). Thermocouple is used in this heater

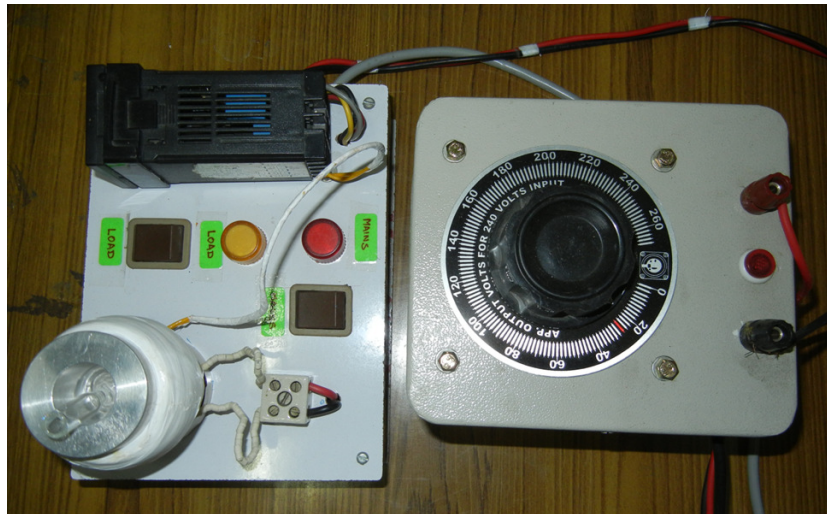


Figure 2.6: Photograph of a heater.

as a sensor. An aluminium sample holder with cylindrical hole was made so that sample with 10 ml bottle can go inside easily. This aluminium sample holder is wrapped with Kanthal Super, which is loaded with ceramic beads. This Kanthal Super is then surrounded by ceramic wool and followed by teflon to maintain uniform heat within the sample holder. The target temperature is fixed on the controller and the sample can be heated to the desired temperature for mixing. A glass rod is stirred continuously for uniform mixing in the isotropic phase.

2.5 Measurement of Cell Thickness

The thickness of the cell is measured using interferometric technique. The schematic diagram of the setup is shown in the Figure 2.7. The fiber optic spectrometer (Ocean Optics) consists of source, controller and fiber. The

2.5 Measurement of Cell Thickness

reflection probe consists of 7 optical fibers, out of which the central fibers is the read fiber and surrounding 6 fibers are the illuminating fibers. The light incident on the cell through the 6 illuminating fibers will get reflected back from the cell to the read fiber of the reflection probe and the signal is sensed through the spectrometer (HR4000CG-UV-NIR) which in turn will display the interference pattern on the screen of the computer monitor. The light reflected by the two internal surfaces of the cell interfere to produce the interference pattern. We use this interferometer to make precise measurements of cell thickness at various positions.

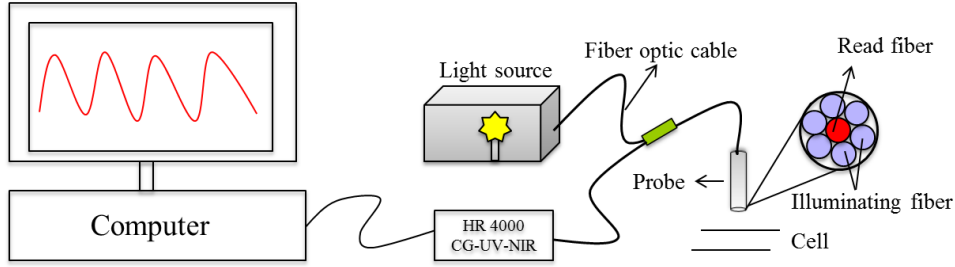


Figure 2.7: Schematic diagram of the Ocean optic spectrometer.

The interference pattern consists of maxima and minima corresponding to constructive and destructive interference. The thickness of the cell d is calculated by measuring the air gap between the two glass plates of the cell using the formula:

$$d = \frac{(m - n) (\lambda_m \times \lambda_n)}{2 (\lambda_m - \lambda_n)},$$

where λ_m and λ_n are wavelegths corresponding to m^{th} and n^{th} minima or maxima. The accuracy in the cell thickness measurement is $\simeq 1\%$.

3

Temperature and electric field induced inverse Freedericksz transition in a nematogen with weak surface anchoring

3.1 Introduction

Aligning liquid-crystal molecules in a particular direction at solid substrate surfaces is very important from technological as well as fundamental points of view [1]. As we have discussed earlier two different categories of alignment layers are used in liquid crystal display devices (LCDs), i.e., homogeneous or planar and homeotropic. Depending on the strength of the anchoring energy, liquid crystals can also exhibit a rich variety of phenomena such as memory effect [2], surface melting [3], orientational wetting [4, 5] etc. Apart from this in appropriate surface condition the liquid-crystal molecules may exhibit anchoring transition, i.e., spontaneous change in the director orientation. There are some theoretical and experimental reports on various anchoring transitions [6–25]. Among these a few reports are about the continuous anchoring transition as a function of temperature on various alignment layers

Temperature and electric field induced inverse Fredericksz transition in a nematogen with weak surface anchoring

in nematic liquid crystals [6–9]. Anchoring transition was first observed in 1976 by Ryschenkow *et al.* [6] at the interface between glass and MBBA by varying the temperature. When the temperature is increased towards the nematic-isotropic transition, a continuous anchoring transition between a conical and homeotropic anchoring was observed. In 1993 Patel *et al.* [7] observed a temperature dependent continuous anchoring transition of liquid crystal mixture E7 in fluoropolymer treated cells. They have measured the surface tilt angle using oriented sample in the temperature region where the liquid crystal undergoes an anchoring transition. The variation of tilt angle as a function of temperature is shown in Figure 3.1. The exact interfacial mechanism for continuous anchoring transition is not known, but it was indicated that two competing temperature dependent force are responsible, one that prefers homogeneous orientation and other that prefers homeotropic orientation. A surface anchoring transition of a nematic at polymer surfaces

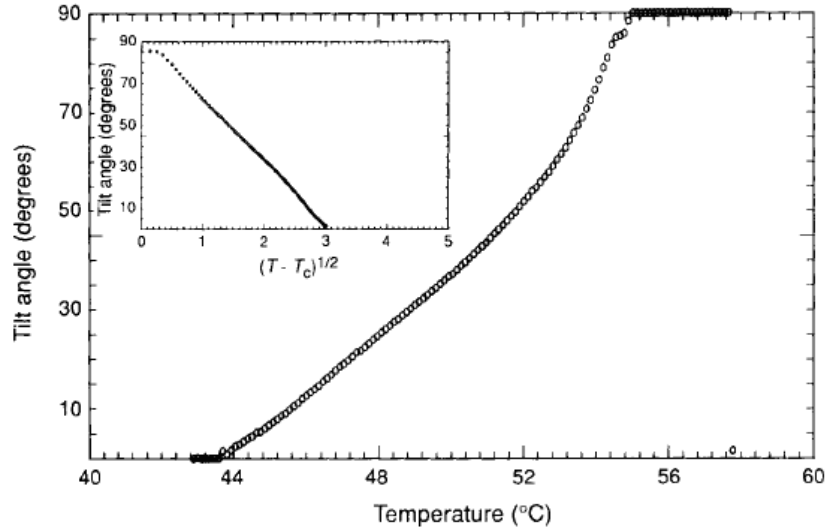


Figure 3.1: Variation of tilt angle as a function of temperature as determined from the intensity data. The insert is a semi-log plot of tilt angle against the square root of the reduced temperature. Here T_c correspond to the onset of the homeotropic transition temperature. (adopted from ref. [7]).

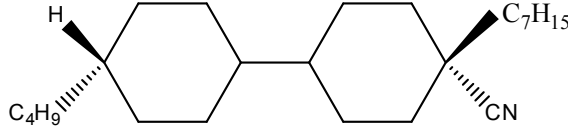
created by polymerization induced phase separation was seen by Amundson *et*

3.1 Introduction

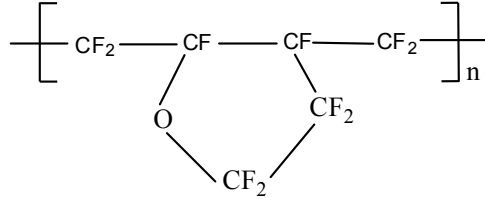
al. [10]. This transition occurs far from bulk nematic phase transition and it is tunable across nearly the entire nematic temperature range by modification of the polymer side group. A computer simulation of temperature driven anchoring transition in nematic liquid crystal was also reported by Lin and Taylor [11]. Their observations reveals that the anchoring transition can be induced by the thermal motion of the substrate.

A brief and qualitative study on discontinuous anchoring transition in the mixture of liquid crystals with a longitudinal dipole moments (4-cyano-4'-n-octylbiphenyl (8CB) and 4-cyano-4'-n-octyloxycyanobiphenyl (8OCB)) as a function of temperature was made by Birecki [12]. However, no quantitative measurements were made to reveal the role of molecular dipole moment and various surface forces. Faget *et al.* [13] demonstrated conical to planar and to anticonical transitions on grafted polystere surface and also theoretically explained including the non-Rapini-Papoular terms in the anchoring energy. Recently Dhara *et al.* [14] have shown some interesting experimental observations of a liquid crystal 4'-butyl-4-heptyl-bicyclohexyl-4-carbonitrile (CCN-47) which exhibits large transverse dipole moment on a perfluoropolymer alignment layer. They reported a strong discontinuous anchoring transition of liquid crystal director from planar to homeotropic with decreasing temperature. They have also demonstrated that the thermal hysteresis of the discontinuous anchoring transition can be used to fabricate light-driven bistable memory or rewritable devices [15, 16]. The chemical structures of CCN-47 and perfluoropolymer are shown in Figure 3.2. CCN-47 exhibits the following sequence of phase transitions: Cr 25.6°C SmA 28.2°C N 57.3°C I, and has a large negative dielectric anisotropy ($\Delta\epsilon = -5.7$ at 30°C). CCN-47 showed a planar texture at 50°C as shown in Figure 3.3(a). On further cooling the sample temperature below 45°C the dark region grows abruptly and randomly as shown in Figure 3.3(b) and the whole area becomes dark within a temperature range of $\sim 1^\circ\text{C}$ as shown in Figure 3.3(c). It indicates that the director orientation spontaneously changes from planar to vertical direction (homeotropic alignment). They measured the transmitted intensity as a function of temperature (Figure 3.4(a)) and calculated the birefringence from the transmitted intensity. The variation of birefringence as a function

Temperature and electric field induced inverse Fredericksz transition in a nematogen with weak surface anchoring



(a)



(b)

Figure 3.2: The Chemical structures of: (a) CCN-47 and (b) perfluoropolymer.

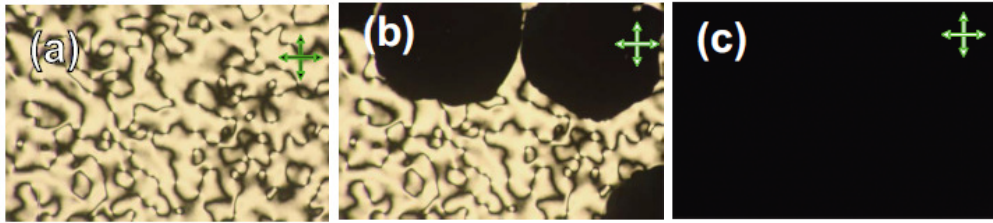


Figure 3.3: Photomicrographs of the textures showing anchoring transitions in CCN-47 under crossed polarizers (white crossed arrows): (a) CCN-47 at 50°C; (b) CCN-47 during the discontinuous anchoring transition; (c) CCN-47 at 40°C (adopted from ref. [14]).

of temperature in both heating and cooling cycles is shown in Figure 3.4(b). They explained the results by considering steric, short-range dipolar and long-range Van der Waals interactions [17, 26, 27].

3.1 Introduction

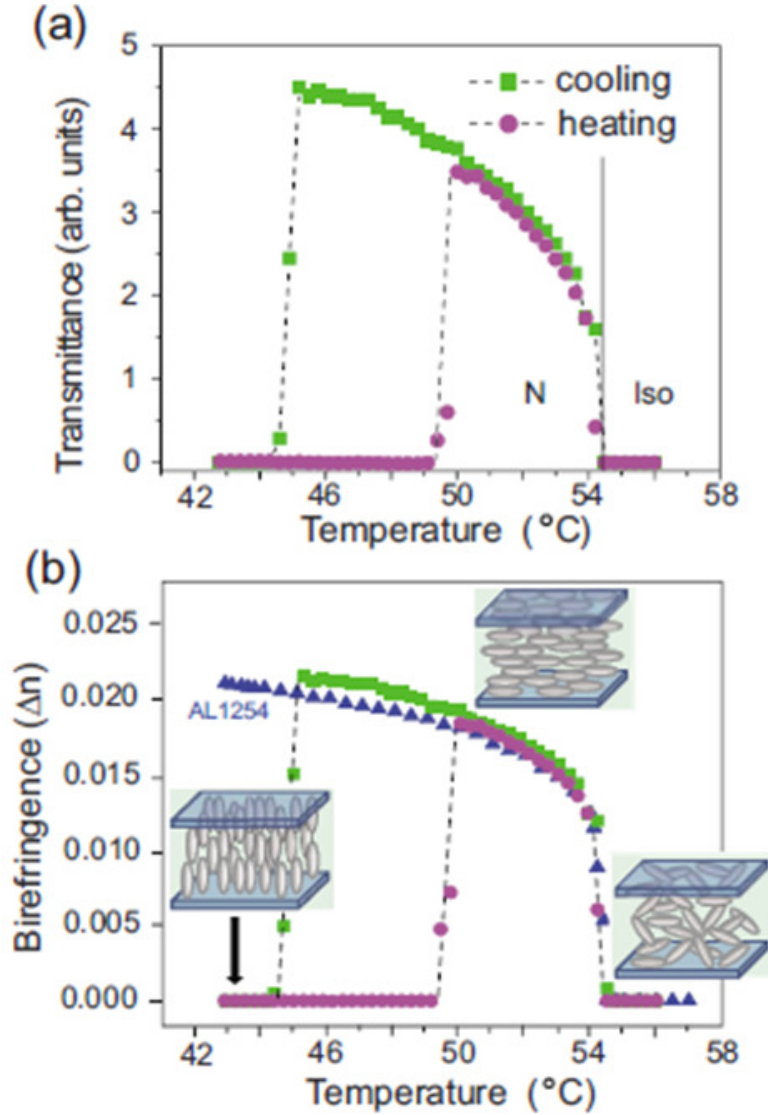


Figure 3.4: (a) Transmitted light intensity of an orientated sample of CCN-47 between crossed polarizers as a function of temperature. (b) Calculated birefringence obtained from (a). Data for cooling and heating processes are shown by squares and circles, respectively. A large hysteresis in temperature is observed. Data corresponding to triangles are measured using homogeneous alignment agent AL-1254, which shows no anchoring transition (adopted from ref. [14]). It may be mentioned that a small shift in the NI transition temperature is due to uncalibrated heater. The correct temperature is reported in ref. [15].

3.2 Experimental

We have used the same perfluoropolymer poly[perfluoro-(4-vinyloxy-1-butene)] (PPFVB, commercially known as CYTOP) as alignment layer for our experiment. CYTOP is used widely for antireflective coatings and optical fibers because of its low refractive index (1.34) and high transmittance over a wide wavelength range (200 nm to 2 μ m). Besides, its high solubility in fluorinated solvent makes it suitable for easy coating on substrate for various applications in photonics such as nanoimprint lithography (NIL), organic light-emitting diodes (OLEDs), lasing, and in biological applications. CYTOP solution was prepared by adding 1 part of CTX-809A to 2 parts of CT-Solv.180 by weight. These were obtained from Asahi Glass Co., Ltd. Japan. CYTOP was spin-coated on ITO-coated glass plates. After coating, substrates were kept in oven at 100°C for 30 minutes. Spacers of 5 μ m were mixed with glue and a line of glue was applied at the edge of the substrates to make a cell. Then UV polymerization of empty cell was done by exposing to UV light. The liquid crystal was filled in the cell in the isotropic phase by capillary action. The textures were observed using a polarizing optical microscope (Olympus BX-51). The temperature of the sample is controlled by a Mettler hotstage (FP82HT) to an accuracy of 0.1°C. A signal generator (Tektronix AFG 3102) was used to apply sinusoidal voltages at a frequency of 3.11 KHz.

3.3 Results and Discussion

We first show the textures observed under a optical polarizing microscope in the absence of an electric field. The compound exhibits a planar texture as it is cooled below the isotropic to nematic transition temperature. At 52.2°C mostly half-strength disclinations are observed. The photomicrograph in Figure 3.5(a) shows the texture with mostly half strength disclinations. From Figure 3.5(a) we can make the physical inferences that the occurrence of the two-brush defects are twofold. First the director is apolar, i.e., \hat{n}

3.3 Results and Discussion

and $-\hat{n}$ are physically equivalent, and second the director is in the plane parallel to the plates, forming line defects [28]. As the temperature is lowered dark domains are nucleated at about 48°C in a few locations of the sample and spread with time as shown in Figure 3.5(b) even if the temperature is held fixed. The photomicrograph in Figure 3.5(b) shows nucleation of dark domains in the sample. A closer look reveals that in the dark domains the director is normal to the substrate, i.e., the alignment is homeotropic. Thus at the anchoring transition the director rotates by 90°, from planar to homeotropic, *discontinuously*. On further cooling the sample to about 46°C, the entire texture turns completely dark as shown in Figure 3.5(c). Our careful observation of the sample shows that the medium is uniaxial. We studied the effect of electric field on this discontinuous anchoring transition. Initially the sample is heated to the isotropic phase and slowly cooled at the rate 0.2°C per minute in the presence of a desired ac field with a frequency 3.11 KHz. Interestingly, after the transition from isotropic to nematic phase, the appearance of the texture is essentially the same as in the zero-field case. The half-strength and one-strength defects appear at the same locations in the sample as in the field free run. For low fields ($\leq 0.1\text{V}/\mu\text{m}$) homeotropic domains also nucleated at the same locations as in the zero-field case, but at field-dependent *lower* temperatures as shown in Figure 3.5(d). The growth of any given domain is also similar to that in the field free sample. The anchoring transition occurs with the formation of dark domains (i.e., discontinuously) up to the field of $\simeq 0.1\text{V}/\mu\text{m}$ and the anchoring transition temperature is 47.2°C. Beyond this field the anchoring transition occurs with the appearance of regions with *reduced birefringence*, instead of dark domains, but located at the same places. Textures exhibited by the sample which undergoes a continuous anchoring transition under the field are also shown in Figure 3.5(d)-(f). As shown in Figure 3.5(d), a domain with lower birefringence appears as the temperature is reduced under an electric field of $0.29\text{V}/\mu\text{m}$. This domain grows in size on further cooling as shown in Figure 3.5(e). Curiously, most of the defects are expelled from the growing domains such that their nuclei collect at the interface between the domains and the surrounding sample which continues to have a planar alignment. On very rare occasions, a half strength

Temperature and electric field induced inverse Fredericksz
transition in a nematogen with weak surface anchoring

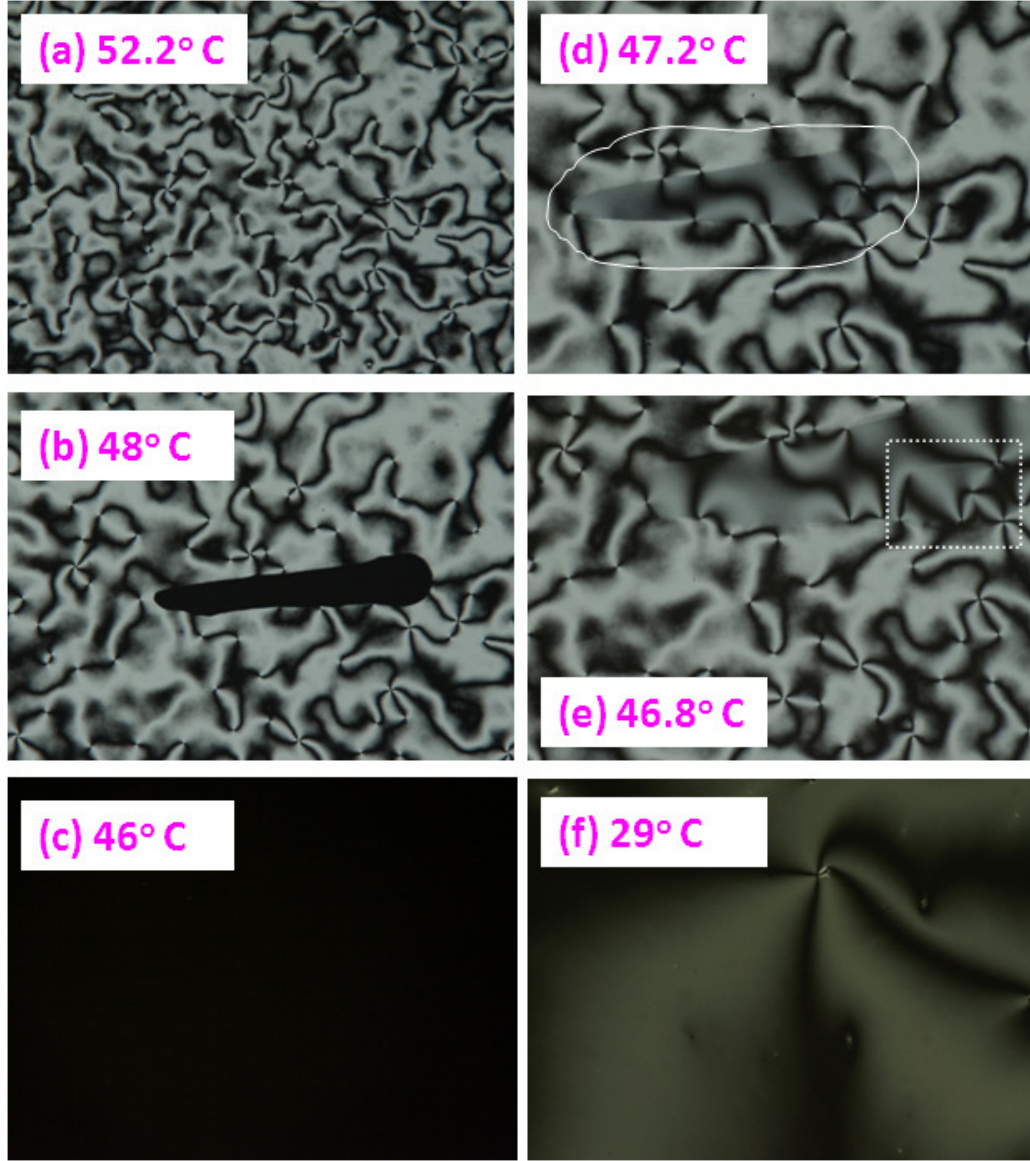


Figure 3.5: Photomicrographs of the textures around the anchoring transition temperature in CCN-47 between crossed polarizers, at (a) 52.2°C (b) 48°C (c) 46°C., all under zero field. Textures in the same region under an electric field of $0.29\text{V}/\mu\text{m}$, as photographed at (d) 47.2°C (e) 46.8°C (f) 29°C. White dotted lines in Figure 3.5(d) enclose a domain with tilted director. Thickness of the cell is $5.2\text{ }\mu\text{m}$.

3.3 Results and Discussion

defect is trapped inside the domain, and a relatively thin wall connects such a defect to the edge of the domain. The inset in Figure 3.5(e) shows a half strength defect which was trapped inside the domain. These observations indicate that the director inside the domain is tilted with respect to the plane of the sample. The photomicrograph in Figure 3.5(e) shows tilting of the director inside the domain. The tilted director field inside the domain can merge with the planar director field outside the domains only if the $1/2$ strength defects lie on the boundaries of the domains. If the defect is inside the domain, a wall across which the tilt angle changes sign has to lie between the defect and the boundary of the domain as shown in Figure 3.5(e) and Figure 3.6(c). On further cooling the texture finally becomes very dark but for a few one-strength defects as in Figure 3.5(f) suggesting that the director is now almost vertical with respect to the substrates. Further careful observations across the periphery of the tilted domain in Figure 3.5(e) show that the contrast of the texture changes gradually, indicating that the tilt angle of the director changes continuously from planar to tilted across the periphery. The side and the top views of the director orientation across the periphery are shown schematically in Figure 3.6(a) and Figure 3.6(b) respectively. The reason for choosing the specific director profile shown in Figure 3.6(a) will be clear later. The detailed director orientation is superimposed on the texture in Figure 3.6(c) which includes a boundary between tilted and non tilted domains and a half-defect connected with an inversion line inside the tilted domain as well. The variation of anchoring transition temperature, i.e., the temperature at which the nucleation of the domain starts at some particular location, is measured as a function of the applied field from the microscope observation. The anchoring transition temperature as a function of an electric field is plotted as shown in Figure 3.7. The anchoring transition temperature decreases with increasing electric field with a change of slope at $\simeq 0.1\text{V}/\mu\text{m}$, corresponding to the crossover from discontinuous to continuous anchoring transition. It may be mentioned that this is not a thermodynamic phase transition as the phase remains nematic before and after the transition; instead it is an anchoring transition bringing about a change in the director orientation. The lowering of the anchoring transition temperature on the

Temperature and electric field induced inverse Freedericksz transition in a nematogen with weak surface anchoring

application of the field is a result of the competition between the surface anchoring and dielectric response to the electric field. At a temperature lower than 48°C, the surface interaction favours a homeotropic alignment, whereas the electric field favours a planar alignment, as the dielectric anisotropy of the material is negative, whose magnitude increases with decreasing temperature.

We develop a theoretical model to account for the above observations. The Rapini-Papoular [29] form of the anchoring energy per unit surface area is given by

$$F_s = \frac{1}{2} A \sin^2 \psi_s, \quad (3.1)$$

where ψ_s is the tilt angle of \hat{n} with respect to the surface, and the positive coefficient A is the anchoring strength. By assuming that, the anchoring energy per unit area can be expressed in the form

$$F_s = \frac{u}{2} (T - T_A) \sin^2 \psi_s, \quad (3.2)$$

where $T_A \simeq 48^\circ\text{C}$ and u is positive. This means that the anchoring strength favouring planar alignment above T_A weakens rapidly as that temperature is approached from above, and changes sign at T_A to favour homeotropic anchoring whose strength rapidly increases as the temperature is lowered. A possible origin of the abrupt anchoring transition is the build-up of smectic-A type short range order near the CYTOP coated surfaces at temperatures lower than T_A , which favours the homeotropic alignment. An external electric field favours the tilt angle ψ to be zero both in the bulk and the surfaces, as the dielectric anisotropy $\Delta\epsilon$ is negative. When the sample is cooled under the action of an electric field, four possible director profiles are possible below T_A , which arises from the mutually antagonistic preferred orientations arising from the surface anchoring and dielectric energy density. This can in turn give rise to three different types of anchoring transitions. In type 1 transition, the director can have a *uniform* tilt angle $\psi(z) = \psi_s$ independent of the position z even below the transition temperature. The curvature elastic energy is zero,

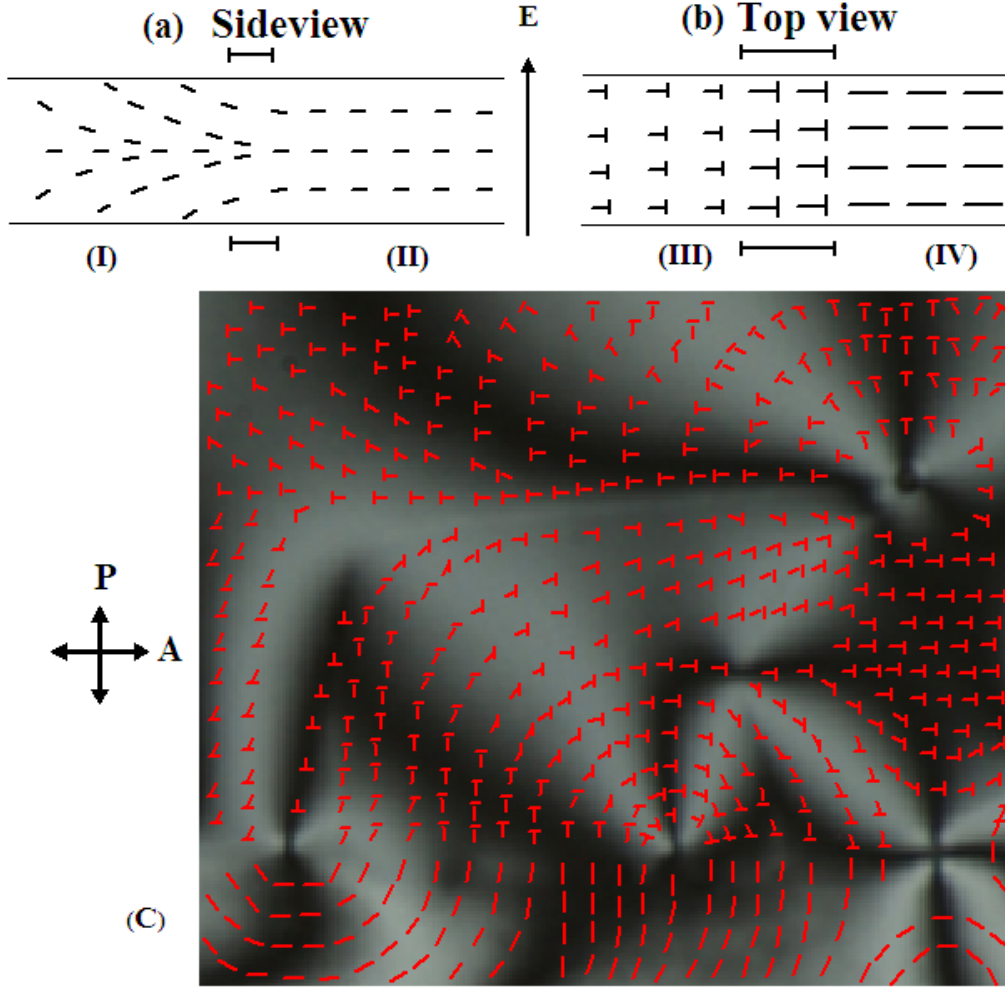


Figure 3.6: Schematic drawings of (a) the sideview and (b) the topview (say in the upper half of the cell) of the director orientation across boundary between the untilted and tilted regions. In (b) the length of the line is a measure of the projection of the director in the plane of the plate. Regions in (I) and (III) represent tilted and (II) and (IV) represent planar director orientations. (c) Part of the texture taken from Figure 3.5(e) including a half-defect connected by an inversion wall and the superimposed director orientations across the boundary between the regions with tilted and planar alignments of the director.

Temperature and electric field induced inverse Fredericksz transition in a nematogen with weak surface anchoring

and the total energy per unit area of the cell of thickness d is given by

$$F_1(T) = -\frac{\epsilon_0}{2} (\epsilon_{\parallel} \sin^2 \psi + \epsilon_{\perp} \cos^2 \psi) E^2 d + u (T - T_A) \sin^2 \psi,$$

using $\Delta\epsilon = \epsilon_{\parallel} - \epsilon_{\perp}$, we get

$$F_1(T) = -\frac{\epsilon_0}{2} [(\Delta\epsilon + \epsilon_{\perp}) \sin^2 \psi + \epsilon_{\perp} \cos^2 \psi] E^2 d + u (T - T_A) \sin^2 \psi,$$

$$F_1(T) = -\frac{\epsilon_0}{2} (\Delta\epsilon \sin^2 \psi + \epsilon_{\perp} \sin^2 \psi + \epsilon_{\perp} \cos^2 \psi) E^2 d + u (T - T_A) \sin^2 \psi,$$

$$F_1(T) = -\frac{\epsilon_0}{2} (\Delta\epsilon \sin^2 \psi + \epsilon_{\perp}) E^2 d + u (T - T_A) \sin^2 \psi,$$

$$F_1(T) = -\frac{\epsilon_0}{2} \Delta\epsilon E^2 d \sin^2 \psi - \frac{\epsilon_0}{2} \epsilon_{\perp} E^2 d + u (T - T_A) \sin^2 \psi,$$

$$F_1(T) = \left[u (T - T_A) - \frac{\epsilon_0}{2} \Delta\epsilon E^2 d \right] \sin^2 \psi - \frac{\epsilon_0}{2} \epsilon_{\perp} E^2 d. \quad (3.3)$$

As $\Delta\epsilon$ is negative, the term in the square brackets of equation 3.3 changes sign at the anchoring transition temperature,

$$T_{1at} = T_A - \frac{\epsilon_0}{2} |\Delta\epsilon| \frac{E^2 d}{u}. \quad (3.4)$$

At temperatures *above* T_{1at} the term in the square brackets of equation 3.3 will have a *positive* sign, and the energy $F_1(T)$ is minimized by $\psi = 0$, i.e., by a uniform *planar* alignment of the director throughout the cell. Below T_{1at} the term becomes *negative*, and the total energy is minimized by $\psi = \frac{\pi}{2}$, i.e., the director adopts a uniform *homeotropic* alignment throughout the cell. The anchoring transition is very similar to that in the field-free sample, and ignoring the temperature dependence of $\Delta\epsilon$, the transition point T_{1at} decreases *quadratically* with the applied field E , from T_A when $E = 0$. The fitted line as shown in Figure 3.7 takes into account the temperature dependence of

3.3 Results and Discussion

$\Delta\epsilon$. As the applied field E is increased, the dielectric energy density, which depends quadratically on the field, favours the director tilt angle $\psi(z)$ to be zero in the bulk. As we will show below, this changes the nature of the anchoring transition when the sample is cooled under relatively large values of the applied electric field E . The tilt angle $\psi(\frac{d}{2})$ in the central plane of the cell with $z = \frac{d}{2}$ can be expected to be smaller than that at the surfaces, ψ_s at $z = 0$ or d . This means that the director profile has a curvature deformation, and the elastic energy of the medium has to be taken into account. Our main interest is in the analysis of the anchoring transition, just beyond which the director field has only a splay deformation. The bulk free energy density of the medium with a *negative* $\Delta\epsilon$ is given by

$$g_2(z) = \frac{1}{2}K_{11} \left(\frac{d\psi(z)}{dz} \right)^2 - \frac{\epsilon_0}{2}\Delta\epsilon E^2 \sin^2 \psi(z). \quad (3.5)$$

As we are interested only in locating the transition at which the tilt angle $\psi(z)$ just starts deviating from 0, we linearise the Euler-Lagrange equation [30]

$$\frac{d}{dz} \left(\frac{\partial(g_2(z))}{\partial\psi'} \right) - \frac{\partial(g_2(z))}{\partial\psi} = 0,$$

$$K_{11} \frac{d^2\psi}{dz^2} - \frac{\epsilon_0|\Delta\epsilon|E^2}{2} 2 \sin \psi \cos \psi = 0,$$

for small values of ψ the above equation reads as

$$\frac{d^2\psi}{dz^2} - \frac{\epsilon_0|\Delta\epsilon|E^2}{K_{11}} \psi = 0. \quad (3.6)$$

As the sample is cooled under an electric field E in a temperature range favouring homeotropic anchoring at the surfaces located at $z = 0$ and d , we can expect that $\psi(0)$ and $\psi(d)$ start deviating from 0 at the transition.

There are two possible solutions and hence two types of anchoring transitions.

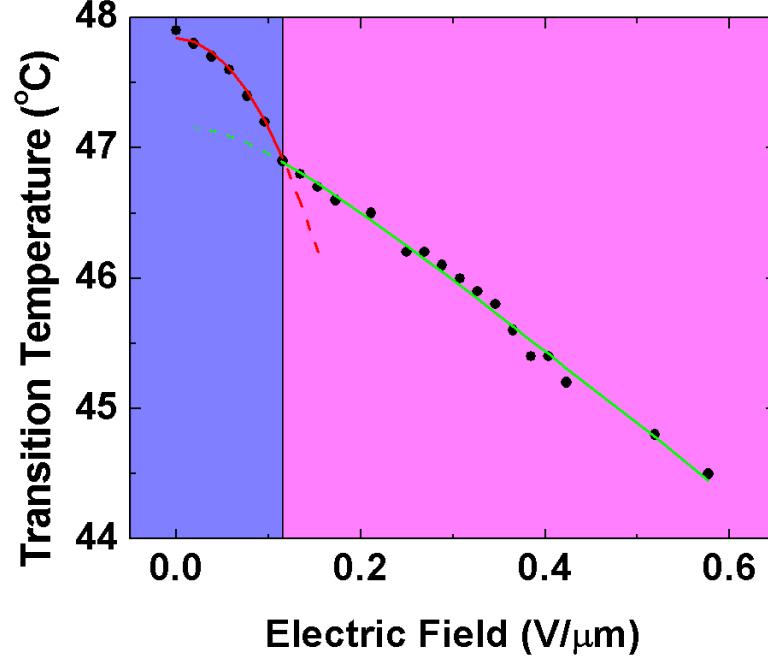


Figure 3.7: Variation of anchoring transition temperature with applied electric field. Continuous lines are best fit to the theoretical equation 3.4 and equation 3.13 with fit parameter $u = 1.6 \times 10^{-6} J/m^2 K$. The type 2 and type 1 transitions, shown by the dashed lines are superseded by transitions of the other type occurring at a higher temperatures.

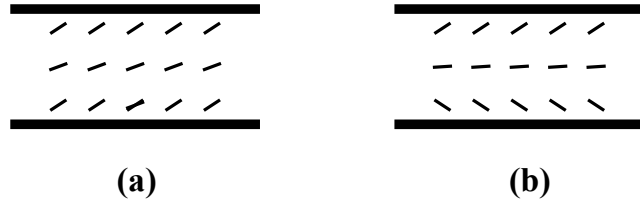


Figure 3.8: Schematic diagram illustrating the director orientations near the two surfaces and the midplane of the cell below the anchoring transition of type 2 corresponding to (a) the even and (b) the odd solutions of $\psi(z)$.

3.3 Results and Discussion

(a) both $\psi(0)$ and $\psi(d)$ are assumed to have the same sign, and we look for a solution characterized by $\psi(z) = \psi(d - z)$ as shown in Figure 3.8(a)

$$\psi(z) = \alpha \cosh(\beta(d/2 - z)), \quad (3.7)$$

where α is a measure of the amplitude of $\psi(z)$ and $\beta^2 = (\epsilon_0 |\Delta\epsilon| E^2 / K_{11})$. The surface torque balance equation at $z = 0$ reads as

$$\frac{dF_s}{d\psi(0)} = K_{11} \left(\frac{d\psi(z)}{dz} \right)_{z=0}. \quad (3.8)$$

A similar equation holds at the surface with $z = d$. Again linearizing the above equation and using the solution for $\psi(z)$,

$$\frac{d}{d\psi} \left(\frac{u}{2} (T - T_A) \psi_s^2 \right) = K_{11} \frac{d}{dz} (\alpha \cosh(\beta(d/2 - z))),$$

$$u(T - T_A) \psi_s = -K_{11} \beta \alpha \sinh(\beta(d/2 - z)),$$

$$u(T - T_A) \alpha \cosh(\beta(d/2 - z)) = -K_{11} \beta \alpha \sinh(\beta(d/2 - z)),$$

at $z = 0$ we get

$$u(T - T_A) \cosh(\beta d/2) + K_{11} \beta \sinh(\beta d/2) = 0, \quad (3.9)$$

$$u(T - T_A) = -K_{11} \beta \tanh(\beta d/2),$$

$$T - T_A = -\frac{K_{11}}{u} \sqrt{\epsilon_0 |\Delta\epsilon| E^2 / K_{11}} \tanh \left(\frac{d}{2} \sqrt{\frac{\epsilon_0 |\Delta\epsilon| E^2}{K_{11}}} \right).$$

The continuous anchoring transition temperature in this regime 2a is given by

Temperature and electric field induced inverse Fredericksz transition in a nematogen with weak surface anchoring

$$T_{2eat} = T_A - \frac{1}{u} \left(\sqrt{\epsilon_0 |\Delta\epsilon| K_{11} E^2} \right) \tanh \left(\frac{d}{2} \sqrt{\frac{\epsilon_0 |\Delta\epsilon| E^2}{K_{11}}} \right), \quad (3.10)$$

where the subscript e signifies that $\psi(z)$ is an even function. As $\tanh(x) \approx 1$ for all $x \geq 2.5$, in this regime the anchoring transition temperature essentially decreases linearly with increase of RMS value of E , reflecting the experimentally observed trend. However, as $\tanh(x) \approx x$ for very small values of x (say ≤ 0.25), the above equation actually reduces to equation 3.4 derived for the *discontinuous* anchoring transition between the planar and homeotropic states, while the derivation of the last equation above is valid only for a continuous transition, in which $\psi(z)$ just starts acquiring a non-zero value. This is an unsatisfactory feature of the even solution assumed for $\psi(z)$. Thus, even though at first sight equation 3.10 seems to mathematically describe both the experimentally found distinct regimes as far as the dependences on the electric field are concerned, it is really valid only in the regime 2 in which the transition is continuous. Indeed by equating the anchoring transition temperatures derived for the two regimes that is

$$T_{1at} = T_{2eat},$$

$$T_A - \frac{\epsilon_0}{2} |\Delta\epsilon| \frac{E^2 d}{u} = T_A - \frac{1}{u} \sqrt{\epsilon_0 |\Delta\epsilon| K_{11} E^2} \tanh \left(\frac{d}{2} \sqrt{\frac{\epsilon_0 |\Delta\epsilon| E^2}{K_{11}}} \right),$$

$$\frac{d}{2} \epsilon_0 |\Delta\epsilon| E^2 = \sqrt{\epsilon_0 |\Delta\epsilon| K_{11} E^2} \tanh \left(\frac{d}{2} \sqrt{\frac{\epsilon_0 |\Delta\epsilon| E^2}{K_{11}}} \right),$$

3.3 Results and Discussion

we get the condition for the crossover as

$$\tanh \left(\frac{d}{2} \sqrt{\frac{\epsilon_0 |\Delta \epsilon| E^2}{K_{11}}} \right) = \left(\frac{d}{2} \sqrt{\frac{\epsilon_0 |\Delta \epsilon| E^2}{K_{11}}} \right), \quad (3.11)$$

which is valid only for $E = 0$. Thus the above solution does *not* describe the experimentally found non-zero value of the crossover field satisfactorily. Hence we look for another possible solution to the linearized Euler-Lagrange equation 3.6.

(b) We now assume that $\psi(0)$ and $\psi(d)$ have opposite signs, and more generally, $\psi(z) = -\psi(d - z)$. This implies that the tilt angle of the director at the mid plane of the cell $\psi(d/2) = 0$ even in the distorted state, which is favoured by the dielectric interaction of the medium with the external field as shown in Figure 3.8(b). The solution is

$$\psi(z) = \alpha \sinh(\beta(d/2 - z)). \quad (3.12)$$

Proceeding as before, the continuous anchoring transition temperature corresponding to the above odd solution is given by

$$T_{2oat} = T_A - \frac{1}{u} \left(\sqrt{\epsilon_0 |\Delta \epsilon| K_{11} E^2} \right) \coth \left(\frac{d}{2} \sqrt{\frac{\epsilon_0 |\Delta \epsilon| E^2}{K_{11}}} \right). \quad (3.13)$$

As $\coth(x)$ also tends to the constant value 1 for large x , the essentially linear dependence of the anchoring transition temperature T_{2oat} on the RMS electric field E is recovered in the regime 2b. The condition for the crossover between the two regimes is again found by equating T_{1at} to T_{2oat} as we discussed above, and reads as

$$\coth \left(\frac{d}{2} \sqrt{\frac{\epsilon_0 |\Delta \epsilon| E^2}{K_{11}}} \right) = \left(\frac{d}{2} \sqrt{\frac{\epsilon_0 |\Delta \epsilon| E^2}{K_{11}}} \right), \quad (3.14)$$

This is satisfied for $(d/2) \sqrt{\epsilon_0 |\Delta \epsilon| E^2 / K_{11}} \approx 1.19968$. The crossover voltage is

Temperature and electric field induced inverse Freedericksz transition in a nematogen with weak surface anchoring

thus given by

$$V_{co} = E_{co}d \approx 2.4 \sqrt{\frac{K_{11}}{\epsilon_0 |\Delta\epsilon|}}. \quad (3.15)$$

The above equation shows that (i) the crossover occurs at a well-defined applied *voltage* V_{co} , which is independent of the sample thickness, and (ii) more remarkably, the crossover voltage does *not* depend on the anchoring coefficient u . It only depends on the material parameters K_{11} and $\Delta\epsilon$. The temperature dependence of the dielectric anisotropy of CCN-47 has been measured [31]. Only the bend elastic constant K_{33} of CCN-47 has been measured, and we will discuss the method of estimating K_{11} later. Using the data near the relevant temperature, the calculated value of V_{co} is $\simeq 0.5\text{V}$, which agrees extremely well with the measured value. Thus the odd solution for $\psi(z)$ gives the correct description of the director distortion below the anchoring transition in the regime 2. We fit the experimental data in the two regimes using equation 3.4 and equation 3.13 respectively. As K_{11} has not been measured for CCN-47, we estimate it using the mean field result, viz., $K_{11}(T) = K_0 S^2$, where S is the orientational order parameter whose temperature dependence has been measured [31]. The estimated value of $K_0 \simeq 7.2 \times 10^{-12}$ N. The agreement between the theoretical expressions equation 3.4 and equation 3.13 and the experimental data is highly satisfactory as shown in Figure 3.7. The overall agreement of the experimental and calculated electric field variations of the anchoring transition temperatures in both regimes show that the assumption made in equation 3.2 about the temperature variation of the anchoring energy A is appropriate for the ATr in the system studied. The calculations corresponding to the type 2b regime can be extrapolated all the way down to $E = 0$ as shown in Figure 3.7. Indeed as $\coth(x) = 1/x$ for very small values of x , for low values of E , equation 3.13 leads to a field-independent anchoring transition temperature

$$\coth \left(\frac{d}{2} \sqrt{\frac{\epsilon_0 |\Delta\epsilon| E^2}{K_{11}}} \right) = \left(\frac{2}{d} \sqrt{\frac{K_{11}}{\epsilon_0 |\Delta\epsilon| E^2}} \right),$$

3.3 Results and Discussion

now the above value should be substituted in equation 3.13. Then T_{2oat} reads as

$$T_{2oat} = T_A - \frac{1}{u} \left(\sqrt{\epsilon_0 |\Delta\epsilon| K_{11} E^2} \right) \times \left(\frac{2}{d} \sqrt{\frac{K_{11}}{\epsilon_0 |\Delta\epsilon| E^2}} \right),$$

$$T_{2oat}(E \rightarrow 0) = T_A - \frac{2K_{11}}{ud}. \quad (3.16)$$

This *hypothetical continuous anchoring transition* would have taken place when the temperature is just low enough for the gain in anchoring energy by a tilting of the director at the two surfaces to exceed the positive energy cost of the resulting elastic distortion of the director field. Of course this hypothetical transition is cut off at a higher temperature by the *discontinuous* transition of type 1. There is some similarity between this phenomenon and the nematic to isotropic (NI) transition. In the latter case, as was pointed out by de Gennes [32], the thermodynamically first order NI transition occurs at a temperature slightly higher than that of a hypothetical second order transition. The analogy is not perfect, however, as the two types of anchoring transitions discussed by us lead to two very different director distributions in the cell. It may be noted that the anchoring transition of type 2b occurs as the sample is cooled under an electric field $|E|$, with the tilt angle at the center of the sample ψ_m remaining at a value $= 0$, and the tilt angles at the two surfaces ψ_s exhibiting a transition to a non zero value. The transition occurs as the surfaces favour homeotropic alignment ($\psi_s = \frac{\pi}{2}$) with a *very weak* anchoring energy. In contrast, as described earlier, the familiar *Freedericksz transition* in the above geometry occurs if a sample with *positive dielectric anisotropy* and a *strong planar anchoring* is subjected to an appropriate electric field across the cell. This transition is characterized by $\psi_s = 0$, and $\psi(d/2)$ acquiring a non-zero value. We can thus describe the type 2 anchoring transition in our system as an *inverse - Freedericksz transition*. A schematic inverse - Freedericksz transition is shown in Figure 3.8(b). Further, in the

usual Freedericksz transition, the tilt angle at the mid plane $\psi(d/2)$ takes a maximum value, decreasing to 0 at both surfaces if the anchoring is strong, or to some finite non zero value smaller than $\psi(d/2)$ if the anchoring is weak. This necessarily requires the solution $\psi(z)$ be an even function. On the other hand, in the inverse Freedericksz transition investigated by us, the odd solution is relevant.

3.4 Conclusions

In conclusion, we have shown that the discontinuous anchoring transition of CCN-47 observed on CYTOP becomes continuous beyond a crossover voltage. The quadratic and linear variations of the anchoring transition temperature in the low voltage discontinuous and high voltage V continuous regimes with an applied field have been accounted for by a simple physical model. The latter can be described as an *inverse Freedericksz transition*. The observations also show that disclinations tend to get expelled from regions in which this transition takes place. A half-strength defect trapped inside the tilted region is connected with a tilt-inversion wall. The effect of an electric field on the homeotropic state (i.e., below T_A) and the detailed analysis of the evolution of the defects and the director profile will be discussed in chapter 4.

References

- [1] K. Takato, M. Hasegawa, M. Koden, N. Itoh, R. Hasegawa and M. Sakamoto., *Alignment technologies and applications of liquid crystal devices*, Taylor and Francis, London, 2005.
- [2] Y. Ouchi, M. B. Feller, T. Moses and Y. R. Shen, “Surface memory effect at the liquid crystal polymer interface”, *Phys. Rev. Lett.*, **68**, 3040 (1992).

REFERENCES

- [3] R. Barberi and G. Durand, “Order parameter of a nematic liquid crystal on a rough surface”, *Phys. Rev. A* **41**, 2207 (1990).
- [4] P. Sheng, “Phase transition in surface aligned nematic films”, *Phys. Rev. Lett.*, **37**, 1059 (1976).
- [5] G. P. Crawford, R. O. Crawford, S. Zumer and J. W. Doane, “Anchoring and orientational wetting transitions of confined liquid crystals”, *Phys. Rev. Lett.*, **70**, 1838 (1993).
- [6] G. Ryschenkow and M. Kleman, “Surface defects and structural transitions in very low anchoring energy nematic thin films”, *J. Chem. Phys.*, **64**, 404 (1976).
- [7] J. S. Patel and H. Yokoyama, “Continuous anchoring transition in liquid crystals”, *Nature (London)* **362**, 525 (1993).
- [8] P. Jagemalm, G. Barbero, L. Komitov, and A. Strigazzi, “Symmetry rules and temperature induced anchoring transitions”, *Phys. Lett. A* **235**, 621 (1997).
- [9] Y. Aoki, T. Watabe, T. Hirose and K. Ishikawa, “Noble orientation change with temperature in nematic liquid crystals”, *Chem. Lett.*, **36**, 380 (2007).
- [10] K. R. Amundson and M. Srinivasarao, “Liquid crystal anchoring transitions at surfaces created by polymerization induced phase separation”, *Phys. Rev. E* **58**, R1211 (1998).
- [11] B. Lin and P. L. Taylor, “Temperature driven polar anchoring transitions in nematic liquid crystals: computer simulations”, *J. Phys. II France*, **4**, 825 (1994).
- [12] H. Birecki, *Liquid crystals and ordered fluids*, Plenum, New York, Vol. 4, 853 (1984).

REFERENCES

- [13] L. Faget, S. L. Forget, P. M. Lagarde, P. Auroy and I. Dozov, “Anticonical anchoring and surface transitions in a nematic liquid crystal”, *Phys. Rev. E* **74**, 050701(R) (2006).
- [14] S. Dhara, J. K. Kim, S. M. Jeong, R. Kogo, F. Araoka, K. Ishikawa and H. Takezoe, “Anchoring transition of transversely polar liquid crystal molecules on perfluoropolymer surfaces”, *Phys. Rev. E* **79**, 060701 (2009).
- [15] J. K. Kim, F. Araoka, S. M. Jeong, S. Dhara, K. Ishikawa and H. Takezoe, “Bistable device using anchoring transition of nematic liquid crystals”, *Appl. Phys. Lett.*, **95**, 063505 (2009).
- [16] J. K. Kim, K. V. Le, S. Dhara, F. Araoka, K. Ishikawa and H. Takezoe, “Heat-driven and electric-field-driven bistable devices using dye-doped nematic liquid crystals”, *J. Appl. Phys.*, **107**, 123108 (2010).
- [17] H. Kimura, “Statistical theory of surface tension and molecular orientations in nematic liquid crystals. III. on hard flat walls”, *J. Phys. Soc. Jpn.*, **62**, 2725 (1993).
- [18] B. Jerome, “Surface effects and anchoring in liquid crystals”, *Rep. Prog. Phys.*, **54**, 391 (1991).
- [19] H. Yokoyama, “Surface anchoring of nematic liquid crystals”, *Mol. Cryst. Liq. Cryst.*, **165**, 265 (1988).
- [20] J. Bechhoefer, J. L. Duvail, L. Masson, B. Jerome, R. M. Hornreich and P. Pieranski, “Critical behaviour in anchoring transitions of nematic liquid crystals”, *Phys. Rev. Lett.*, **64**, 1911 (1990).
- [21] Y. M. Zhu, Z. H. Lu, X. B. Jia, Q. H. Wei, D. Xiao, Y. Wei, Z. H. Wu, Z. L. Hu, and M. G. Xie, “Anchoring transition of liquid crystals on crown ether monolayers”, *Phys. Rev. Lett.*, **72**, 2573 (1994).
- [22] M. Monkade, M. Boix and G. Durand, “Order electricity and oblique nematic orientation on rough solid surfaces”, *Europhys. Lett.*, **5**, 697 (1988).

REFERENCES

- [23] V. G. Nazarenko and O. D. Lavrentovich, “Anchoring transition in a nematic liquid crystal composed of centrosymmetric molecules”, *Phys. Rev. E* **49**, R990 (1994).
- [24] J. Zhou, D. M. Collard, J. O. Park and M. Srinivasarao, “Control of the anchoring behavior of polymer dispersed liquid crystals: effect of branching in the side chains of polyacrylates”, *J. Am. Chem. Soc.*, **124**, 9980 (2002).
- [25] Y. Choia, Y. Leeb, H. Kwonb, S. D. Lee, “Optical detection of the ligand receptor binding by anchoring transitions of liquid crystals”, *Mater. Sci. Eng.*, **C 24**, 237 (2004).
- [26] K. Okano, “Anisotropic excluded volume and alignment of nematic liquid crystal in a sandwich cell”, *Jpn. J. Appl. Phys.*, **22**, L343 (1983).
- [27] K. Okano, “Alignment of a liquid crystal on an anisotropic substrate”, *Jpn. J. Appl. Phys.*, **21**, L109 (1982).
- [28] J. Nehring and A. Saupe, “On the schlieren texture in nematic and smectic liquid crystals”, *J. Chem. Soc., Faraday Trans. II*, **68**, 1 (1972).
- [29] A. Rapini, M. Papoular, “Distortion dune lamelle nmatique sous champ magnétique conditions dancrage aux parois”, *J. Phys. Colloq. France* **30**, C4-54 (1969).
- [30] E. G. Virga, *Variational theories for liquid crystals*, Chapman and Hall, London, 1994.
- [31] S. Dhara, N. V. Madhusudana, “Physical characterisation of 4'-butyl-4-heptyl- bicyclohexyl-4-carbonitrile”, *Phase Transitions*, **81**, 561 (2008).
- [32] P. G. de Gennes, *The Physics of liquid crystals*, 2nd Ed. Clarendon, Oxford, 1993.

4

Effect of an electric field on defects in a nematic liquid crystal with variable surface anchoring

4.1 Introduction

In the previous chapter we have studied the effect of electric field on the discontinuous anchoring transition both experimentally and theoretically. In this chapter we will discuss the effect of electric field on the defects in the same system.

As we know liquid crystals are highly anisotropic materials. Therefore, liquid crystals exhibit a variety of colorful textures under polarizing optical microscope [1]. These textures are useful for the preliminary characterization of the liquid crystalline phases. For example, nematic liquid crystals generally exhibit schlieren textures. Cholesteric and smectic liquid crystals exhibit fingerprint and focal conic textures. These textures are composed of different types of defects [2, 3]. In nematics the characteristic defects are disclinations which are basically line-defects. In smectics, in addition to the focal conic defects, dislocations exist as line defects, although they can not be seen optically. The line defects are topological defects in order parameter space. They

Effect of an electric field on defects in a nematic liquid crystal with variable surface anchoring

are also seen in various other systems: for example, vortices in superfluid helium, dislocations in crystals [4]. The disclinations seen in nematics have been studied extensively, both theoretically and experimentally [5–15]. Two disclinations attract each other when they are ‘unlike’ and repel when they are ‘like’, mimicking the interactions between electrical charges. Nehring and Saupe [6] in their classic paper presented detailed observations made on schlieren textures of nematics and calculated the force of interaction between two disclinations. They showed that annihilation of unlike half-strength defects and creation of integer-strength defects from merger of like half-strength defects sometimes occur very near the nematic-isotropic phase transition temperature. Lavrentovich *et al.* [16] have studied both theoretically and experimentally different types of defects and their structures in various liquid crystals.

There are also several experimental and theoretical studies on the defect-antidefect annihilation dynamics in nematic liquid crystals [17–36]. The annihilation dynamics have been studied as a functions of time, when the director field evolves after rapid quenching from isotropic to nematic phase. Bogi *et al.* have studied the influence of surface anchoring on the annihilation dynamics of two parallel $\pm 1/2$ defects. They found that when the defect lines are far from each other, the elastic interaction is completely screened by anchoring energy [17]. The dynamics of $\pm 1/2$ defects under an external electric field was investigated by Blanc *et al.* [18]. They found that the relaxation is governed by the π wall connecting two opposite charges and that the $+1/2$ defects move faster than $-1/2$ defects.

In the previous chapter we studied the effect of electric field on the discontinuous anchoring transition of CCN-47 on CYTOP. This discontinuous anchoring transition occurs from planar to homeotropic at $\sim 47.5^\circ\text{C}$ on cooling and the reverse transition at $\sim 50.6^\circ\text{C}$ on heating [37, 38]. In the cooling mode, the sample exhibits a texture with a large number of $\pm 1/2$ defects above $\sim 47.5^\circ\text{C}$, and we have reported earlier about the defect-antidefect correlations in this system [39]. In this chapter we present merging of two like half-strength defects to form integer strength (± 1) defects and annihilation of two unlike half-strength defects when the director tilts away from the planar

4.2 Experimental

alignment. The tilting occurs below the anchoring transition temperature under applied electric fields which are large enough to change the transition to continuous one. We show that the defects of strength 1 which are seen just below this temperature have a new structure, with either a + or a - point defect located at the midplane of the sample, and associated with two boojums lying at the two surfaces. Their number density decreases as the temperature is reduced. At temperature $\sim 6^\circ$ below the anchoring transition temperature, the anchoring strength for homeotropic alignment grows to a large value, and sample leads to the formation of umbilics. We found that these field-induced defects follow the dynamic scaling laws found earlier for both umbilics and schlieren defects near the NI transition temperature.

4.2 Experimental

The cell preparation and experimental method is same as discussed in the previous chapter. We have used olympus image analysis software to calculate defect density and defect-antidefect separation.

4.3 Results and Discussion

4.3.1 Textures without an electric field

In this section we present the textures observed under polarizing optical microscope in the absence of an electric field. A typical planar texture observed at temperature 52.2°C is shown in Figure 4.1(a). It is evident from the planar texture that the compound exhibits mostly half strength disclinations and a few disclinations of strength 1. As we cool the sample further, at temperature 47.5°C the nucleation of dark domains were observed in various places of the sample. The size of the domain was increasing even the temperature of the sample was held fixed. The growth of dark domains in the sample is shown in the Figure 4.1(b). The homeotropic state of the sample

Effect of an electric field on defects in a nematic liquid crystal with variable surface anchoring

is shown in Figure 4.1(c) and the details of this discontinuous anchoring transition are already discussed in the previous chapter. The system also exhibits a large hysteresis of a few degrees celsius in the anchoring transition temperature. We first observed textures on heating the sample at a rate of $1^{\circ}\text{C}/\text{min}$ from the homeotropic state. The homeotropic state of the sample at temperature 50°C is shown in Figure 4.2(a). During heating the sample starts to undergo the discontinuous anchoring transition from homeotropic to planar at temperature 50.6°C . The texture depicting the discontinuous anchoring transition from homeotropic to planar state is presented in Figure 4.2(b). Only integer strength defects with many walls associated with homeotropic to planar transition are seen. Defects connected with walls are shown in Figure 4.2(c). These integer strength defects expected in the sample as the director reorients from homeotropic to planar via tilted orientation. We also noticed that the defect density is much lower compared with that of the field induced umbilic defects which will be discussed later. On further heating, the dark brushes become comparatively thicker as shown in Figure 4.2(d). In several heating cycles, we found that the defects appear at the same locations which means that the director distortion starts at the glass plates.

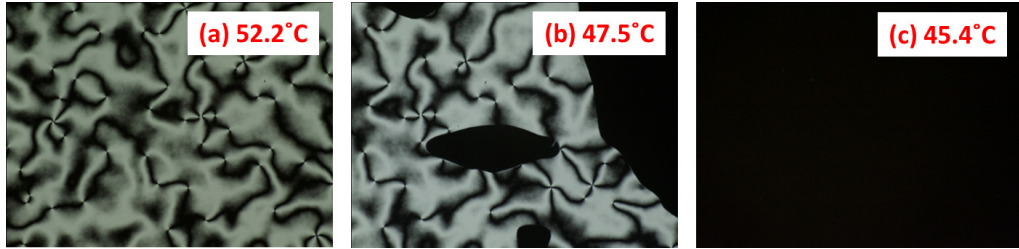


Figure 4.1: (a) Photomicrographs of the texture at 52.2°C (b) during discontinuous anchoring transition at 47.5°C (c) homeotropic texture at 45.4°C . All the above observations were made in the absence of an electric field in a $5.2\text{ }\mu\text{m}$ thick cell.

4.3 Results and Discussion

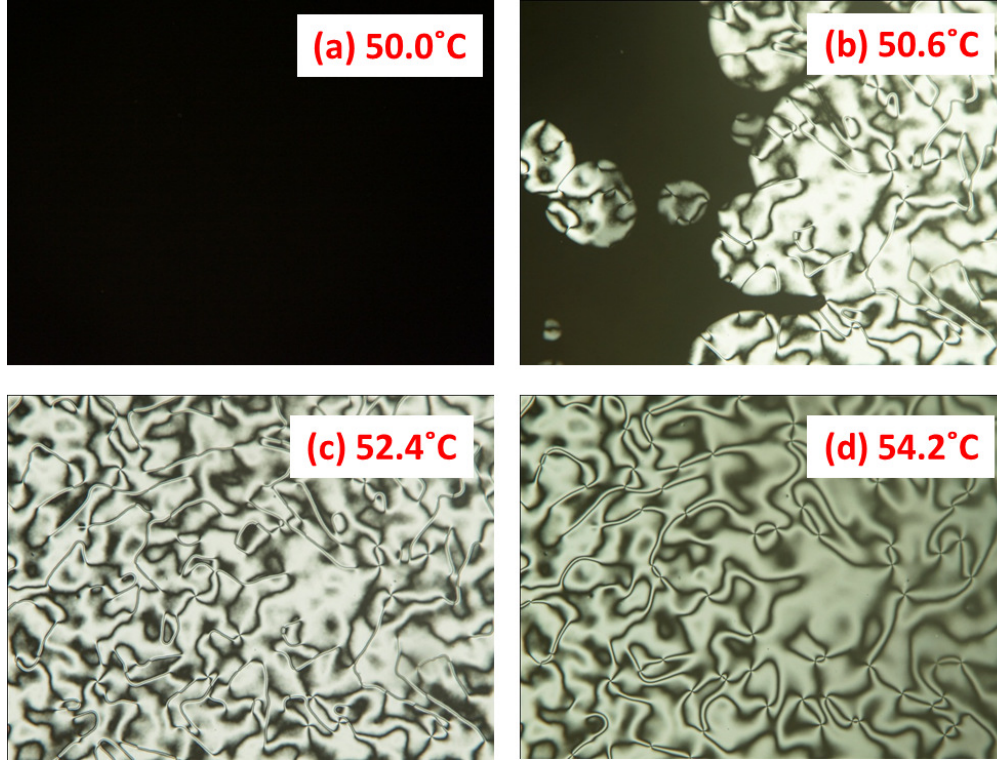


Figure 4.2: Photomicrographs showing discontinuous anchoring transition on heating the sample from homeotropic state (a) homeotropic texture at 50°C (b) during the discontinuous anchoring transition at 50.6°C (c) planar texture at 52.4°C and (d) at 54.2°C. All the above observations were made in the absence of an electric field a 5.2 μm thick cell.

4.3.2 Textures with electric field

As we discussed in the previous section CCN-47 shows discontinuous anchoring transition on perfluoropolymer treated surface at temperature 47.5°C, while the sample cooled from isotropic to nematic. When voltage was applied to the sample, no observable change in the texture is noticed at the temperature above the anchoring transition temperature as shown in Figure 4.3(a). But as the temperature approaches anchoring transition temperature the nature of the transition changes from discontinuous to continuous depending on

Effect of an electric field on defects in a nematic liquid crystal with variable surface anchoring

the strength of the applied voltage. The voltage at which the discontinuous anchoring transition becomes continuous is called cross-over voltage. Here the value of the cross-over voltage is $\sim 0.5V$ as mentioned in the previous chapter. When the temperature is reduced to anchoring transition point, some domains with lower birefringence start growing in the sample as shown in Figure 4.3(b). These lower birefringent domains corresponds to the signature of the continuous anchoring transition. At this continuous anchoring transition the director starts tilting away from the surfaces. While transition is being taking place, like half-strength defects merge to form defects with integer-strength (± 1) or are expelled from the tilted domains on the other hand unlike half strength disclinations annihilate each other as shown in Figure 4.3(c). Only integer strength defects survive the continuous anchoring transition as shown in Figure 4.3(d). Further we study how a new type of defect structure is created by opposite tilts induced by the field at the two surfaces.

Now we concentrate on disclinations of strength ± 1 , which survive the continuous anchoring transition under the applied external electric field. The stability of the (nontopological) ± 1 disclinations arises because of the escape of the director in the third direction [7], removing the core of the line defect. Hereafter we call the ± 1 disclination line as line defect, although it contains no orientational singularity or core. However, they are lines connecting two point defects at the top and bottom surfaces as described in the following. The director configurations of $+1$ and -1 line defects confined to a cell of finite thickness are shown in Figure 4.4 and Figure 4.5 respectively. The top and side views of $+1$ defect are sketched in Figure 4.4. The director tilts away from the plane of the glass plates, the nail heads being at lower positions than the tips in Figure 4.4(a). The director configuration has rotational symmetry about the defect line as shown in Figure 4.4(b) and it incorporates a partial ‘ $+1$ point’ disclination at the lower glass plate and a partial ‘ -1 point’ disclination at the upper surface. Such surface point defects are called boojums [41]. If the surface strength is finite, the core (a virtual core) of the boojums is located at the boundary or at some distance from it. These boojums cannot move inside the nematic bulk because of the boundary conditions. A necessary

4.3 Results and Discussion

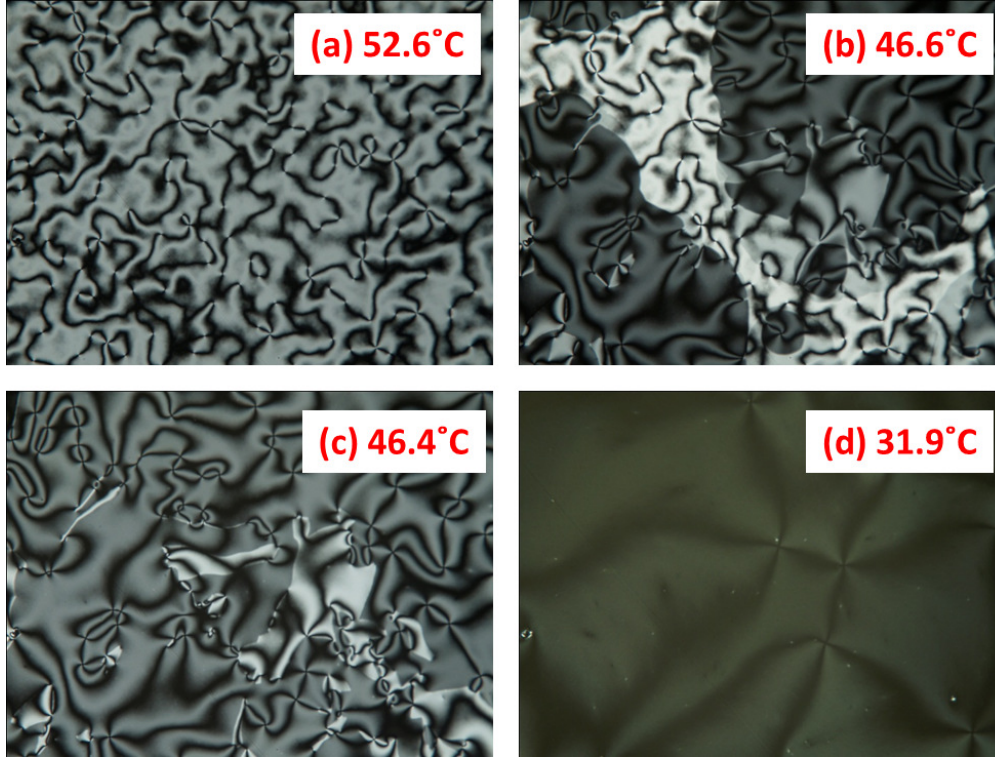


Figure 4.3: Photomicrographs showing anchoring transition under an applied ac voltage of 0.9V (above cross-over field) and frequency 3.11 KHz during cooling (a) at 52.6°C (b) showing a continuous anchoring transition at 46.6°C (c) at 46.4°C (d) dark field of view with a few four brush defects at 31.9°C. Cell thickness 5.2 μm .

condition for formation of boojums is that the director is either tangential or tilted with respect to the surface so that the defect is characterized. The top view of the -1 line defect is shown in Figure 4.5. There is no rotational symmetry about this line defect, along which there is a 2-fold axis. As we move along the 45° line from lower right to upper left quadrant, the director twists in an anti-clockwise fashion. Clock wise twist is seen when we look along the lower left to upper right quadrant. On the other hand, there is only splay-bend distortion along the vertical and horizontal planes. Again there are partial point defects or boojums of opposite sign at the upper and lower glass plates.

Effect of an electric field on defects in a nematic liquid crystal
with variable surface anchoring

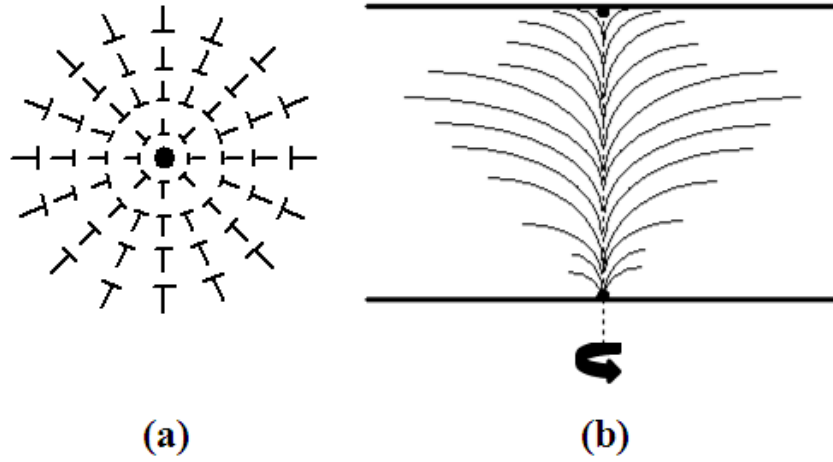


Figure 4.4: Schematic representation of director orientations of a +1 defect line: (a) top view (b) side view.

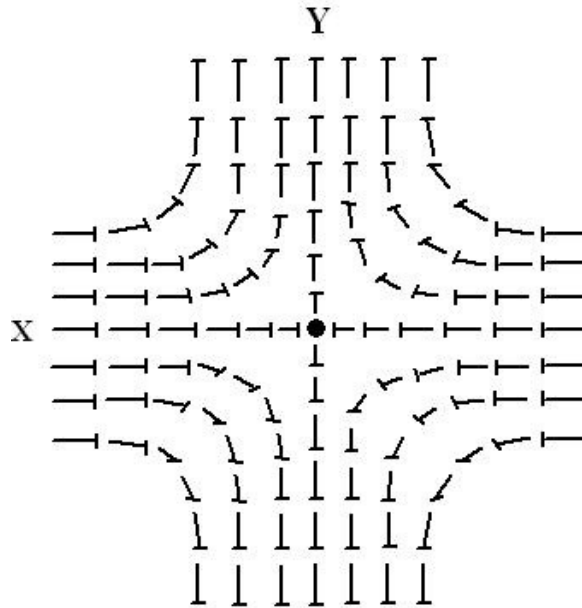


Figure 4.5: Schematic representation of director orientations in the top view of a -1 disclination line.

We now focus our attention on a small region of the sample and carefully

4.3 Results and Discussion

observe the merging and annihilation processes. We noticed that at 44.1°C some of the half-strength defects had already merged to form defects of strength one as shown in Figure 4.6. There are still some half-strength defects which are connected by the inversion walls. Green arrows in the Figure 4.6(a) and Figure 4.6(b) shows the inversion wall which connect half-strength defects. As the temperature reduces the half-strength defects moves closer whereas positions of one-strength defects are almost fixed as shown in Figure 4.6(b) and Figure 4.6(c). The half strength defects of the same sign moves closer in order to reduce the energy of the inversion wall. Finally, two like half-strength defects merge together and create a defect of strength one as shown in Figure 4.6(d). In the present case our observations show that it is a defect of strength $+1$. On the other hand two unlike half-strength defects are annihilated as shown in Figure 4.6(d). We also noticed that in a given pair of annihilating defects, the $+1/2$ defects moves faster towards the $-1/2$ defect as reported by Blanc *et al* [18]. Finally, no half-strength defects remain in the texture as shown in Figure 4.6(d). When we switch off the electric field at any temperature below that of the anchoring transition, homeotropic domains are formed immediately and the field of view becomes completely dark recovering the discontinuous anchoring transition.

As we know if the homeotropic anchoring at the surfaces is strong and appropriate magnitude of an electric field is applied along the direction of director of a nematic with negative dielectric anisotropy induces the usual Freedericksz transition. In the present case, the director starts tilting at the *midplane* of the sample and in view of the degeneracy in azimuthal angles, line defects of integral strength which are somewhat similar to those described above are formed in the sample. The strong homeotropic anchoring at the surfaces ensure that no boojums are formed at the ends of the line defects, which are called *umbilic* defects [2]. We describe observations on umbilic defects at low temperatures in section 4.3.3.

In our sample, the boundary condition changes from planar to homeotropic below the anchoring transition temperature as we cool the sample from isotropic to nematic. This is presumably because of the build up of

**Effect of an electric field on defects in a nematic liquid crystal
with variable surface anchoring**

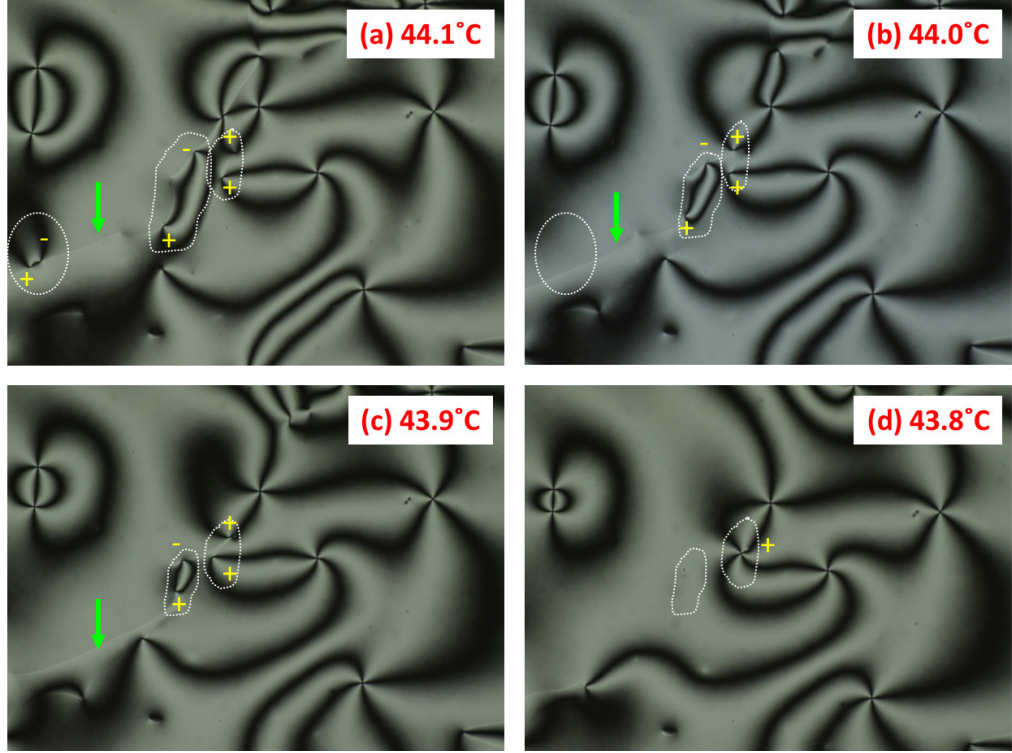


Figure 4.6: Merging of $\pm 1/2$ defects under the applied ac voltage of 1.5V (a) pairs of half-strength defects are shown with enclosed dotted white lines at 44.1°C some of the half-strength defects have already merged to form integer-strength defects; (b) one pair of unlike defects (enclosed with dotted lines at the left) annihilated at 44°C (c) both the unlike and like half-strength defects approach each other (d) like half-strength defects merge to form an integer defect and unlike half-strength defects are annihilated. White wispy lines pointed by green arrows are inversion walls.

smectic-A like short range order on the flat surfaces of the cell walls. As we discussed earlier the anchoring strength is weak close to the anchoring transition temperature. At this stage we can pose a question ourselves stating that what will be the structures of the defects of strength 1 when the director tilts oppositely at the surfaces below the continuous anchoring transition temperature under the ac electric field ? The answer to the above question is as follows, In the case of a disclination line of strength +1, there are two

4.3 Results and Discussion

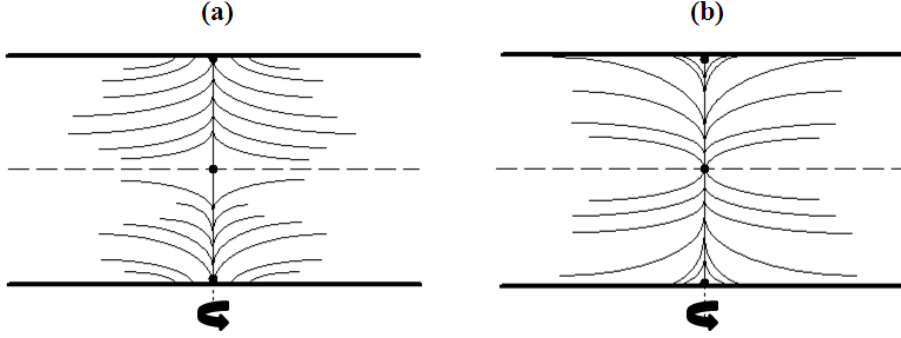


Figure 4.7: (a) Schematic representation of two possible director configurations with opposite tilts at the two surfaces in the case of $+1$ defect.

possibilities consistent with the opposite tilts at the two surfaces: (i) the boojum with negative sign is in Figure 4.7(b) can detach from the surface and become a point disclination with strength -1 which settles down at the center of the sample, and a new boojum with positive sign is formed at the surface. Thus the disclination line now will have a collapse of the director occurring in opposite directions in the two halves of the cell as shown in Figure 4.7(a). (ii) Another possibility for the positive boojum of Figure 4.7(b) is to shift to the midplane as a $+1$ point defect, and a boojum of negative strength is to form at the surface as shown in Figure 4.7(b). Both of these field induced structures have rotational symmetry about the line defects and exhibit similar dark brushes between crossed polarizers. As the temperature reduces, the tilt angle near the surfaces increases and the over all brightness decreases.

The change in the director field in the presence of the external field can be expected to be more complicated in the case of a line defect of strength -1 . The expected director patterns in the XZ and YZ planes which had only splay-bend distortions above the anchoring transition temperature are shown in Figure 4.8. Again there are only splay-bend distortions in these two planes, but it is clear that in any given quadrant, the twist distortion of the director changes sense between the upper and lower halves of the sample. The director structure here is more complicated than that of the point defect at the center of the sample as shown in Figure 4.7(a) and (b). The projection of the director

Effect of an electric field on defects in a nematic liquid crystal with variable surface anchoring

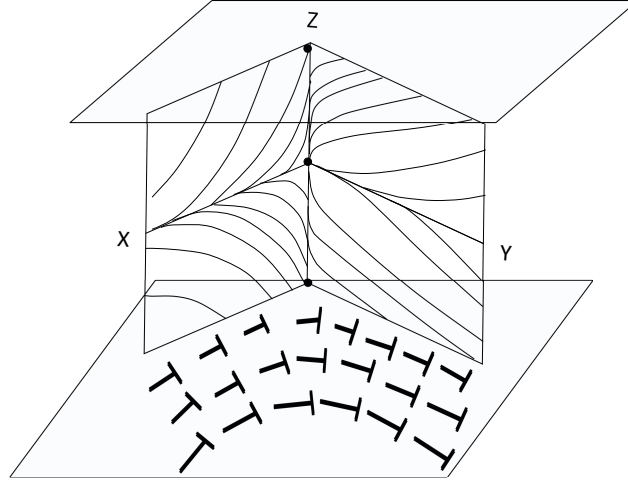


Figure 4.8: Some cross sections of the director configuration of -1 disclination, with opposite tilts at the two surfaces.

field in the XY-plane in one of the quadrants is shown to emphasize that the optical pattern between crossed polarizers will be similar to that of the line defect of -1 strength in the planar aligned sample. The overall pattern again has 2-fold symmetry about the line defect as before. When the +1 and -1 line defects with these modified structures approach each other, it will be energetically less expensive if the +1 defect with structure as in Figure 4.7(a) approaches the -1 defect along the Y-axis, while that with the structure as shown in Figure 4.7(b) approaches along the X-axis. The opposite tilts of the director at the two plates below the continuous anchoring transition temperature in the presence of sufficiently high external electric field gives rise to the new type of structures illustrated above. Both line defects of +1 and -1 strength will have point defects at the midplane of the cell, apart from the two boojums at the two surfaces. The structures are new, which appears because of the opposite tilts at the two surfaces realized by the anchoring transition under an electric field: the field free line defects are not expected to have the point defects at the center. The umbilic defects seen above the Freedericksz threshold in materials with negative dielectric anisotropy in cells with strong homeotropic boundary conditions do not have the boojums. The

4.3 Results and Discussion

interactions between the new types of defects in our sample can be expected to be dominated by the point defects at the midplane of the cells.

Although the structures of both +1 and -1 line defects change substantially below the inverse Freedericksz transition point, they continue to produce four dark brushes between crossed polarizers. On cooling the sample further, the number of these defects reduced due to the mutual annihilation of defects of opposite strength as they approach each other as described above. A typical texture of the sample taken on cooling to 31.9°C, which is much lower than the anchoring transition temperature is shown in Figure 4.3(d). The texture appears dark with a few four-brush defects remaining in the background.

4.3.3 Dynamics of umbilic defects

The study of the dynamics of topological defects created by symmetry-breaking phase transitions has received considerable attention in cosmology, particle physics and condensed matter physics. Liquid crystals are one of the most valuable and suitable systems to study coarsening dynamics of topological defects. Different kinds of string like (twist) and point like (wedge) disclinations can easily be created and controlled in specially treated cells. The dynamics of defects can also be observed easily in optical microscope. Further, the experimental results obtained in liquid crystals have universality. Therefore, liquid crystals can be used for exploring the similar scenario encountered in other areas of physics.

The coarsening dynamics of topological defects, which belongs to nonconserved order parameter, in general exhibits a certain scaling law, namely, the defect density or line density (ρ). The defect density (ρ) scales with time as $t^{-\nu}$. Here ν is the scaling exponent and it depends on spatial dimensionality d : for string like defects $\nu=1$ and $\nu=0.5$ for $d = 3$ and $d = 2$ respectively. For point like defects $\nu=1$ at $d = 3$ [11, 20–24]. Experimental results obtained in some low molecular weight liquid crystals with string like [20, 25–29] and point like defects [11, 13] and from polymer liquid crystal with string like [31] and point like defects [32, 33] are in good agreement with the theoretical expectations.

Effect of an electric field on defects in a nematic liquid crystal with variable surface anchoring

However, some investigations show different results. Orihara and Ishibashi [25] have studied the collective motion of an assembly of disclinations in twisted nematic cell and dynamical scaling law was found. Nagaya *et al.* [12] have developed an important experimental technique to generate wedge disclinations. Using these technique they could study the individual motion of two dimensional wedge disclinations. Yurke *et al.* [28] have studied the coarsening dynamics of disclinations in the nematics subject to a rapid pressure-jump quenching. Furthermore, they investigated an analogy between the disclinations and the cosmological defects. Nagaya *et al.* [13] have also reported to the coarsening dynamics of the point like defects in the two dimensional system by utilizing the method developed by them [12]. The system obeys the scaling law and the exponents obtained experimentally agrees well with the dimensional analysis. In recent past, Pargellis *et al.* [11] found a region where the distance D between a largely separated defect pair decreased linearly with time in the smectic-C phase of a thin liquid crystal film, which was contrasted with the other region of D proportional to the square root of time for a similar separation. The linear time dependence was also reported for a hybrid aligned nematic cell by Lavrentovich and Rozhkov [30]. Wang *et al.* [31] have studied the coarsening dynamics of string like topological defects and the shrinkage and annihilation of individual defect loops in a nematic polymer liquid crystal and the results are compared with the results obtained in case of low molecular weight liquid crystals.

We studied the dynamics of the field induced umbilics in the same system (sample and cell) that emerge from the homeotropic state when the anchoring energy is relatively strong. When a nematic liquid crystal with $\Delta\epsilon < 0$ is subjected to homeotropic boundary conditions as well as applied electric field. If the applied voltage exceeds Freedericksz threshold, the director reorient to planar configuration. Under these conditions only two types of director deformations can be found which are similar to schlieren point defects of strength ± 1 . These deformations are called Umbilic defects. Umbilic defects always exist in integer strength. The umbilic defects differs from schlieren defects only at the core at which the director tilts continuously towards the substrate normal. Umbilic defects have experimentally been observed before

4.3 Results and Discussion

[34, 35] and their annihilation dynamics is the subject of this section. The annihilation dynamics of umbilic defects have been studied by Dierking *et al.* [36] in a commercially available mixture (ZLI-2806) in cells treated with JALS-204-R40. The dielectric anisotropy of ZLI-2806 is $\Delta\epsilon < -4.8$. Umbilic defects were induced by square wave generator in connection with high voltage amplifier. The obtained scaling exponents ν and α for defect density $\rho(t)$ and pair separation $D(t)$ are well agreed with theoretically predicted values. They have shown that the values of ν and α does not vary with external parameters such as electric field amplitude, frequency, cell gap and temperature. Their experimental results give evidence of the universality of scaling relations for the annihilation of the topological defects in liquid crystals, extended to umbilical defects and their annihilation dynamics under applied external field. In the present study we kept the sample at temperature 42°C i.e., whole sample is in homeotropic state. At this stage we connected function generator (Tektronix) to the cell and a sinusoidal wave of amplitude 4V with frequency of 3.11 KHz was applied to the cell to induce umbilic defects in the sample. As we discussed in previous chapter the anchoring strength A is about 10^{-5}J/m^2 at this temperature. Further, the bend elastic constant of CCN-47 K_{33} is 0.8pN [40]. Thus, the extrapolation length $K_{33}/A \simeq 0.08\mu\text{m}$, which is much smaller than the sample thickness $d = 5.2\mu\text{m}$. The anchoring energy is effectively *strong*, and the applied field induces umbilic defects above the Freedericksz threshold as we discussed earlier.

In the present case we recorded a video of evolution of umbilic defect using Olympus Image Analysis software and then converted it into frames. Using the same software we could calculate defect density and defect-antidefect separation from each frame. Typical photographs showing the evolution of umbilic defects with time are shown in Figure 4.9. It is seen that initially there are a large number of ± 1 umbilic defects as shown in Figure 4.9(a), which mutually annihilate with the progress of time to reduce the number density is shown in Figure 4.9 (b) to (d). Finally, a small number remains static due to the surface irregularities or impurities as shown in Figure 4.9(d). The director field around a +1 strength umbilic defect is shown schematically

Effect of an electric field on defects in a nematic liquid crystal
with variable surface anchoring

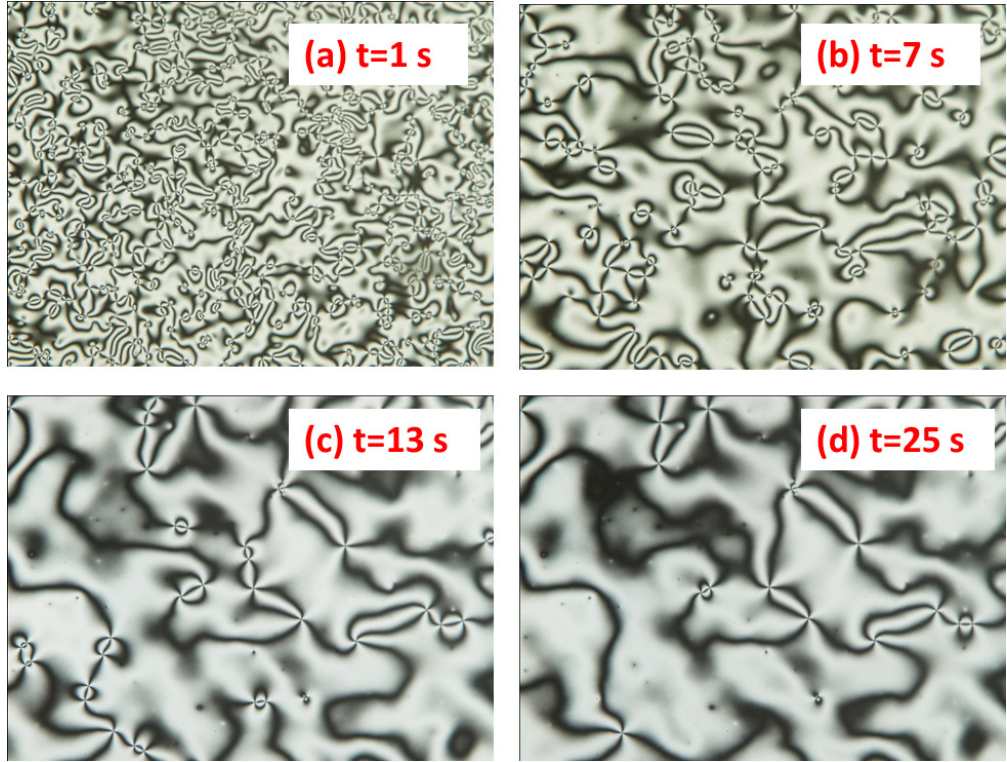


Figure 4.9: Textures (at 42°C) showing umbilic defects under an applied voltage of amplitude 4V and frequency 3.11 KHz: elapsed time after the application of the field: (a) 1 sec (b) 7 sec (c) 13 sec (d) 25 sec; cell thickness $d = 5.2\mu\text{m}$.

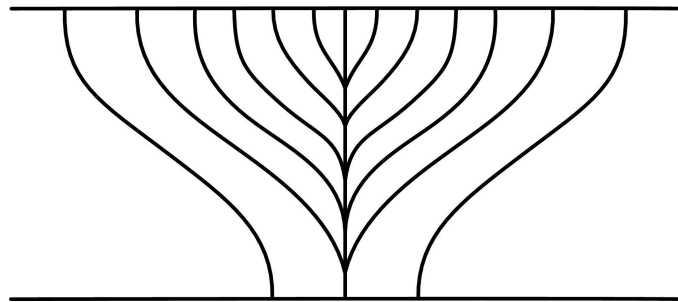


Figure 4.10: Schematic representation of director field of an umbilic defect of +1 strength generated by an electric field. Note the absence of boojums.

4.3 Results and Discussion

in Figure 4.10. Diagrams showing the variations of defect density $\rho(t)$ and the inter defect separation $D(t)$ as functions of time are shown in Figure 4.11(a) and Figure 4.11(b) respectively. According to the theoretical predictions [12] the defect density and the inter defect separation obey the following scaling laws:

$$\rho(t) \propto t^{-\nu}, \quad (4.1)$$

with $\nu = 1$, and

$$D(t) \propto (t_0 - t)^\alpha, \quad (4.2)$$

where $t_0 - t$ is the time to annihilate and $\alpha = 0.5$. A nonlinear least squares fitting program was used to fit the experimental data. The best fits to $\rho(t)$ and $D(t)$ are shown in Figure 11(a) and Figure 11(b) respectively. The fit parameters are obtained as $\nu = 1.1 \pm 0.05$, and $\alpha = 0.55 \pm 0.01$, and are very close to the theoretical predictions. Similar values of the above two exponents have also been reported by Dierking *et al.* [36]. This study verifies previously reported results and suggests that irrespective of the material and alignment layers these critical exponents for umbilic defects are universal.

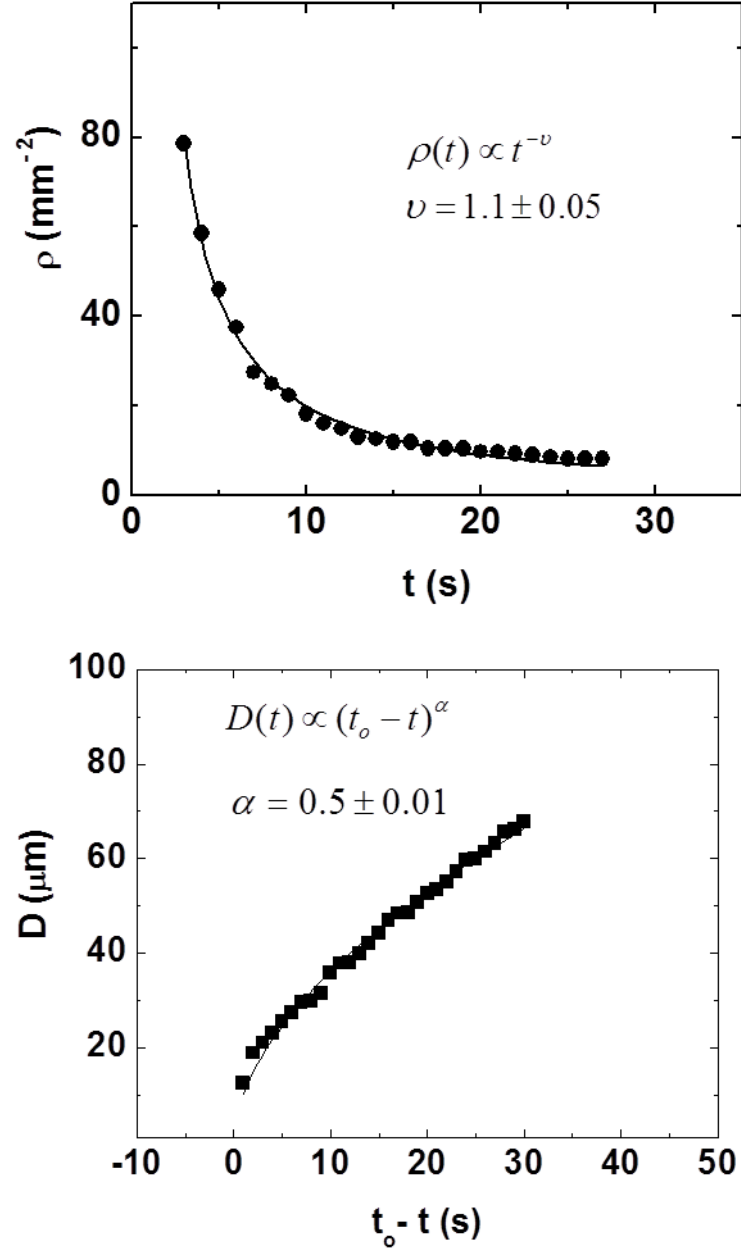


Figure 4.11: (a) Time evolution of defect density $\rho(t)$. The continuous line is the best fit to the theoretical equation 4.1 with the exponent $\nu = 1.1 \pm 0.05$. (b) Time evolution of defect pair separation $D(t)$. The continuous line is the best fit to the theoretical equation 4.2 with the exponent $\alpha = 0.55 \pm 0.01$.

4.4 Conclusions

In conclusion, we have studied the evolution of line defects of strength 1 in a planar aligned sample to new types of defects, consisting of point defects of integral strength at the midplane, and boojums at the surfaces, as the sample is cooled below a continuous anchoring transition temperature under an electric field. We have recorded the annihilation of half-strength defects of opposite sign and creation of integer-strength defects from those of the same sign. We have also studied the dynamics of the umbilic defects formed under the action of an electric field on the homeotropically aligned state at a sufficiently low temperature, and found that the exponents for the time dependences of the defect density and the inter defect separation are consistent with the results of previous studies.

References

- [1] I. Dierking, *Textures of liquid crystals*, Wiley-VCH Verlag GmbH and Co. KGaA Weinheim, 2003.
- [2] P. G. de Gennes, *The physics of liquid crystals*, 2nd ed Clarendon, Oxford, 1993.
- [3] S. Chandrasekhar, *Liquid crystals*, Cambridge University Press, Cambridge, 1977.
- [4] P. M. Chaikin and T. C. Lubensky, *Principle of condensed matter physics*, Cambridge University Press, Cambridge, 1998.
- [5] F. C. Frank, “Liquid crystals: on the theory of liquid crystals”, *Disc. Faraday Soc.*, **25**, 19 (1958).
- [6] J. Nehring and A. Saupe, “On the schliere texture in nematic and smectic liquid crystals”, *J. Chem. Soc., Faraday Trans. II*, **68**, 1 (1972).

REFERENCES

- [7] P. E. Cladis and M. Kleman, “Non-singular disclinations of strength $S=+1$ in nematics”, *J. Phys. (Paris)*, **33**, 591 (1972).
- [8] P. E. Cladis, W. V. Saarloos, P. L. Finn and A. R. Kartan, “Dynamics of line defects in nematic liquid crystals”, *Phys. Rev. Lett.*, **58**, 222 (1987).
- [9] R. B. Meyer, “On the existence of even indexed disclinations in nematic liquid crystals”, *Phil. Mag.*, **27**, 405 (1973).
- [10] M. Kleman, *Advances in liquid crystals*, Ed. G. H. Brown, Academic Press, New York, Vol. **1** 1975.
- [11] A. Pargellis, N. Turok and B. Yurke, “Monopole antimonopole annihilation in a nematic liquid crystal”, *Phys. Rev. Lett.*, **67**, 1570 (1991).
- [12] T. Nagaya, H. Hotta, H. Orihara and Ishibashi, “Observation of annihilation process of disclinations emerging from bubble domains”, *J. Phys. Soc. Jpn.*, **60**, 1572 (1991).
- [13] T. Nagaya, H. Hotta, H. Orihara and Ishibashi, “Experimental study of the coarsening of $+1$ and -1 disclinations”, *J. Phys. Soc. Jpn.*, **61**, 3511 (1992).
- [14] K. Minoura, Y. Kimura, K. Ito, R. Hayakawa and T. Miura, “Annihilation of a wedge disclination pair in a hybrid aligned nematic cell”, *Phys. Rev. E* **58**, 643 (1998).
- [15] C. M. Dafemous, “Disclinations in liquid crystals”, *Quart. J. Mech. Appl. Math (UK)*, **23**, S49 (1970).
- [16] O. D. Lavrentovich, P. Pasini, C. Zannoni, S. Zumer, *Defects in liquid crystals: computer simulations, theory and experiments* (Kluwer Academic Publishers), NATO Science Series Mathematics, Physics and Chemistry, Vol. **43** 2001.
- [17] A. Bogi, P. M. Lagarde, I. Dozov and M. Nobili, “Anchoring screening of defects interaction in a nematic liquid crystal”, *Phys. Rev. Lett.*, **89**, 225501 (2002).

REFERENCES

- [18] C. Blanc, D. Svensek, S. Zumer and M. Nobili, “Dynamics of nematic liquid crystal disclinations: The role of the backflow”, *Phys. Rev. Lett.*, **95**, 097802 (2005).
- [19] P. Oswald and J. I. Mullol, “Backflow induced asymmetric collapse of disclination lines in liquid crystals”, *Phys. Rev. Lett.*, **95**, 027801 (2005).
- [20] I. Chuang, B. Yurke, and A. N. Pargellis, “Coarsening dynamics in uniaxial nematic liquid crystal”, *Phys. Rev. E* **47**, 3343 (1993).
- [21] G. F. Mazenko and M. Zannetti, “Instability, spinodal decomposition, and nucleation in a system with continuous symmetry”, *Phys. Rev. B* **32**, 4565 (1985).
- [22] H. Toyoki and K. Honda, “Ordering dynamics of a deeply quenched complex field”, *Prog. Theor. Phys.*, **78**, 237 (1987).
- [23] H. Toyoki, *Dynamics of ordering process in condensed matter*, edited by S. Komura and S. Furukawa (Plenum, New York), 1988.
- [24] H. Toyoki, “Pair annihilation of pointlike topological defects in the ordering process of quenched systems”, *Phys. Rev. A* **42**, 911 (1990).
- [25] H. Orihara and Y. Ishibashi, “Dynamics of disclination in twisted nematic quenched below the clearing point”, *J. Phys. Soc. Jpn.*, **55**, 2151 (1986).
- [26] I. Chuang, R. Durrer, N. Turok and B. Yurke, “Cosmology in the laboratory: Defect dynamics in liquid crystals”, *Science*, **251** 1336 (1991).
- [27] I. Chuang, N. Turok, and B. Yurke, “Late-Time coarsening dynamics in a nematic liquid crystal”, *Phys. Rev. Lett.*, **66**, 2472 (1991).
- [28] B. Yurke, A. N. Pargellis and N. Turok, “Coarsening dynamics of nematic liquid crystals”, *Mol. Cryst. Liq. Cryst.*, **222**, 195 (1992).
- [29] N. Mason, A. N. Pargellis and B. Yurke, “Scaling behavior of two time correlations in a twisted nematic liquid crystal”, *Phys. Rev. Lett.*, **70**, 190 (1993).

REFERENCES

- [30] O. D. Lavrentovich and S. S. Rozhkov, *Pis'ma Zh. Eksp. Teor. Fiz.* **47**, 210 (1988)[*JETP Lett.* **47**, 254 (1988)].
- [31] W. Wang, T. Shiwaku and T. Hashimoto, "Experimental study of dynamics of topological defects in nematic polymer liquid crystals", *J. Chem. Phys.*, **108**, 1618 (1998)
- [32] T. Shiwaku, A. Nakai, H. Hasegawa and T. Hashimoto, "Ordered structure of thermotropic liquid crystal polymers. 1. Characterization of liquid crystal domain texture", *Polym. Commun.*, **28**, 174 (1987); *Macromolecules* **23**, 1590 (1990).
- [33] D. K. Ding and E. L. Thomas, "Structures of point integer disclinations and their annihilation behavior in thermotropic liquid crystal polyesters", *Mol. Cryst. Liq. Cryst.*, **241**, 103 (1994).
- [34] A. Saupe, "Disclinations and properties of the director field in nematic and cholesteric liquid crystals", *Mol. Cryst. Liq. Cryst.*, **21**, 211 (1973).
- [35] R. B. Meyer, "Point disclinations at a nematic isotropic liquid interface", *Mol. Cryst. Liq. Cryst.*, **16**, 355 (1972).
- [36] I. Dierking, O. Marshall, J. Wright and N. Bullied, "Annihilation dynamics of umbilical defects in nematic liquid crystals under applied electric fields", *Phys. Rev. E* **71**, 061709 (2005).
- [37] S. Dhara, J. K. Kim, S. M. Jeong, R. Kogo, F. Araoka, K. Ishikawa and H. Takezoe, "Anchoring transitions of transversely polar liquid crystal molecules on perfluoropolymer surfaces", *Phys. Rev. E* **79**, 060701 (2009).
- [38] T. Arun Kumar, P. Sathyanarayana, V. S. S. Sastry, H. Takezoe, N. V. Madhusudana and S. Dhara, "Temperature and electric field induced inverse Fredericksz transition in a nematogen with weak surface anchoring", *Phys. Rev. E*, **82**, 011701 (2010).
- [39] S. Dhara, T. A. Kumar, K. Ishikawa and H. Takezoe, "Thermotropic uniaxial nematic liquid crystal with $\pm 1/2$ strength disclinations: defect-

REFERENCES

- antidefect production and correlation”, *J. Phys. Condens. Matter*, **21**, 505103 (2009).
- [40] S. Dhara and N. V. Madhusudana, “Physical characterisation of 4’-butyl-4-heptyl- bicyclohexyl-4-carbonitrile”, *Phase Transition*, **81**, 561 (2008).
- [41] M. Kleman and O. D. Lavrentovich, “Topological point defects in nematic liquid crystals”, *Phil. Mag.*, **86**, 4117 (2006).

5

Anchoring transition in a nematic liquid crystal doped with chiral agents

5.1 Introduction

In the previous chapter we have discussed the effect of electric field on the defects in CCN-47 in CYTOP treated cells and found some new defect structure. With the intention to extend the investigation of anchoring transition in cholesteric liquid crystals (CLCs) on CYTOP treated substrate, we have prepared several cholesteric liquid crystals by adding several chiral dopants at various concentrations with the same nematic liquid crystal (CCN-47) studied in the previous chapters. The alignment and anchoring transition of cholesteric liquid crystals in CYTOP treated cells is the main concern of this chapter.

Cholesteric liquid crystals exhibit various types of orientations with appropriate boundary conditions namely the planar (Grandjean), focal conic, fingerprint and amorphous cholesteric texture. Some typical director orientations in cholesteric liquid crystals with planar and homeotropic boundary conditions are schematically shown in Figure 5.1. In case of planar texture, the liquid crystal molecules are parallel to the surface of the cell and the helix is perpendicular to the surface as shown schematically in Figure 5.1(a). The

Anchoring transition in a nematic liquid crystal doped with chiral agents

planar texture selectively reflects the light when the pitch is comparable to the wavelength of incident light. In focal conic texture, the helical axis is randomly oriented as schematically shown in Figure 5.1(b). In the focal conic state the reflection depends on the distribution of the helical axis orientation and the internal structure of the multidomain texture. In case of homeotropic cell, the helix axis lies parallel to the substrate as shown schematically in Figure 5.1(c) and no reflection occurs. Cholesteric liquid crystals also exhibit amorphous orientation under strong homeotropic boundary conditions as shown in Figure 5.1(d). Some typical textures of cholesteric liquid crystal under planar and homeotropic boundary conditions are shown in Figure 5.2 and 5.3 respectively.

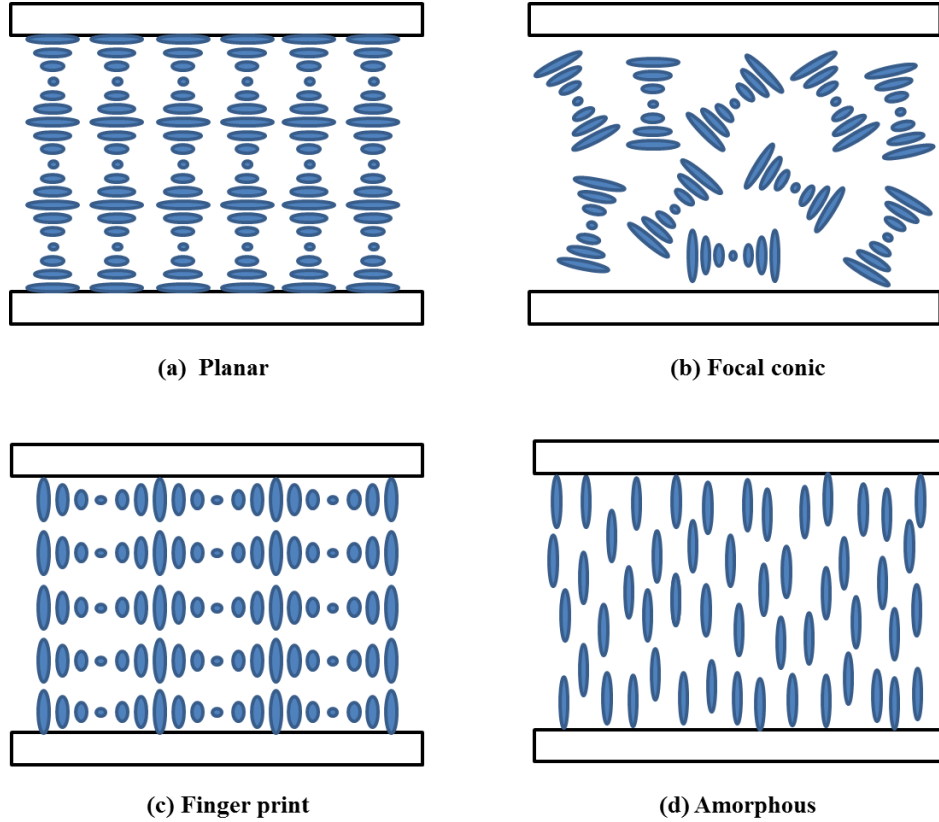


Figure 5.1: Schematic diagram showing various orientations of CLCs: (a)&(b) with planar boundary conditions and (c)&(d) with homeotropic boundary conditions [1].

5.1 Introduction

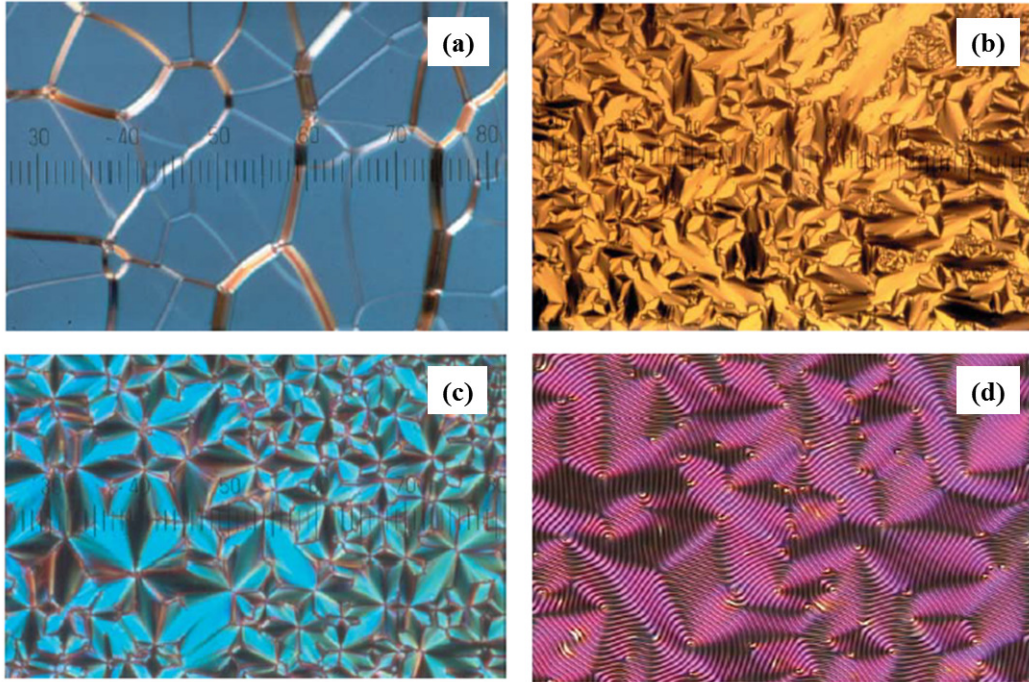


Figure 5.2: Textures of cholesteric phase under planar anchoring conditions: (a) oily streaks texture with a pitch of $P = 2\mu m$, such that the colour observed is not due to selective reflection, (b) fan-like texture of a short pitch cholesteric phase (c) fan-shaped focal conic texture of a short pitch cholesteric phase (d) cholesteric polygonal (fingerprint) texture with a relatively long pitch, such that the helical N^* superstructure is resolved by polarizing microscopy. (adopted from reference [5]).

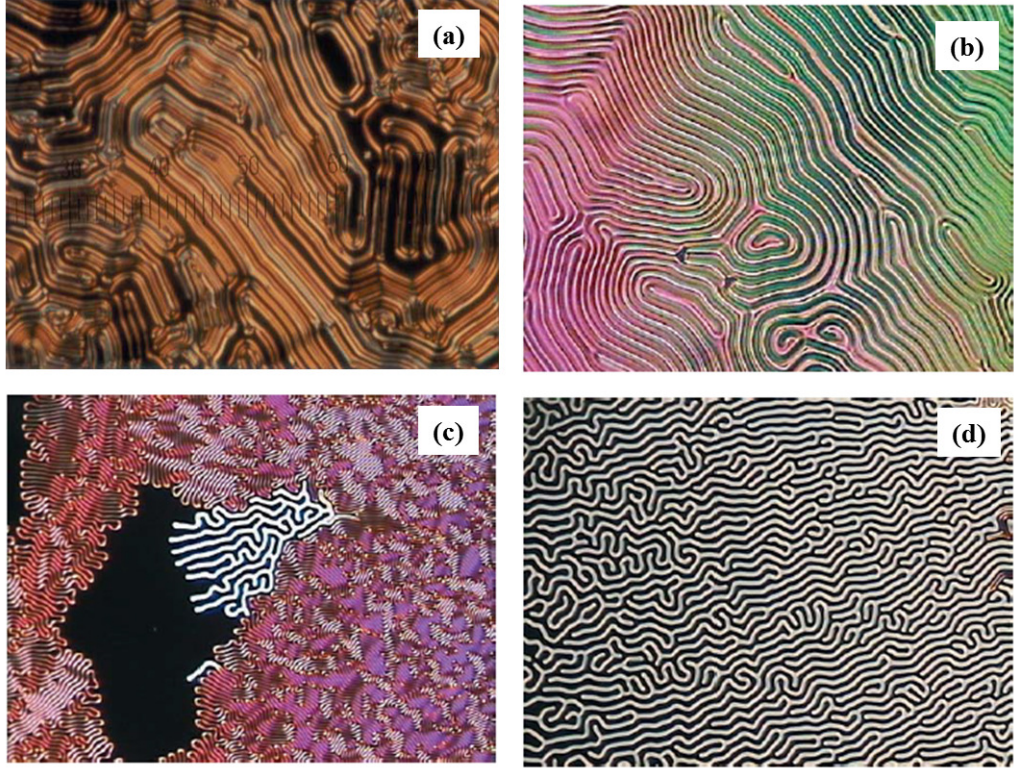
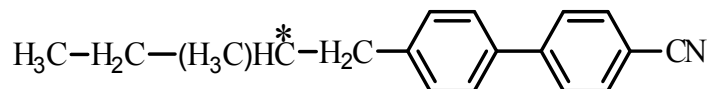


Figure 5.3: Textures of cholesteric phase under homeotropic anchoring conditions: (a) fingerprint texture owing to the identity period $L = P/2$ of the cholesteric phase, the pitch can be determined as twice the distance between two dark lines, (b) fingerprint texture with pitch P approaching the cell gap d (c) coexistence of a cholesteric fingerprint texture with so-called cholesteric fingers (bright lines in the center) and a pseudo-isotropic region with a homeotropic nematic director configuration (black) (d) sample with a diverging cholesteric pitch exhibiting so called cholesteric fingers. In the strongly distorted director configuration, the dark areas represent a pseudo-isotropic, homeotropically aligned nematic (adopted from reference [5]).

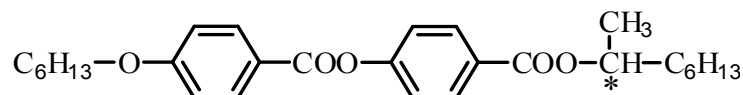
5.2 Experimental

We have used CYTOP treated cells of thickness $\simeq 5\mu m$ to study the anchoring transition in CCN-47 doped with chiral agents. On the other hand polyimide coated wedge cells were used to measure the pitch of the same sample. We have used several chiral agents such as CB15, S811 and d-2. The first two chiral dopants are obtained from Merck Ltd., Japan and d-2 is an imine-based chiral dopant [2]. The chemical name of CB 15 is 4-cyano-4'-(2-methylbutyl)-biphenylene. It has the following phase transitions: Cr 4°C N* 54°C I, and exhibits right handed helix [3]. The chemical name of S811 is 4-[(1-methylheptyl)oxy]carbonylphenyl-4-(hexyloxy)benzoate. It has following phase transitions: Cr 47.8°C I, and exhibits left handed helix [4]. The chemical structure of all these chiral dopants are shown in Figure 5.4. We have prepared several mixtures by adding chiral agents in various concentrations with CCN-47. The chiral dopants and CCN-47 were dissolved in chloroform and the bottle was kept on vortex mixture to mix the compounds thoroughly. Then it was kept on a hotplate at temperature 60°C for 3 hours to evaporate chloroform. The texture observation was made using the polarizing optical microscope (POM). The temperature of the sample is controlled by a Mettler hotstage (FP82HT) with an accuracy of $\simeq 0.1^{\circ}\text{C}$.

1) Chiral dopant CB 15



2) Chiral dopant S 811



3) Chiral dopant d-2

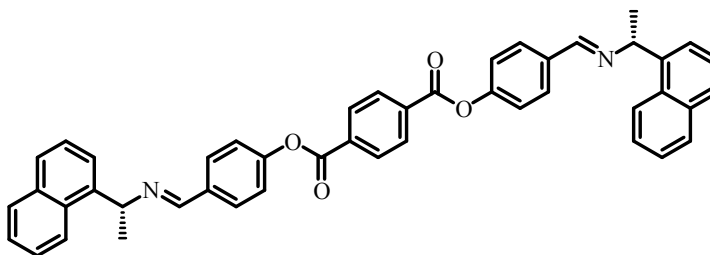


Figure 5.4: Chemical structures of chiral agents CB 15, S811 and d-2.

5.3 Results and Discussion

5.3.1 CLCs doped with CB15

We first prepared a cholesteric liquid crystal by adding 5wt% of CB 15 to the nematic liquid crystal CCN-47. Then the sample is filled into the CYTOP coated unrubbed cell of thickness $\simeq 5\mu\text{m}$. When the sample was cooled from the isotropic to cholesteric phase at the rate of 1°C per minute, the fan-shaped texture appears at 51.1°C as shown in Figure 5.5(a). When the

5.3 Results and Discussion

temperature reaches to 48.0°C , the fan-shaped texture changes to finger print texture as shown in Figure 5.5(b-d). We have also observed the sample on heating and found that the texture changes from finger print to fan-shaped as shown in Figure 5.5(e&f). It indicates that the pitch of the cholesteric is increasing as the temperature is reduced as expected. Interestingly we did not observe any anchoring transition with this concentration. This suggests that the interfacial forces that are responsible for anchoring transition are affected by the addition of large chiral dopant. In other words, helix forming ability is strong enough compared with the interfacial forces. To reduce the helix forming ability, we have reduced the concentration of CB15 from 5wt% to 3wt%. The textures observed with 3wt% are shown in Figure 5.6. When the temperature is reduced to 55.3°C from the isotropic phase, only planar state exists with several cholesteric defects in it as shown in Figure 5.6(a). As the temperature decreases further to 46.7°C , finger print texture is disappearing and some regions with reduced birefringence are seen as shown in Figure 5.6(b), suggesting tilting of director. This transition proceeds till it reaches to 45.7°C . On further cooling to 39.7°C , the texture changes and some small dark regions are formed as shown in Figure 5.6(c&d). This is more prominent when the sample is cooled down to 28.7°C as shown in Figure 5.6(e). Almost complete homeotropic state with some thin bright lines are observed when the temperature is reduced to 25°C as shown in Figure 5.6(f).

On heating, the cholesteric finger appears at 27.3°C as shown in Figure 5.7(a) and the texture remains the same until the temperature reaches to 51.3°C as shown in Figure 5.7(b-d). At 51.4°C , some bright domains are also seen along with the finger print texture as shown in Figure 5.7(e&f). Gradually the finger print texture disappears as the temperature proceeds towards isotropic as shown in Figure 5.7(g&h). The situation is more clearer in the sample with 1wt% of CB15. With decreasing temperature, finger print and cholesteric finger textures cannot be observed. Instead, the anchoring transition could be more clearly observed. Thus, with decreasing the weight fraction of chiral dopant CB15, the anchoring transition becomes prominent, as expected.

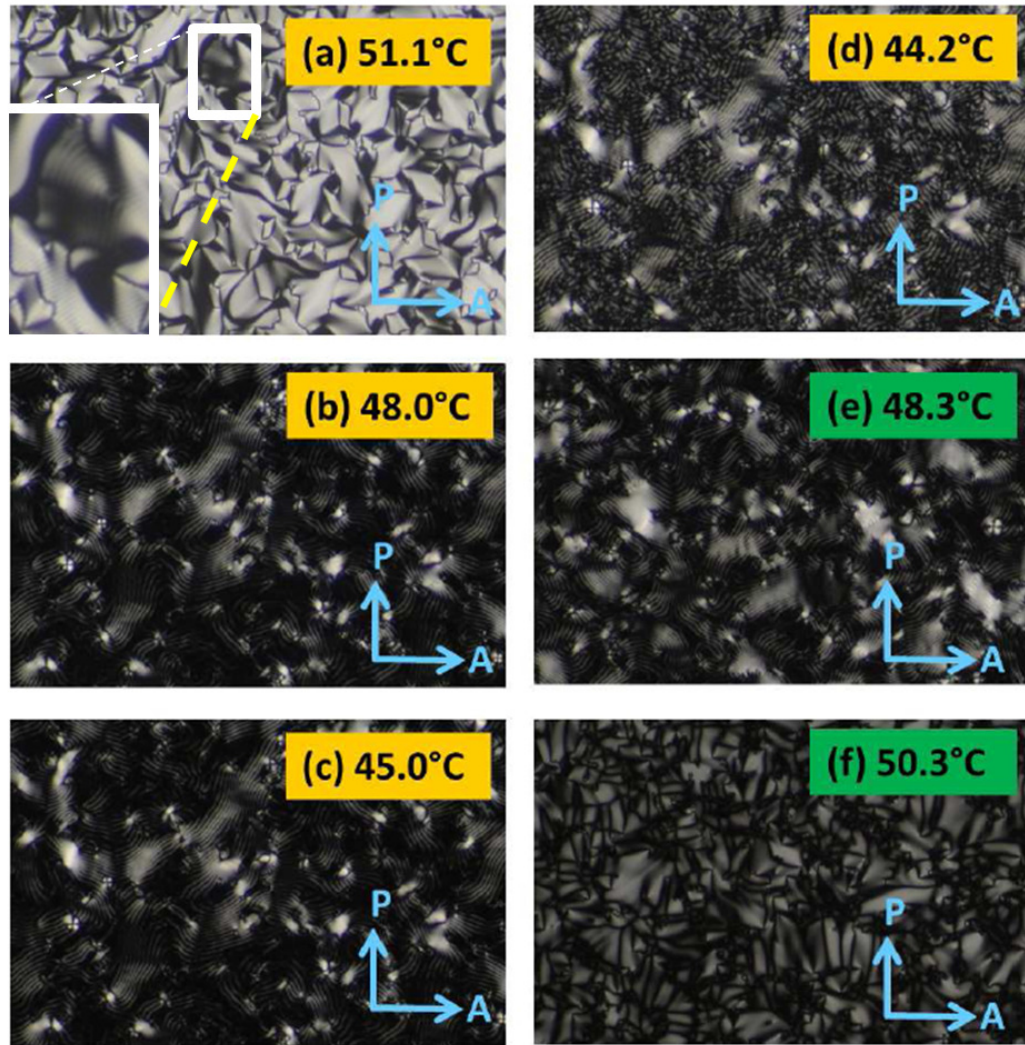


Figure 5.5: The evolution of textures in CCN-47 doped with 5wt% of CB15: (a) fan-shaped texture, (b)-(d) fan-shaped to finger print on cooling, and (e) and (f) finger print to fan-shaped on heating. Even in (a) fine fringes are seen (inset).

5.3 Results and Discussion

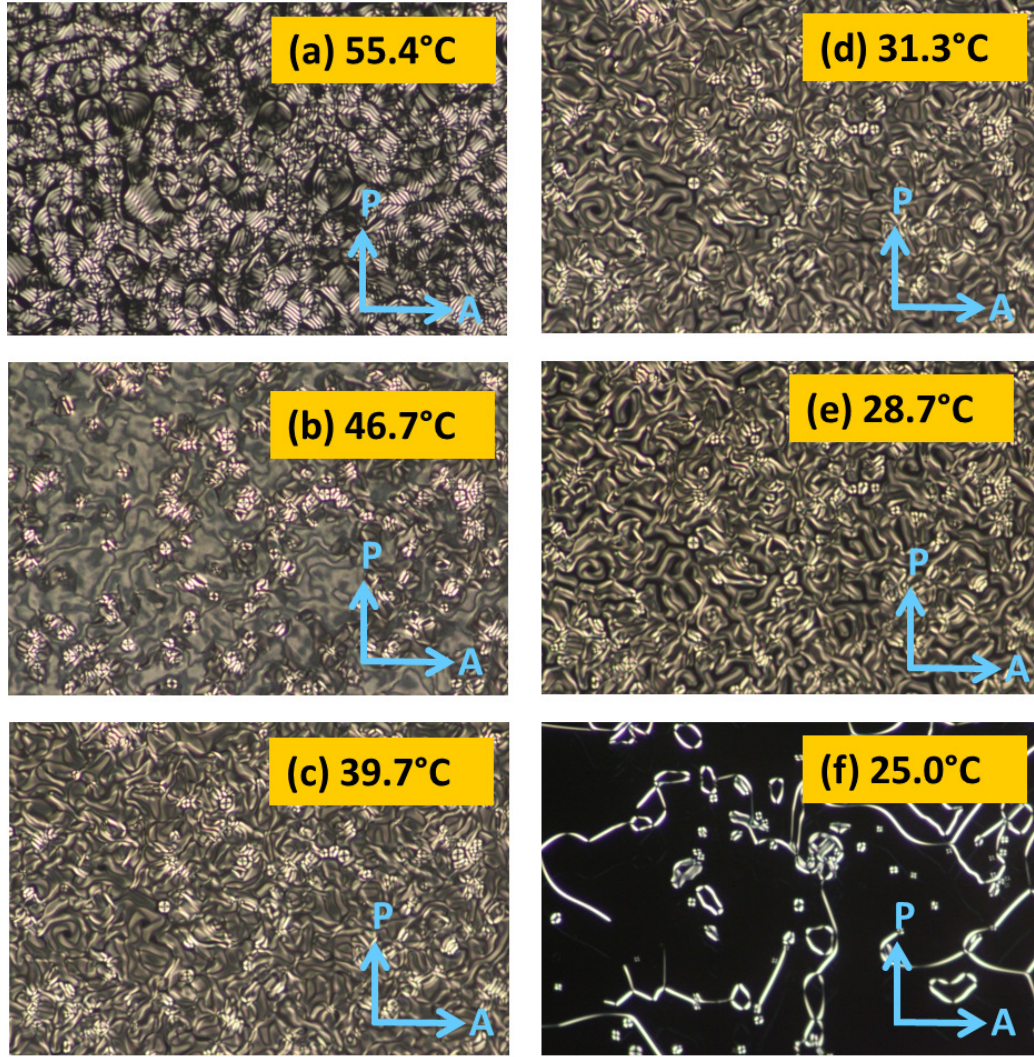


Figure 5.6: Photomicrographs of CCN-47 doped with 3wt% of CB15 on cooling: (a) planar state, (b) planar to tilting transition, (c) & (d) finger print texture with some homeotropic regions, (e) texture with more homeotropic regions, (f) homeotropic state with a few thin bright lines.

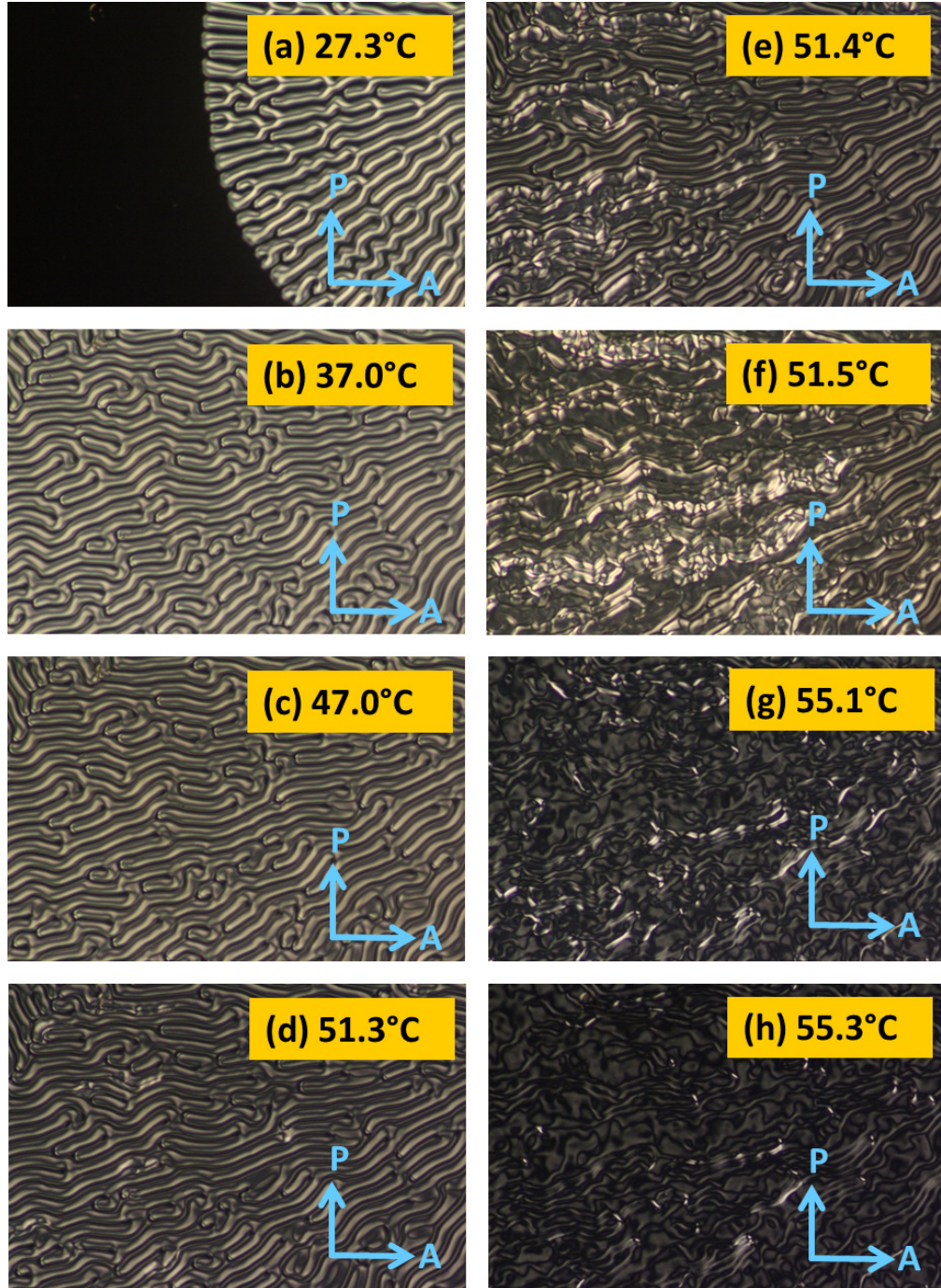


Figure 5.7: Photomicrographs of CCN-47 doped with 3wt% of CB15 on heating: (a) transition from homeotropic to finger print, (b)-(d) finger print texture, (e)&(f) finger print to tilted state, and (g)&(h) tilted state with reduced brightness.

5.3 Results and Discussion

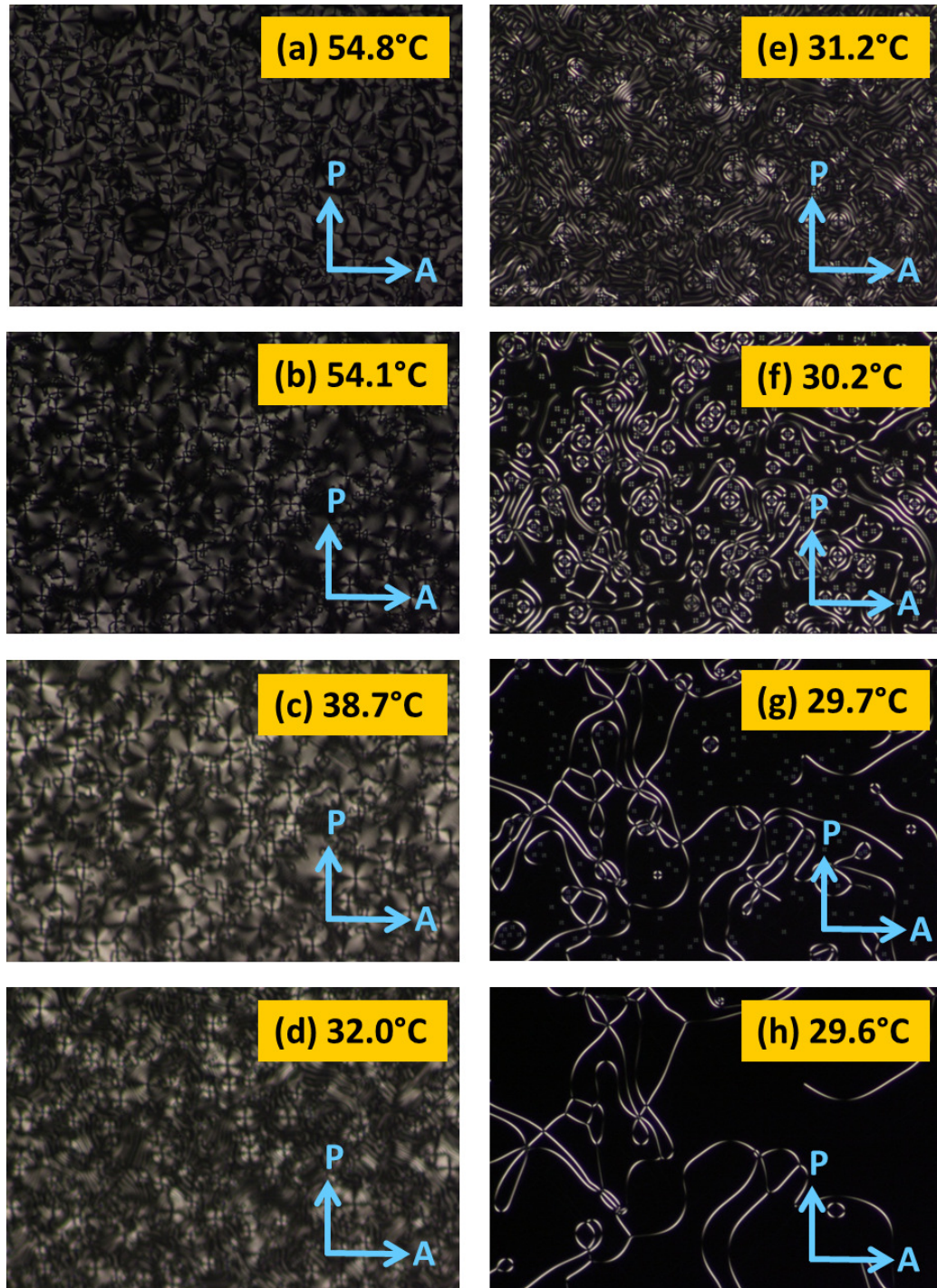


Figure 5.8: Photomicrographs of CCN-47 doped with 5wt% of S811 on cooling: (a)-(c) Textures of fan like shape, (d)&(e) transition from fan-like shape to finger print, and (f)-(h) finger print to homeotropic state.

Anchoring transition in a nematic liquid crystal doped with chiral agents

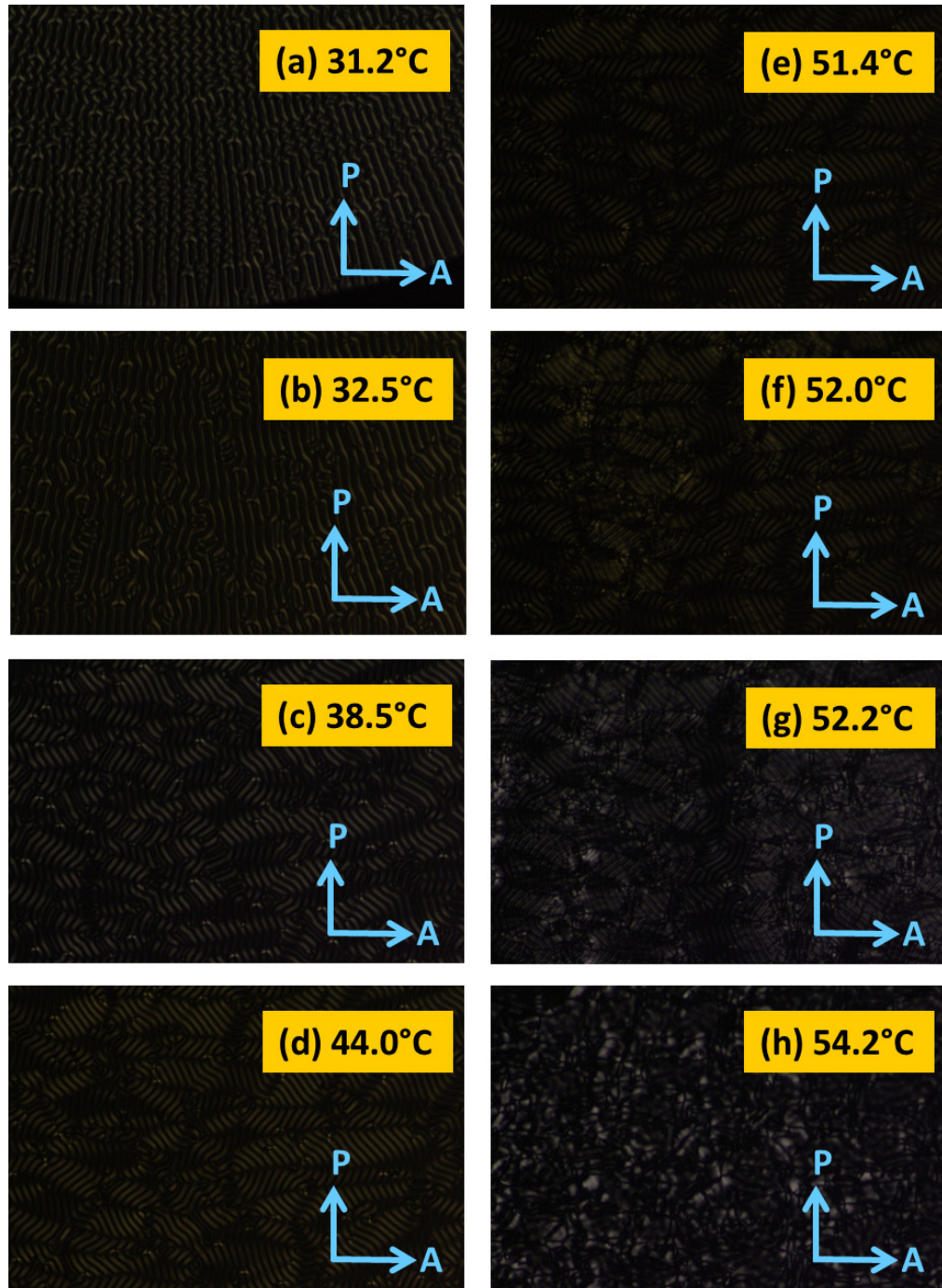


Figure 5.9: Photomicrographs of CCN-47 doped with 5wt% of S811 on heating: (a) the transition from homeotropic to finger print texture, (b)-(e) finger print texture, (f) transition from finger print to tilted state, and (g&h) fan-like shape texture.

5.3 Results and Discussion

5.3.2 CLCs doped with S811

Further we studied a cholesteric liquid crystal prepared by mixing the chiral agent S811 with CCN-47. In this case, we first added 5wt% of S811 to CCN-47 and then filled it in CYTOP treated unrubbed cell. When the sample was cooled from isotropic to cholesteric phase, we found fan-like shape texture at 54.8°C as shown in the Figure 5.8(a-c). As the sample is cooled further, the fan-like shape texture slowly changes to finger print texture as shown in Figure 5.8(d&e). When the sample temperature reaches to 30.2°C, the finger print texture is transformed to mostly homeotropic texture with some bright thin lines as shown in the Figure 5.8(f-h). While on heating, the finger print texture appears at 31.2°C as shown in Figure 5.9(a). The finger print texture remains same until the temperature reaches to 51.4°C as shown in the Figure 5.9(b-e). At 52°C, we noticed continuous change in texture suggesting an anchoring transition from finger print texture to fan like shape texture is shown in Figure 5.9(f). The fan like shape textures are shown in the Figure 5.9(g&h).

We further studied mixture of CCN-47 with 1wt% of S811. Mostly the finger print texture was observed during the isotropic to cholesteric phase transition as shown in Figure 5.10(a-c). As the temperature decreases finger print texture is transformed to homeotropic texture is shown in the Figure 5.10(d&f). When the sample temperature is reduced further, the finger print texture is almost disappeared and becomes completely homeotropic as shown in the Figure 5.10(g-h). The variation is more clearly seen when the same sample (1wt%) was filled in CYTOP treated rubbed cell and texture observation was made under polarizing microscope. As the temperature decreases from isotropic to cholesteric, the overall brightness increases as the temperature decreases as shown in Figure 5.11(a&b). When the temperature reaches to 32.0°C, the anchoring transition from planar to homeotropic state occurs along the rubbing direction as shown in the Figure 5.11(c). As the sample temperature decreases further the homeotropic regions grow as shown in the Figure 5.11(d&e). The sample becomes completely homeotropic at

Anchoring transition in a nematic liquid crystal doped with chiral agents

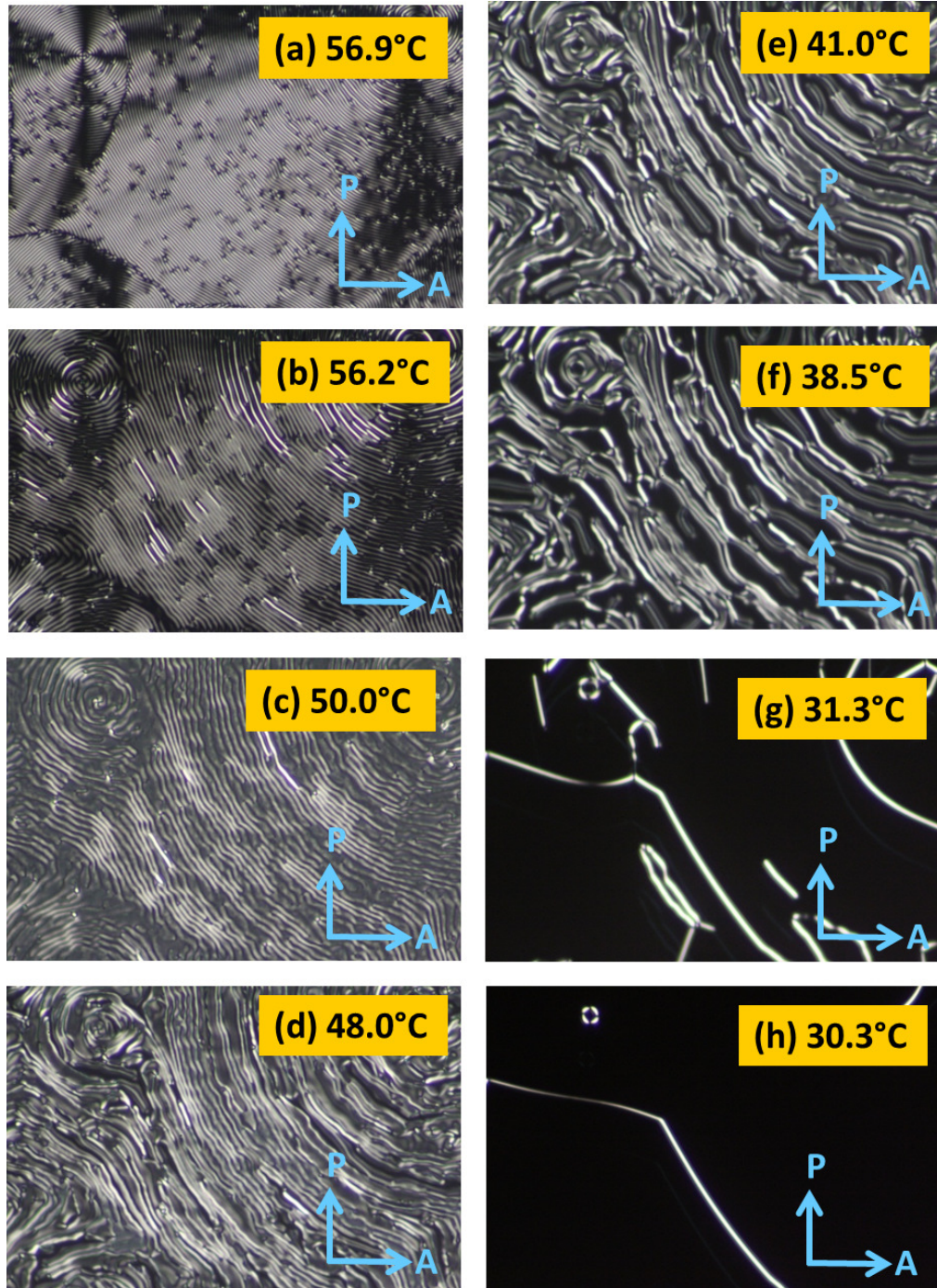


Figure 5.10: Photomicrographs of CCN-47 doped with 1wt% of S811 on cooling:(a)-(c) fan shape texture, (d)–(f) fan shape texture slowly changes to finger print texture, (g)&(h) transition from finger print to homeotropic state.

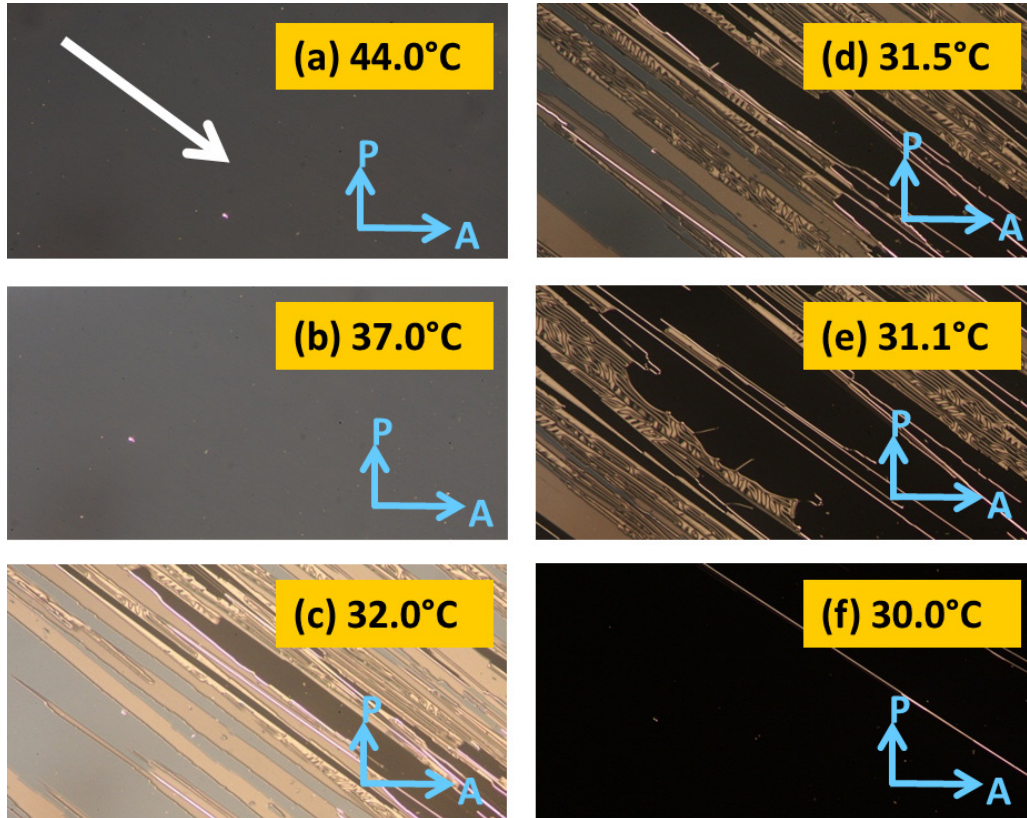


Figure 5.11: Photomicrographs showing alignment of CCN-47 doped with 1wt% of S811 in a CYTOP treated rubbed cell on cooling: (a) tilted state, (b) tilted state with increased brightness, (c) anchoring transition from planar to homeotropic state, (d&e) anchoring transition, and (f) homeotropic state.

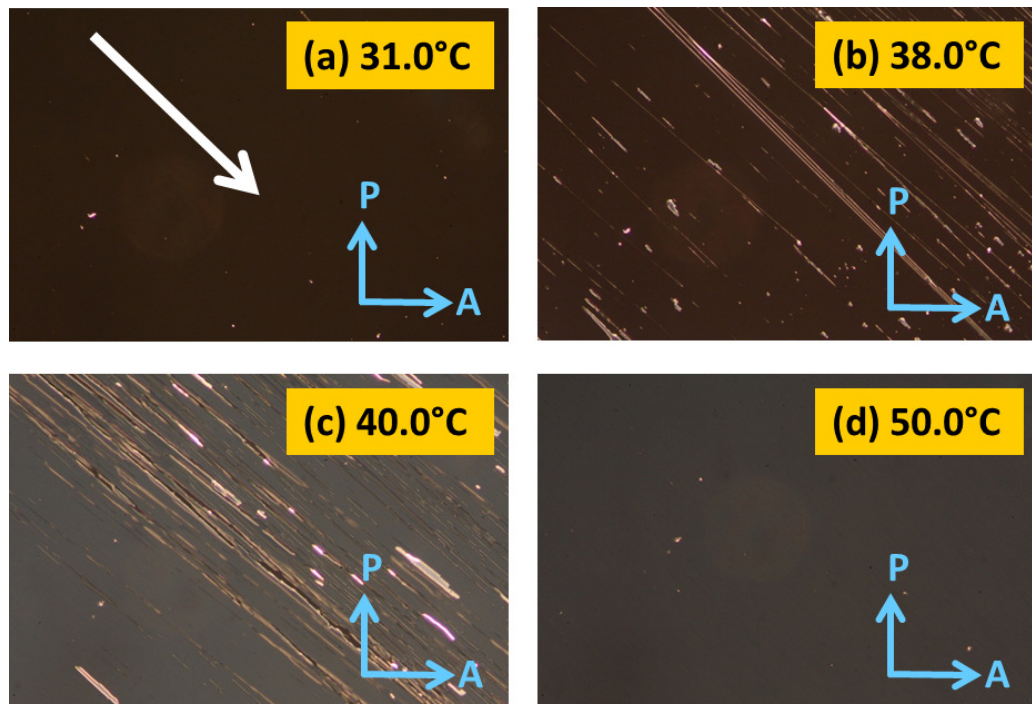


Figure 5.12: Photomicrographs showing alignment of CCN-47 doped with 1wt% of S811 in a CYTOP treated rubbed cell on heating: (a) homeotropic state, (b)&(c) anchoring transition from homeotropic to planar state, and (d) tilted state with reduced brightness.

5.3 Results and Discussion

$\simeq 30^\circ\text{C}$ as shown in Figure 5.11(f). On the other hand, the sample exhibits homeotropic state on heating till the temperature reaches to 37.8°C as shown in Figure 5.12(a). When the temperature reaches to 38°C , it exhibits anchoring transition from homeotropic to planar state as shown in Figure 5.12(b-d).

5.3.3 CLCs doped with d-2

The two chiral dopants CB15 and S811 have similar helical twisting power (HTP) [6, 7]. In order to study the effect of dopant with large twisting power, we have chosen d-2 which is known to have high helical twisting power ($\text{HTP} = 140\mu\text{m}^{-1}$ in the host 6OCB). We first prepared a cholesteric liquid crystal by adding 5wt% of d-2 with CCN-47 and it is filled in a CYTOP treated rubbed cell. When the temperature decreases from isotropic, we found isotropic to cholesteric phase transition at 58.7°C as shown in Figure 5.13(a). As the temperature decreases, the selective reflection occurs with Grandjean steps as shown in Figure 5.13(b). When the temperature decreases further, the selective reflections shifts from blue to cyan and the width of Grandjean steps also increases as shown in Figure 5.13(c-f). With this concentration we did not see anchoring transition in the sample. Then we reduced the concentration of d-2 from 5wt% to 0.7wt%. We have found that it exhibits only planar texture with no anchoring transition. Further we reduced concentration to 0.5wt% and made microscope observations as shown in Figure 5.14. As the temperature decreases from isotropic phase, we observed focal conic texture with finger prints at 58.5°C as shown in Figure 5.14(a). While cooling we observed a discontinuous anchoring transition from tilted to homeotropic state at $\simeq 47.2^\circ\text{C}$ as shown in Figure 5.14(b). While heating it exhibits anchoring transition from homeotropic to tilted state at temperature 53.0°C as shown in Figure 5.14(c-d).

We also measured the pitch of the mixture with concentrations of 7.5wt%, 5wt% and 0.7wt% of d-2. We have used polyimide treated wedge cells with wedge angle $\alpha = 1.5^\circ$. The schematic orientation of helix in the wedge cell is shown in Figure 5.15. A planar texture with Grandjean Cano steps for

Anchoring transition in a nematic liquid crystal doped with chiral agents

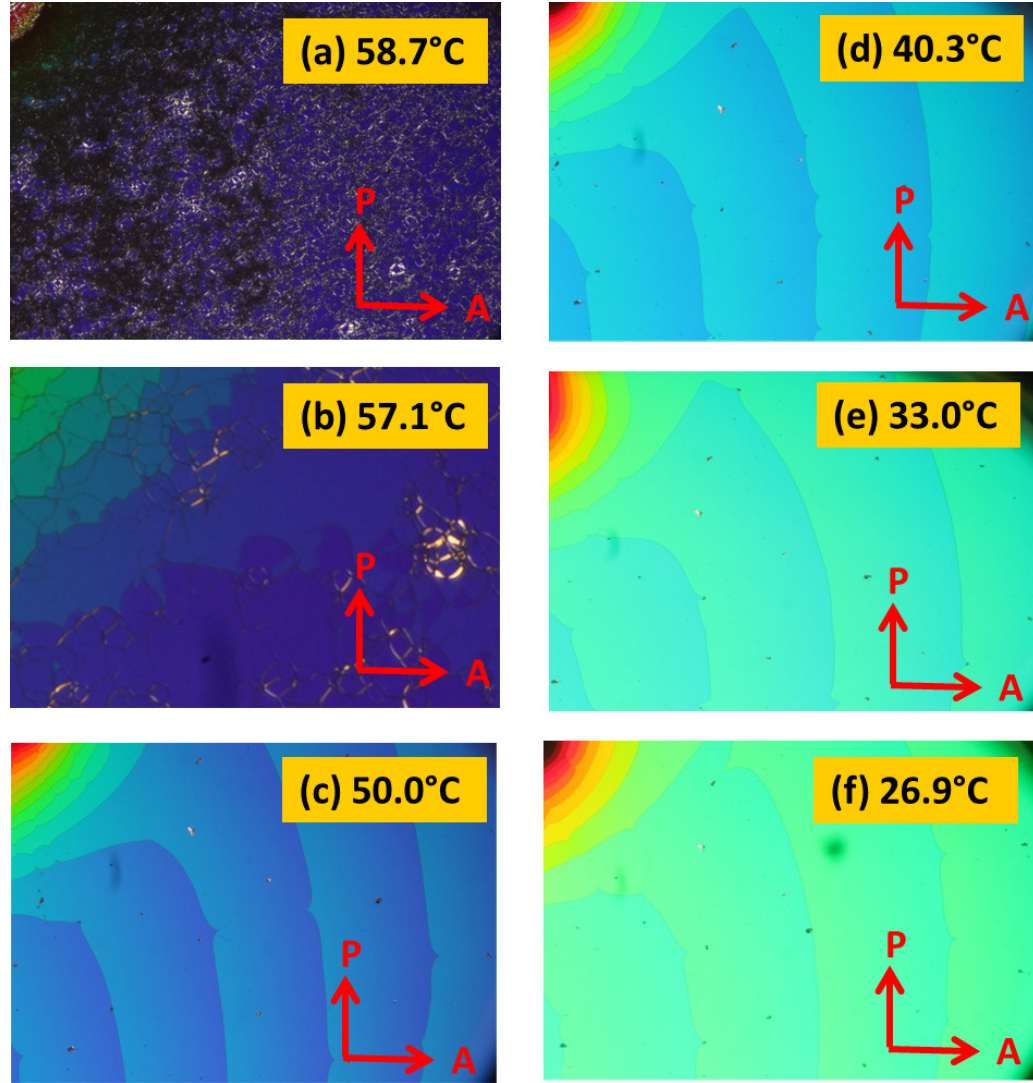


Figure 5.13: Textures with selective reflection on cooling in CYTOP treated rubbed cell with 5wt% of d-2: (a) isotropic to cholesteric phase transition, (b) selective reflection with Grandjean steps, (c) selective reflection of blue colour, (d) blue colour is changing to cyan, and (e)&(f) selective reflections in cyan colour.

5wt% of d-2 is shown in Figure 5.16. In order to measure pitch, we have taken several wedge lines and measured the pitch below $\simeq 10^\circ\text{C}$ from the isotropic-cholesteric phase transition temperature. The pitch of the cholesteric

5.3 Results and Discussion

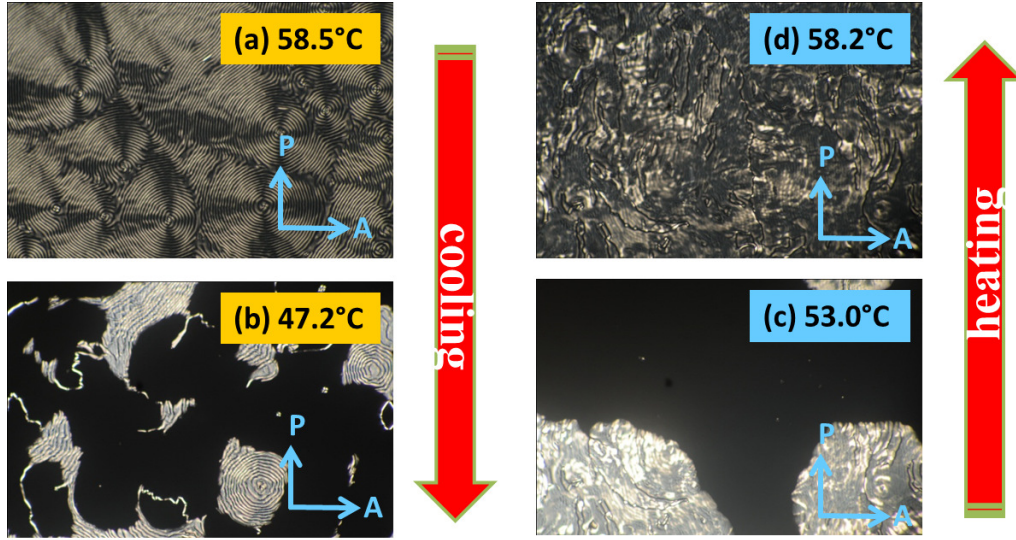


Figure 5.14: Photomicrographs of CLCs made from 0.5wt% of d-2: (a) focal conic texture (b) a discontinuous anchoring transition from tilted to homeotropic occurs at 47.2°C on cooling, (c) anchoring transition from homeotropic to planar occurs at 53.0°C, and (d) tilted state.

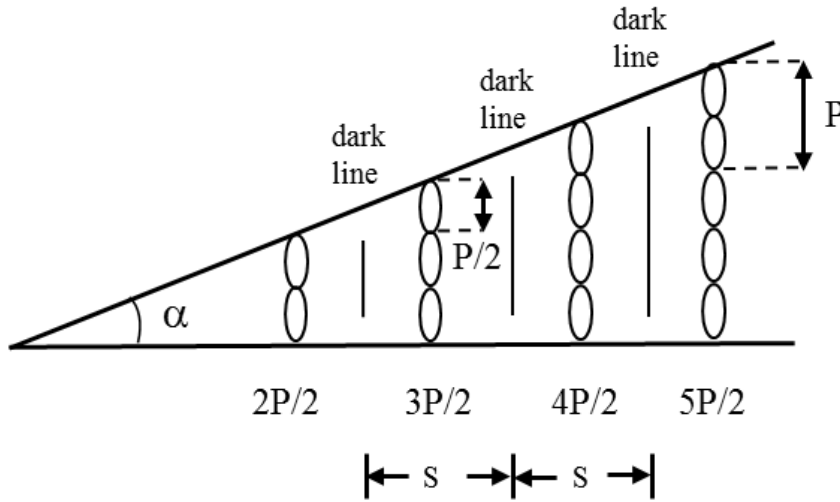


Figure 5.15: Schematic illustration of the wedge cell for the determination of the pitch. Where S is the distance between two Grandjean lines and P is the pitch of the cholesteric.

Anchoring transition in a nematic liquid crystal doped with chiral agents

liquid crystal is measured using the following equation.

$$P = 2S \tan \alpha$$

where S is the distance between the wedge lines. We studied the temperat-

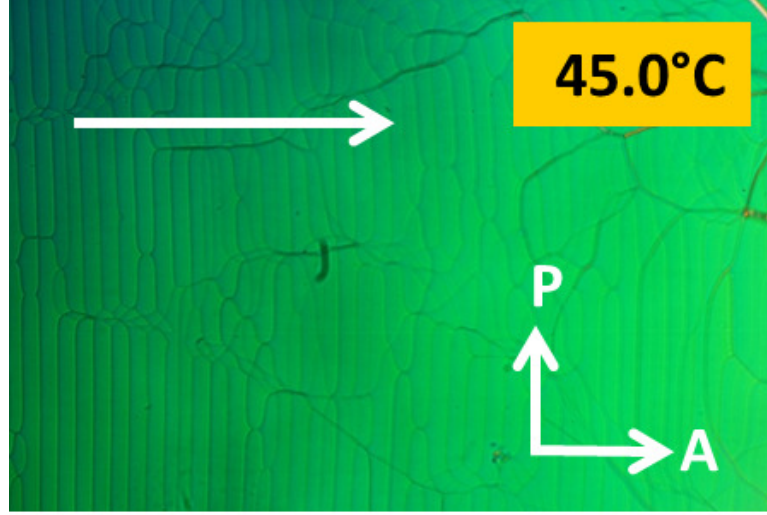


Figure 5.16: Photomicrographs of Grandjean steps observed in wedge cell with 5wt% concentration of d-2 in CCN-47. An arrow in the picture denotes the rubbing direction.

ure dependent of pitch and the variation of pitch as a function of temperature is shown in Figure 5.17. It is observed that very close to isotropic to cholesteric phase transition the pitch is $\simeq 0.54\mu m$ and it increases to 0.59 as the temperature decreases towards the room temperature ($30^\circ C$) as shown in Figure 5.18. The similar kind of measurement was also made on 0.7wt% of d-2. The Grandjean steps (Figure 5.18) observed and temperature variation of pitch is shown in Figure 5.19. In this case the pitch is large and very close to isotropic to cholesteric phase transition it is $\simeq 4.4\mu m$ and it increases to 5.2 as the temperature decreases towards the room temperature ($30^\circ C$) as shown in Figure 5.19.

We also estimated the HTP of d-2. The HTP of a chiral dopant is defined as

$$\beta = (P_{cr})^{-1}$$

5.3 Results and Discussion

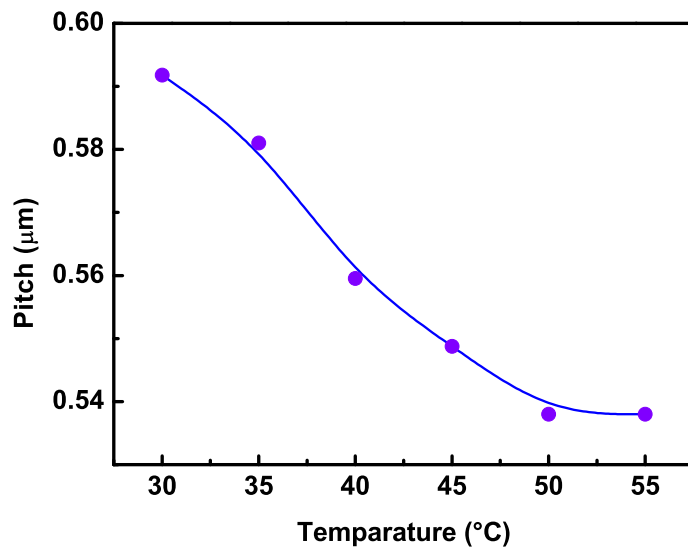


Figure 5.17: Variation of pitch (P) as a function of temperature for the concentration 5wt% of d-2.

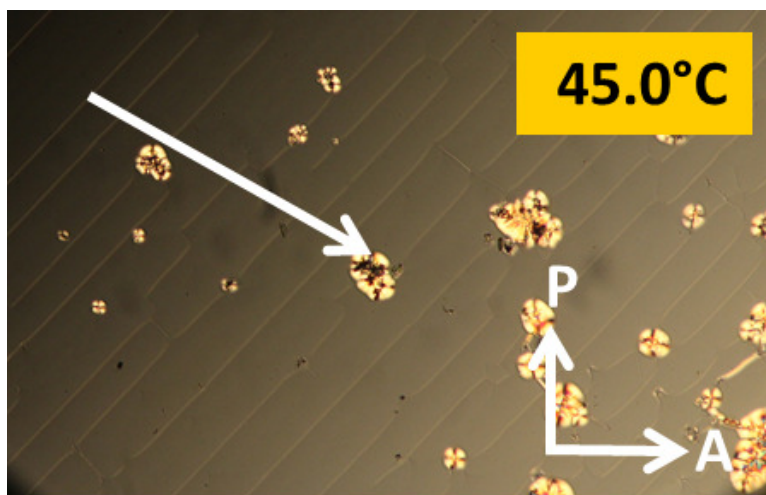


Figure 5.18: Photomicrographs of Grandjean steps observed in wedge cell with 0.7wt% concentration of d-2 in CCN-47. An arrow in the picture denotes the rubbing direction.

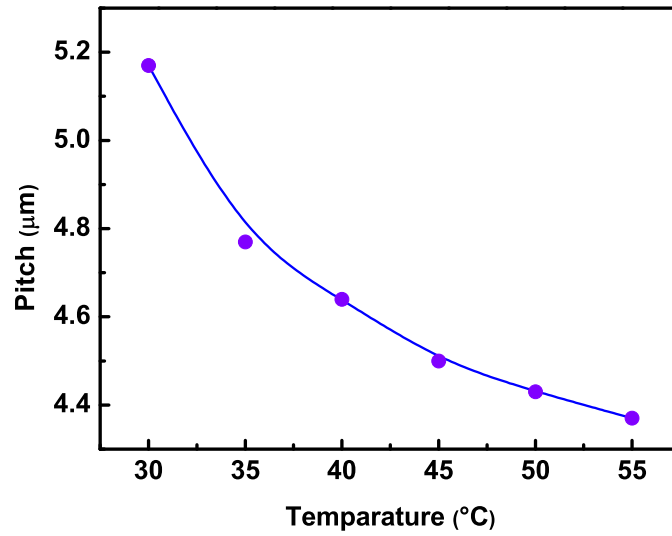


Figure 5.19: Variation of pitch (P) as a function of temperature for the concentration 0.7wt% of d-2.

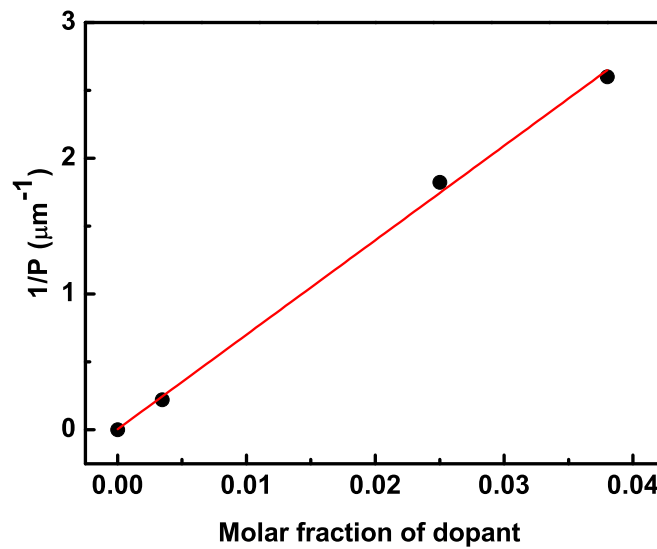


Figure 5.20: Variation of inverse of the pitch (P) as a function of molar fraction of d-2.

5.4 Conclusions

Name of the liquid crystal	Name of the chiral dopant	wt% of chiral dopant	N-I transition temperature (°C)	Anchoring transition on cooling (°C)	Anchoring Transition on heating (°C)
CCN-47	-	0	57.9	47.8	54.0
-	CB 15	5	51.4	no A.T	no A.T
-	-	3	55.4	46.7	51.4
-	S811	5	55.1	32	-*
-	-	1	56.9	48.2	52.8
-	d-2	5	58.9	no A.T	no A.T
-	-	0.7	58.5	no A.T	no A.T
-	-	0.5	58.5	47.3	53.0
-	-	0.2	58.5	46.8	52.7

Table 5.1: Summary of isotropic to nematic and anchoring transition temperatures of chiral dopant added CCN 47. Where no A.T denotes no anchoring transition. *For S811(5wt%) no clear anchoring transition is observed on heating.

where P is the pitch of the chiral nematic phase, c is the molar fraction of the dopant, and r is the enantiometric excess of the dopant. The variation of the inverse of the pitch as a function of molar fraction of d-2 is plotted in Figure 5.20. It is found $\beta \approx 70\mu m^{-1}$, which is almost half compared to the value in the host liquid crystal 6OCB [2]. Finally we present the summary of the study on various chiral dopants in Table 5.1.

5.4 Conclusions

We have observed anchoring transition in CLCs prepared by several chiral agents such as CB 15, S 811 and d-2. Very complicated anchoring transitions were observed mainly depending on HTP. When HTP was very large, a helical structure with the axis perpendicular to surfaces appeared with clear selective reflection and Grandjean lines, and no anchoring transition was observed. In smaller HTP samples, on cooling, fan-shaped texture with fine fringes was

transformed to finger print texture and further to a homeotropic texture. On heating, cholesteric finger emerged from a homeotropic texture, and then the anchoring transition to finger print and to fan-shape-like texture occurs. Such complicated anchoring transition originates from the competition between surface interaction and helix forming power.

References

- [1] Heinz-Siegfried Kitzerow and Christian Bahr, *Chirality in liquid crystals*, Springer, Ed.1, 2000.
- [2] K. Fukuda, H. Suzuki, J. Ni, M. Tokita, and J. Watanabe, "Relationship between chemical structure and helical twisting power in optically active imine dopants derived from (R)-(+)-1-(1-Naphthyl)ethylamine", *Jpn. J. Appl. Phys.*, **46**, 5208 (2007).
- [3] H. Yang, H. Kikuchi and T. Kajiyama, "Thermal switching characteristics based on smecticA \leftrightarrow chiral nematic phase transitions of (liquid crystals/chiral dopant) composites, with and without side chain type liquid crystalline polymer", *Liq. Cryst.*, **29**, 1141 (2002).
- [4] T. H. Lin, Y. J. Chen, C. H. Wu, Y. G. Fuha, J. H. Liu and P. C. Yang, "Cholesteric liquid crystal laser with wide tuning capability", *Appl. Phys. Lett.*, **86**, 161120 (2005).
- [5] I. Dierking, *Textures of liquid crystals*, WILEY-VCH Verlag GmbH & Co. KGaA, 2003.
- [6] E. L. Popova, V. I. Rozenberg, Z. A. Starikova, S. K. Baumann, H. S. Kitzerow, and H. Hopf, "Thermotropic liquid crystals from planar chiral compounds: Optically active mesogenic [2.2] paracyclophane derivatives", *Angew. Chem. Int. Ed.*, **41**, 18 (2002).
- [7] C. R. Lee, S. H. Lin, H. S. Ku, J.H. Liu, P. C. Yang, C. Y. Huang, H. C. Yeh, and T. D. Ji, "Optically band-tunable color cone lasing emission

REFERENCES

in a dye-doped cholesteric liquid crystal with a photoisomerizable chiral dopant”, *Appl. Phys. Lett.*, **96**, 111105 (2010).

6

Perfluoropolymer as planar alignment layer for liquid crystal mixtures

6.1 Introduction

In the previous chapter we have discussed the anchoring transition in cholesteric liquid crystals which are made from the nematic liquid crystal (CCN-47) by adding several chiral agents. In this chapter we will discuss the alignment properties of a room temperature nematic liquid crystal mixture in CYTOP treated cells.

The alignment of liquid crystals (LCs) on the treated surfaces of solid substrates is of great importance for the basic understanding of the interfacial phenomena as well as technological applications [1]. The bulk LC and the interfacial properties strongly influence the electro-optical properties of liquid crystal displays (LCDs) [2, 3]. It is well known that weak anchoring of the LC director at the interface with alignment layer can in principle reduce the operating voltages and can improve the steepness of the electro-optic response of LCDs [4]. For the performance of multistable optical switching, weak anchoring is also desirable. Fast response time less than several hundreds of microseconds are desired for high performance LCDs. The main objective of this chapter is to study the alignment behaviour of a room temperature

nematic liquid crystal mixture (ZLI-2293) on perfluoropolymer (CYTOP). We found CYTOP provides planar alignment for ZLI-2293. We measured some surface and bulk physical properties like polar anchoring energy, pretilt angle and rotational viscosity at room temperature and compared the results with the measured on a common alignment layer AL-1254.

6.2 Experimental

The nematic liquid crystal mixture ZLI-2293 was obtained from Merck, Japan. It exhibits following phase sequence: Cr 21°C N 85°C I. The ITO glass plates were spin coated with polyimide AL-1254 or perfluoropolymer (CYTOP), and were cured at 180 °C and 100 °C for 1 h or 30 min, respectively. After curing, the plates were rubbed by using a homemade rubbing machine. The plates are assembled such that the rubbing directions were set antiparallel. Milar spacer and glass beads were used to make thick ($\sim 100 \mu m$) and thin ($\sim 10 \mu m$) cells. The cells of thickness $\sim 10 \mu m$ were used for measuring anchoring energy and rotational viscosity on the other hand the cells of thicknesses in the ranges 100 to 150 μm were used for measuring pretilt angle. The sample was injected into the empty cell through the capillary action in the nematic phase at room temperature.

6.2.1 Measurement of Polar Anchoring Energy

We adopted Yokoyama and Van sprang [5] technique to measure the polar anchoring energy. This method is based on simultaneous measurement of capacitance C and optical phase retardation R as a function of the voltage V applied to the nematic cell. Consider a slab of Nematic Liquid Crystal (NLC) with positive dielectric anisotropy ($\Delta\epsilon > 0$) and the nematic director is assumed to have a uniform planar orientation in the absence of an electric field. We also assume that both substrates at $z = 0$ and $z = d$ are identically treated and that the NLC is perfectly insulating. By using the angle ϕ that the director makes with the substrate, one can write the excess free energy

6.2 Experimental

per unit area of the NLC as

$$F = \int_0^d \frac{1}{2} \left[(K_{11} \cos^2 \phi + K_{33} \sin^2 \phi) \left(\frac{d\phi}{dz} \right)^2 + \frac{D^2}{(\epsilon_{\parallel} \sin^2 \phi + \epsilon_{\perp} \cos^2 \phi)} \right] dz + 2f_s(\theta), \quad (6.1)$$

The first and second terms in the integral represents the bulk free-energy density and dielectric free-energy density respectively. The boundary conditions denoted by $f_s(\theta) \equiv f(\theta, 0)$, where $\theta = \phi(0) = \phi(d)$ and D represents the electrical displacement, which is uniform through the nematic. K_{11} and K_{33} are the splay and bend elastic constants respectively. ϕ is the angle between the LC director and the substrate rubbing direction (x axis), d is cell gap. The director distribution for a given D is such that $\phi(z)$ has to minimize F . According to the variational calculus, we obtain the Euler-Lagrange equation for $\phi(z)$,

$$\frac{d}{dz} \left[(K_{11} \cos^2 \phi + K_{33} \sin^2 \phi) \left(\frac{d\phi}{dz} \right) - \frac{D^2}{(\epsilon_{\parallel} \sin^2 \phi + \epsilon_{\perp} \cos^2 \phi)} \right] = 0, \quad (6.2)$$

and the boundary condition at $z = 0$ is

$$\frac{df_s(\theta)}{d\theta} = (K_{11} \cos^2 \phi + K_{33} \sin^2 \phi) \left(\frac{d\phi}{dz} \right) \Big|_{z=0}, \quad (6.3)$$

which expresses the torque balance at the interface. Noting that the symmetry of the problem requires $\frac{d\phi}{dz} = 0$ at $z = d/2$, we can integrate equation 6.2 to give

$$\left(\frac{d\phi}{dz} \right)^2 = \frac{\Delta\epsilon D^2}{K_{11} \epsilon_{\parallel}^2} \frac{\cos^2 \phi - \cos^2 \phi_m}{(1 + \gamma \sin^2 \phi)(1 - \eta \cos^2 \phi)(1 - \eta \cos^2 \phi_m)}, \quad (6.4)$$

where $\Delta\epsilon = \epsilon_{\parallel} - \epsilon_{\perp}$, $\eta = \Delta\epsilon/\epsilon_{\parallel}$, and $\gamma = (K_{33} - K_{11})/K_{11}$, and ϕ_m is the maximum angle occurring at $z = d/2$.

The director distortion in the NLC can be detected optically by measuring the phase retardation between the ordinary and the extraordinary rays. For a

Perfluoropolymer as planar alignment layer for liquid crystal mixtures

normally incident beam of wavelength λ the retardation R can be written as

$$R = \frac{2\pi}{\lambda} \int_0^d [n_{eff}(\phi) - n_o] dz, \quad (6.5)$$

where

$$n_{eff}(\phi) = n_o / (1 - \nu \cos^2 \phi)^{1/2}, \nu = (n_e^2 - n_o^2) / n_e^2.$$

n_o and n_e are the refractive indices for the ordinary and extraordinary rays, respectively. Substituting equation 6.4 into equation 6.5, we obtain

$$\begin{aligned} \frac{R}{R_o} = & 2 \left(\frac{K_{11}}{\Delta\epsilon} \right)^{1/2} \frac{\epsilon_{\parallel}}{dD} \int_{\theta}^{\phi_m} \frac{1 - \nu + (1 - \nu)^{1/2}}{1 - \nu \cos^2 \phi + (1 - \nu \cos^2 \phi)^{1/2}} \times \\ & \frac{(1 + \gamma \sin^2 \phi)^{1/2} (1 - \eta \cos^2 \phi)^{1/2} (1 - \eta \cos^2 \phi_m)^{1/2}}{(\cos^2 \phi - \cos^2 \phi_m)^{1/2}} \times \cos^2 \phi d\phi. \end{aligned} \quad (6.6)$$

Here $R_o = 2\pi d(n_e - n_o)/\lambda$ is the retardation in the absence of the electric field. As the applied voltage V increased above the Freedericksz threshold, the elastic distortion inside the NLC tends to localize near the liquid crystal-wall interface. Equation 6.4 shows that the range of localization is roughly given by $d_c = \epsilon_{\parallel}(K_{11}/\Delta\epsilon)^{1/2}/D$, this called the electric coherence length. Let us now assume the cell thickness d to be much larger than the extrapolation length defined by $d_e = K_{11}/A$ so that there exists a range of voltage satisfying the inequality, $d \geq d_c \geq d_e$. In this case, the effect of finite anchoring strength on the Freedericksz transition can be neglected totally, and hence the threshold voltage is given by $V_{th} = \pi(K_{11}/\Delta\epsilon)^{1/2}$. Also noting that the electrical displacement can be related to the applied voltage by $D = CV/S$, where C and S are the capacitance and the electrode area of the NLC cell respectively, we can rewrite equation 6.3 and 6.6 as

$$\frac{df_s(\theta)}{d\theta} = \pi \frac{K_{11}}{d} \frac{CV}{\xi} \frac{(1 + \gamma \sin^2 \theta)^{1/2}}{(1 - \eta \cos^2 \theta)^{1/2}} \cos \theta, \quad (6.7)$$

6.2 Experimental

where $\xi = (\epsilon_{\parallel} S/d) \times \pi(K_{11}/\Delta\epsilon)^{1/2}$, and

$$\frac{R}{R_0} = \frac{\xi}{CV} I(\eta, \gamma, \nu, \theta), \quad (6.8)$$

$$I(\eta, \gamma, \nu, \theta) \equiv \frac{2}{\pi} \int_{\theta}^{\pi/2} \frac{1 - \nu + (1 - \nu)^{1/2}}{1 - \nu \cos^2 \phi + (1 - \nu \cos^2 \phi)^{1/2}} \times \\ (1 + \gamma \sin^2 \phi)^{1/2} (1 - \eta \cos^2 \phi)^{1/2} \cos \phi d\phi. \quad (6.9)$$

Assuming θ is small and hence $f(\theta) \approx 1/2 \times A\theta^2$. The equation 6.8 becomes

$$\frac{R}{R_0} = \frac{\xi}{CV} I(\eta, \gamma, \nu, 0) - 2 \frac{K_{11}}{Ad}. \quad (6.10)$$

This equation shows that, if R/R_0 is plotted against $1/CV$, we obtain a straight line, as long as $d \geq d_c \geq d_e$, having the slope $\xi I(\eta, \gamma, \nu, 0)$ and the intersection with the ordinate axis.

6.2.2 Measurement of Pretilt Angle:

There are several methods to measure pretilt angle. Here we have used crystal rotation method because it is simple, precise and rapid measurement [6]. Consider, for example, a light beam incident on a uniaxial crystal section of thickness d in the cartesian coordinate system. The z axis is normal to the layer, and the xz plane, the principal plane, is also the plane of incidence. The two angles ϕ and α are implicitly defined by the vectors

$$S = (-\sin \phi, 0, -\cos \phi), -90 \leq \phi \leq 90 \\ L = (\cos \alpha, 0, \sin \alpha), 0 \leq \alpha \leq 90,$$

where S is the wave normal of the incident beam and L is the optic axis direction. The incident light breaks up into ordinary and extraordinary waves

Perfluoropolymer as planar alignment layer for liquid crystal mixtures

which propagates through the layer with different velocities and emerge from the other side with a relative phase shift given by [7]

$$\delta\phi = 2\pi \frac{d}{\lambda} \times \left[\frac{1}{c^2} (a^2 - b^2) \sin \alpha \cos \alpha \sin \phi + \frac{1}{c} \left(1 - \frac{a^2 b^2}{c^2} \sin^2 \phi \right)^{1/2} - \frac{1}{b} (1 - b^2 \sin^2 \phi)^{1/2} \right],$$

with $a = 1/n_e$, $b = 1/n_o$

and

$$c^2 = a^2 \cos^2 \alpha + b^2 \sin^2 \alpha,$$

where λ is the wavelength of the incident light and n_o and n_e are the ordinary and extraordinary refractive indices of the nematic liquid crystal. The transmission of light through this uniaxial section placed between the crossed polarizers and oriented with its principal plane at 45° to the plane of polarized light is given by [7]

$$T(\phi) = \frac{1}{2} \sin^2 \left(\frac{\delta\phi}{2} \right). \quad (6.11)$$

Usually, CRM is used for measuring pretilt angle less than 10° .

6.2.2.1 Incident Angle Correction

It should be noted that the incident angle ϕ is not identical with the rotation angle, that is -45° to $+45^\circ$, since the beam is bent away at the glass boundary as shown in Figure 6.1. Let n_g , n_{LC} denotes the refractive index of glass and that of the LC medium confined between two glass plates, respectively. Using Snell's law, we can write

$$\frac{\sin \phi_{rot}}{\sin \phi_g} = n_g,$$

6.2 Experimental

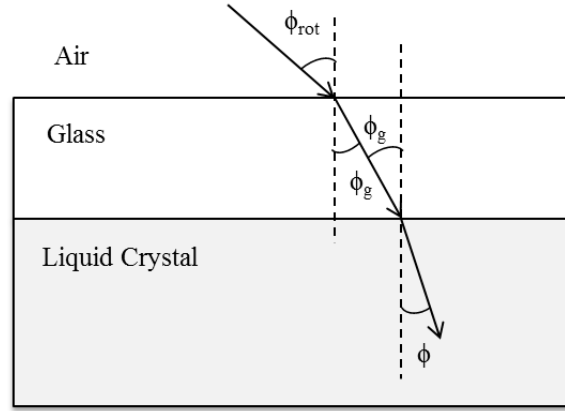


Figure 6.1: Propagation of incident light through air, glass and liquid crystal medium respectively.

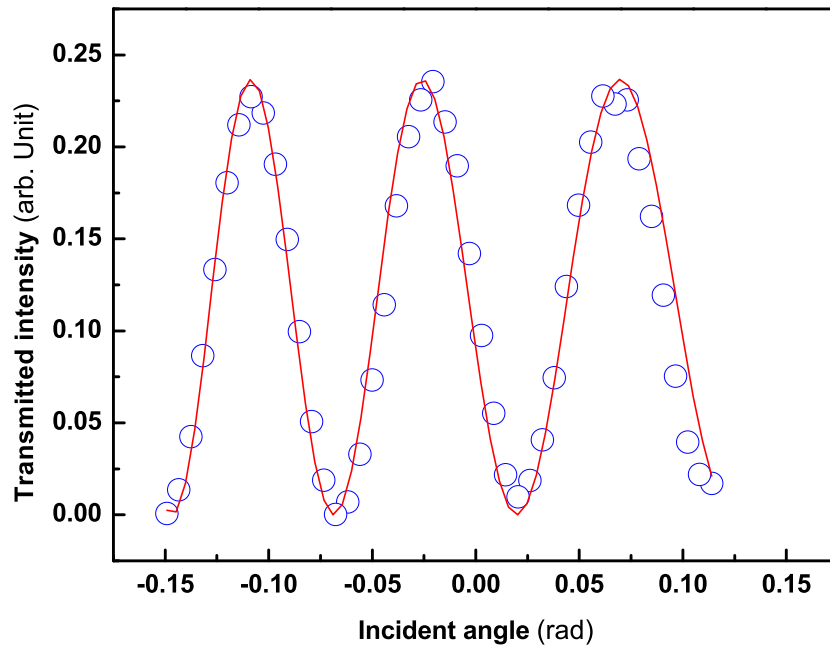


Figure 6.2: Measurement of pretilt angle of 5CB in SE 7492 treated cells. The open circles represent the experimental data points and the solid line denotes the best fit to the equation 6.11.

$$\frac{\sin \phi_g}{\sin \phi} = \frac{n_{LC}}{n_g},$$

where ϕ_{rot} , ϕ_g , ϕ are the rotation angle, the refractive angle in the glass medium and the refractive angle (or the actual incident angle) in the LC medium, respectively. The actual incident angle is given by

$$\phi = \arcsin \left(\frac{\sin \phi_{rot}}{n_{LC}} \right).$$

If we assume that n_{LC} is about 1.5, then the actual incident angle is approximately -28° to $+28^\circ$.

The experimental setup for measuring pretilt angle (α) is calibrated with the liquid crystal 5CB filled in SE 7492 (planar alignment) treated cells of thickness $66\mu m$. The obtained α value at room temperature is $9^\circ \pm 1$ and is comparable to the reported value [8]. Variation of transmitted intensity as a function of incident angle is plotted as shown in Figure 6.2. The open circles in the Figure 6.2 corresponds to experimental data where as the solid line denotes fit to the equation 6.11.

6.2.3 Measurement of Rotational Viscosity

Several experimental methods have been developed for measuring rotational viscosity. The method we used in this study is the phase-decay-time measurement [9, 10] of a parallel-aligned LC cell under small excitation voltage. The equation of motion of parallel aligned liquid crystal under electric field is given by [11, 12]

$$\begin{aligned} (K_{11} \cos^2 \theta + K_{33} \sin^2 \theta) \frac{d^2 \theta}{dx^2} + (K_{33} - K_{11}) \sin \theta \cos \theta \left(\frac{d\theta}{dx} \right)^2 \\ + \epsilon_0 \Delta \epsilon E^2 \sin \theta \cos \theta = \gamma_1 \frac{d\theta}{dt} + I \frac{d^2 \theta}{dt^2}, \end{aligned} \quad (6.12)$$

ignoring the back flow and inertial effects, and under small angle and one constant approximation ($\sin \theta \sim \theta$ and $K_{11} \sim K_{33}$) we get

6.2 Experimental

$$K_{11} \frac{d^2\theta}{dx^2} + \epsilon_0 \Delta \epsilon E^2 \theta = \gamma_1 \frac{d\theta}{dt}, \quad (6.13)$$

when the electric field is switched off then

$$K_{11} \frac{d^2\theta}{dx^2} = \gamma_1 \frac{d\theta}{dt}, \quad (6.14)$$

and the solution is given by

$$\theta(x, t) = \theta_m \sin\left(\frac{\pi x}{d}\right) \exp\left(\frac{-t}{\tau_0}\right), \quad (6.15)$$

where $\tau_0 = \frac{\gamma_1 d^2}{K_{11} \pi^2}$ and θ_m is minimum tilt angle at the center of cell. The phase decay time of parallel aligned liquid crystal cell is expressed as [10]

$$\delta(t) = \delta_0 \exp(-2t/\tau_0), \quad (6.16)$$

when δ_0 is equal or in the vicinity of $(N + 1/2)\pi$ and

$$\delta(t) = \delta_0 \exp(-4t/\tau_0), \quad (6.17)$$

when δ_0 is equal or in the vicinity of $N\pi$. The time dependent transmitted intensity is

$$I = I_0 \sin^2 \left[\frac{(\Delta_{tot} - \delta(t))}{2} \right]. \quad (6.18)$$

The experimental procedure consists of two steps (i) measurement of voltage dependent intensity at a fixed temperature and (ii) measurement of time dependent transmitted intensity after switching off electric field. The voltage dependent intensity is measured with PMT. A small voltage (V_b) corresponding to the first maxima or minima was applied depending on the transmission intensity, such that the total phase retardation of the sample was $N\pi$. At time $t = 0$, the bias voltage (V_b) was removed and the relaxation transmission intensity change of the liquid crystal cell was measured with an oscilloscope.

The transmitted intensity is given by equation 6.18. The phase difference $\delta(t)$ for small director deformation given by equation 6.16 is calculated from equation 6.18. The plot between $\ln[\delta_0/\delta(t)]$ and time t is drawn. The slope of this plot gives τ_0 . The rotational viscosity (γ_1) of the liquid crystal is calculated using

$$\gamma_1 = \frac{\tau_0 K_{11} \pi^2}{d^2}, \quad (6.19)$$

where d is the cell thickness.

6.3 Results and Discussion

The photograph and transmission spectra of bare ITO and CYTOP coated glass plates [13] are shown in Figure 6.3. It is clear from the spectra that the transmission intensity through CYTOP is higher than the bare ITO. Here we show the visual difference of glass plate coated with AL-1254 and CYTOP. The photograph shown in the Figure 6.4 represent the CYTOP coated plate appears more transparent than AL-1254 due to the high transmission of CYTOP. The atomic force micrographs shown in Figure 6.5 shows the surface morphology of CYTOP glass plate before and after rubbing. It is clear from Figure 6.5(a) that the CYTOP provides uniform surface on the glass plate. The micrograph shown in Figure 6.5(b) was taken after rubbing the same glass plate with soft velvet cloth. Generally rubbing generates microgrooves on the glass plates. From Figure 6.5(b) it is clear that the rubbing is uniform except few places where the surface is over rubbed. The arrow in Figure 6.5(b) shows rubbing direction. The texture of nematic phase of ZLI-2293 in rubbed cell under polarizing optical microscope with the rubbing direction $\psi = 0$ and 45° are also shown in Figure 6.6. A complete dark state ($\psi = 0^\circ$) and a uniform bright state ($\psi = 45^\circ$) indicate good uniform alignment of director in the entire nematic phase. To measure anchoring energy we adopted a high field technique as we discussed in section 6.2.1. A computer controlled LabVIEW program was used to measure the optical retardation (R) and

6.3 Results and Discussion

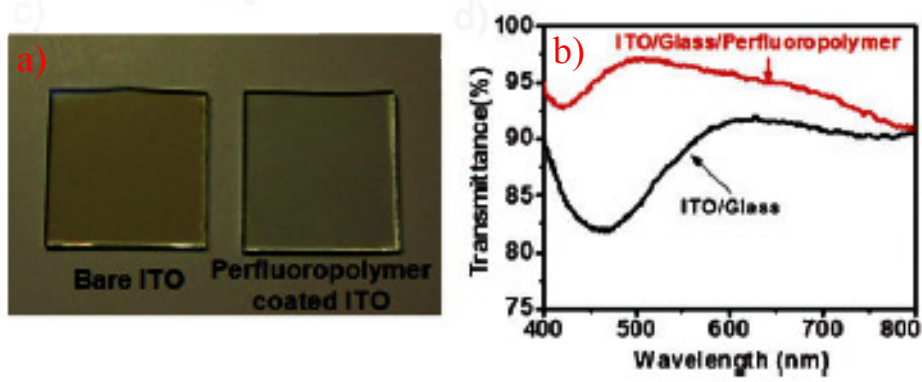


Figure 6.3: Photograph of (a) bare and CYTOP coated ITO glass plates (b) transmission spectrum of bare and CYTOP coated ITO glass plates (adopted from reference [13]).

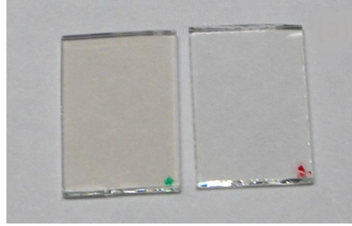


Figure 6.4: The green and red dots on the right corners of the ITO glass plates represents the coating of AL-1254 and CYTOP respectively.

sample capacitance (C) simultaneously. The schematic and a photograph for measuring anchoring energy is shown in Figure 6.7 and 6.8. A He-Ne laser of wavelength 632.8 nm was used as source for optical measurements and the cell is placed between two crossed Glan Thompson polarizers. The temperature of the cell was maintained by a Instec (mK 1000) temperature controller. A LCR meter (Agilent E4980A) was used to measure the cell capacitance as a function of voltage. The transmitted light intensity I was measured using a photodiode. If the intensity of light after polarizer is I_0 then the intensity at detector is given by

$$I = I_0 \sin^2(2\psi) \sin^2\left(\frac{\pi R}{\lambda}\right), \quad (6.20)$$

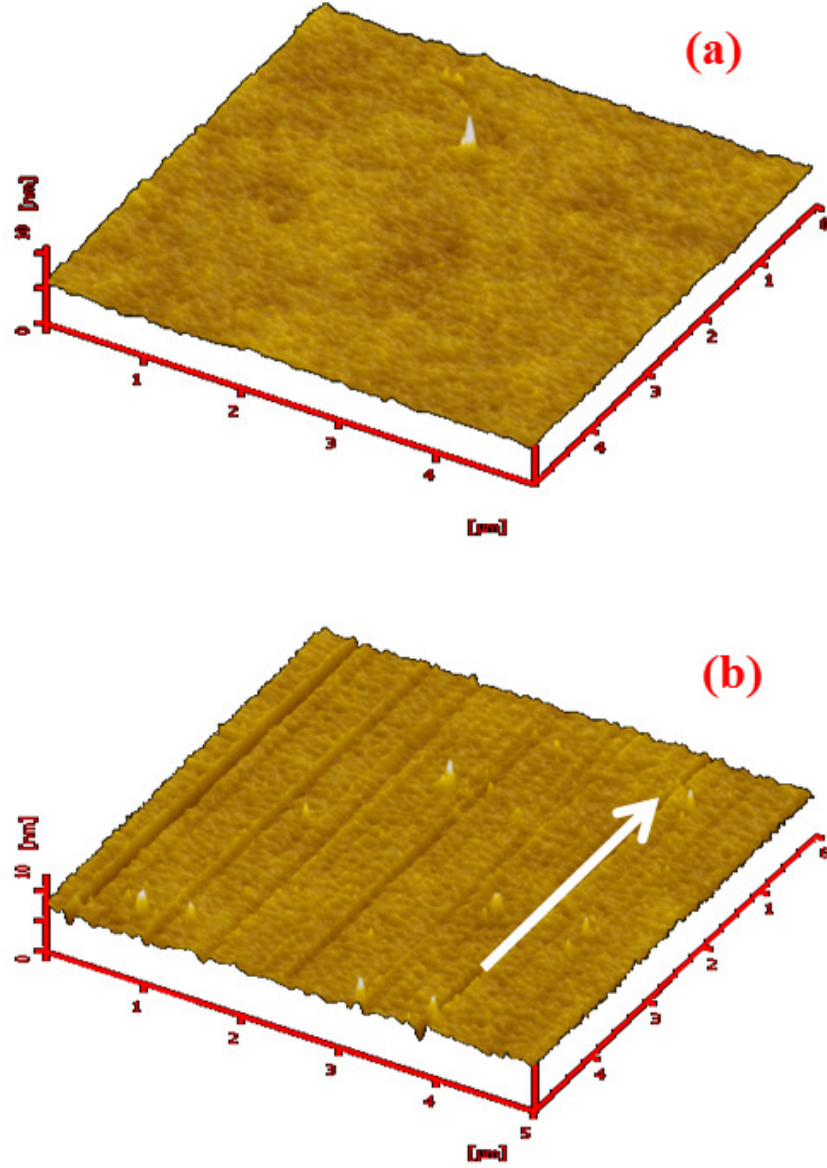


Figure 6.5: The atomic force microscope pictures of CYTOP coated ITO glass plates: (a) before (b) after rubbing.

where ψ is the angle made by the optical axis of the uniaxial material with polarizer and $R = \Delta nd$. In our setup we placed liquid crystal cell with an angle of 45° (i.e $\psi = 45^\circ$) to the polarizer. Hence, intensity measured at

6.3 Results and Discussion

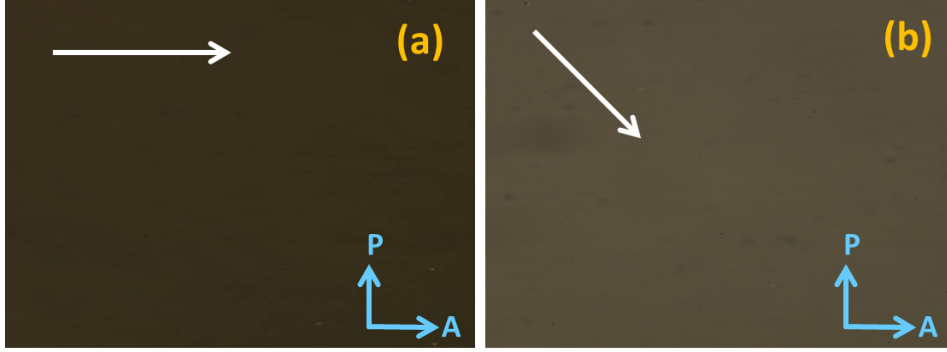


Figure 6.6: Photomicrographs of CYTOP coated cell with ZLI-2293 sample is at room temperature. An arrow in the picture denotes the rubbing direction (a) rubbing direction $\psi = 0^\circ$ and (b) rubbing direction $\psi = 45^\circ$.

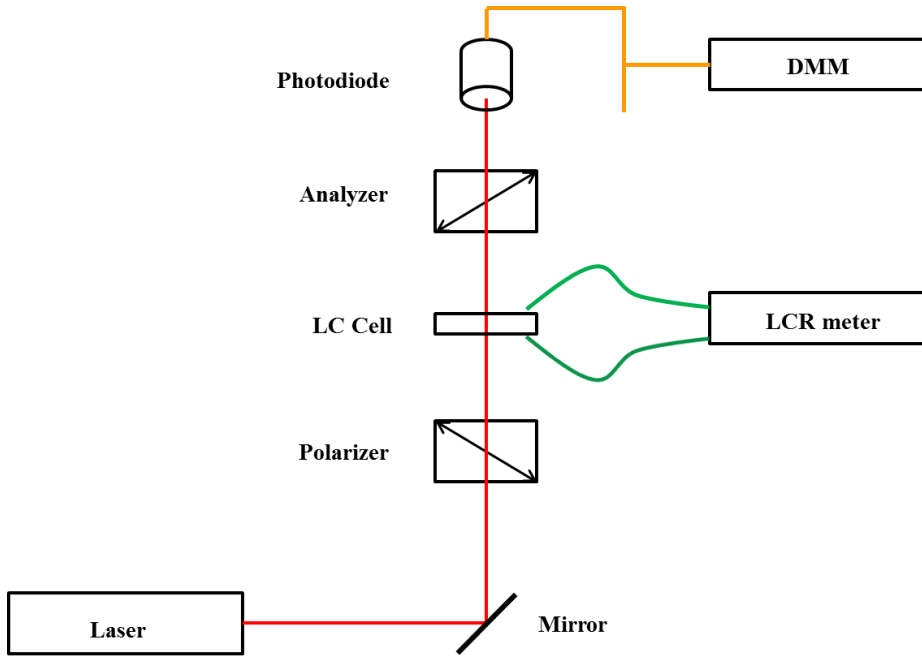


Figure 6.7: Schematic diagram of experimental setup for measuring retardation and capacitance.

detector is given by

$$I = I_0 \sin^2 \left(\frac{\pi R}{\lambda} \right), \quad (6.21)$$

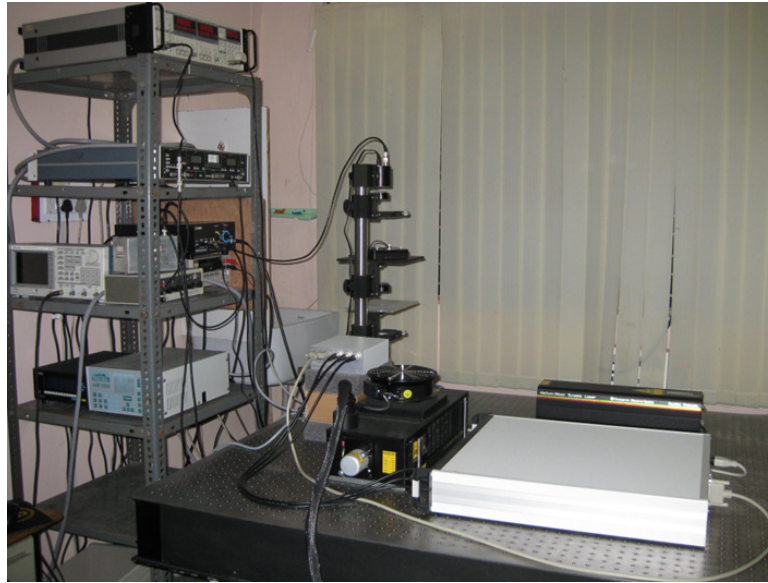


Figure 6.8: Photograph of experimental set up for measuring retardation and capacitance.

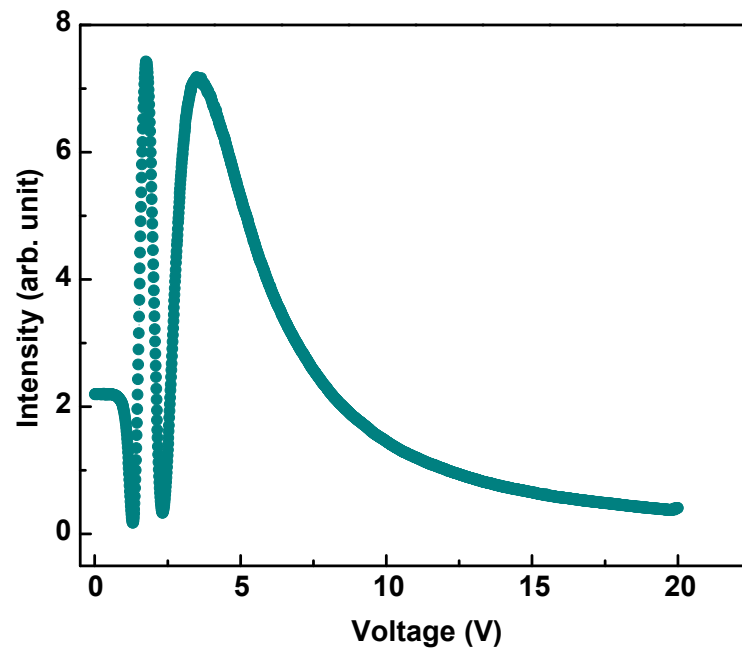


Figure 6.9: The variation of intensity as a function of voltage in CYTOP cell at room temperature.

6.3 Results and Discussion

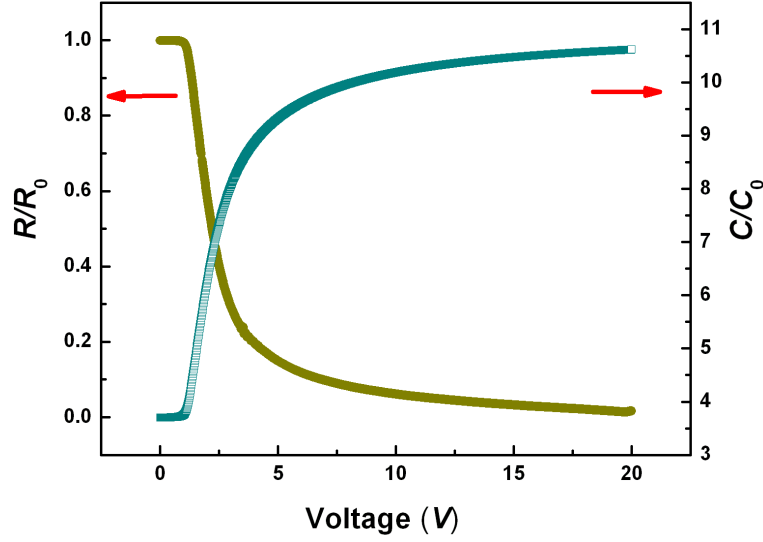


Figure 6.10: Variation of normalized retardation (R/R_0) and the ratio of the sample capacitance to the empty cell capacitance (C/C_0) as a function of voltage in a CYTOP coated cell at room temperature.

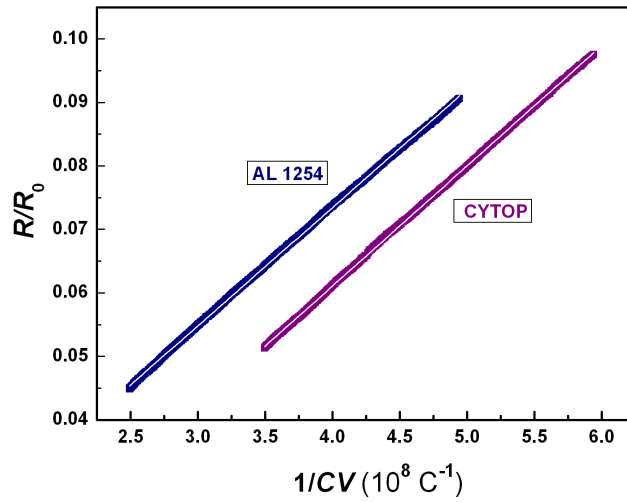


Figure 6.11: The variation of R/R_0 versus $1/CV$ in AL-1254 and CYTOP coated cells at room temperature. The data are well fitted to equation 6.10.

Perfluoropolymer as planar alignment layer for liquid crystal mixtures

where Δn is an effective birefringence of the material, λ is the wavelength of light, d is the thickness of the sample, and ψ is the angle that the optical axis of the uniaxial material makes with polarizer. The variation of intensity as a function of voltage in CYTOP cell at room temperature is shown in Figure 6.9. The anchoring strength (A) is estimated from the following equation 6.10 [5, 14]. Typical variation of normalized retardation R/R_0 and capacitance C/C_0 as a function of applied voltage is shown in Figure 6.10. We obtain the threshold voltage $V_{th}=1.16$ V and estimated splay elastic constant $K_{11} \simeq 8.9 \times 10^{-12}$ N. We have shown the variation of R/R_0 with $1/CV$ in the voltage range of 8 to 17 V in Figure 6.11. Good linear fits were obtained in the above voltage range. From the intercept to the ordinate axis we obtain the anchoring strength; $A \simeq 1.0 \times 10^{-4}$ J/m² in a CYTOP cell and $A \simeq 18.3 \times 10^{-4}$ J/m² in a AL-1254 cell. Note that A in a CYTOP cell is more than eighteen times smaller than A in a AL-1254 cell. Similar values of anchoring energy ($A \sim 17 \times 10^{-4}$ J/m²) of ZLI-2293 on other polyimide at room temperature was reported by You *et al* [14]. Low surface anchoring properties of 5CB (4-cyano-4'-pentyl-1, 1' biphenyl) on Langmuir-Blodgett films of similar polymer (perfluoropolyether) was reported by Russel-Tanner *et al* [15]. Furthermore, CYTOP also provides perfect homeotropic alignment of smectic liquid crystals exhibiting its low surface anchoring properties [13]. We adopted the crystal rotation method (CRM) [6] to measure the pretilt angle as mentioned in 6.2.2. The schematic diagram and photograph of experimental set up of pretilt angle measurement is shown in Figure 6.12 and 6.13. The pretilt angle experimental set up consists of He-Ne (3mW) light source, polarizers, rotating stage and a detector. The whole experimental setup is controlled by LabVIEW program. Polarizers are placed such that they are crossed. A thick LC cell of thickness $\approx 100\mu\text{m}$ was placed in temperature controller and temperature controller is placed on a rotating stage such that it can rotate from -45° to $+45^\circ$. The transmitted intensity was measured with a photodiode as a function of the incidence angle from -45° to $+45^\circ$ about the axis perpendicular to the light beam and the rubbing direction. The transmitted intensity of CYTOP coated cell as a function of incidence angle is shown in Figure 6.14. The transmitted intensity was fitted to the

6.3 Results and Discussion

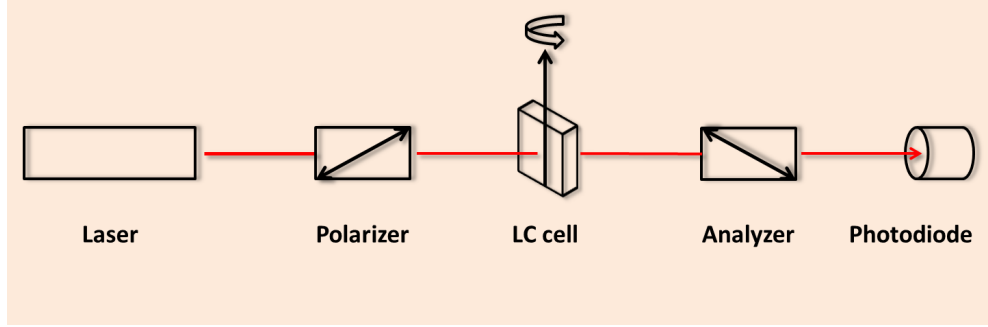


Figure 6.12: Schematic diagram of pretilt angle measurement setup.



Figure 6.13: Photograph of experimental set up of pretilt angle measurement.

theoretical equation 6.11 [6]. A good fit to the theoretical equation gives pretilt angle $\alpha \sim 2^\circ$. In case of AL-1254 it is $\alpha \sim 1^\circ$, which is slightly smaller than CYTOP coated cell.

To measure rotational viscosity (γ_1) we adopted phase decay time measurement technique which was discussed 6.2.3. We measured the transmitted light intensity through a planar aligned LC cell, to obtain the optical phase as a function of time. The phase change $\delta(t)$ as a function of time t was measured from the time dependent intensity equation 6.18. The variation of intensity as a function of time in CYTOP cell at room temperature is shown in Figure 6.15. The decay time is given by the equation 6.16 [9, 10]. The rotational

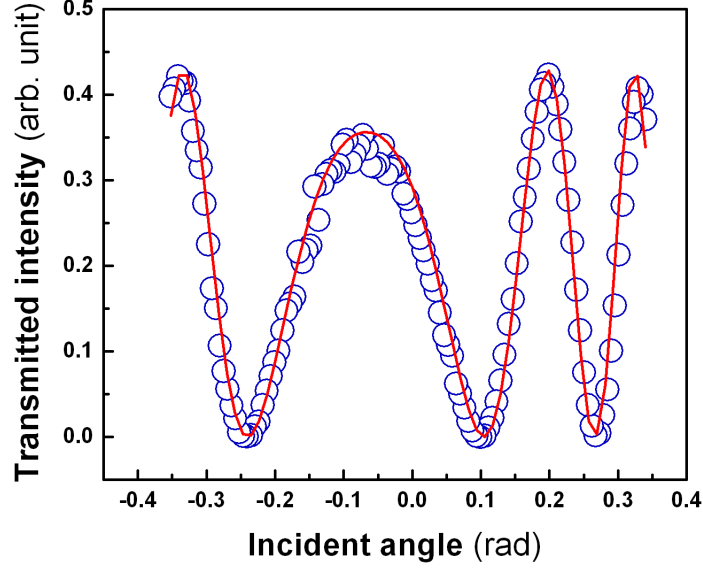


Figure 6.14: Transmitted intensity versus incident angle for ZLI-2293 in a CYTOP coated cell at room temperature. The circles represent the experimental data points and the solid line denotes the best fit to the equation 6.11.

viscosity (γ_1) of the sample is estimated by equation 6.19. All the experiments were performed at room temperature (27 °C). We have shown the variation of $\ln[\delta(0)/\delta(t)]$ as a function of time t in Figure 6.16. A good fit of the experimental data with the theoretical equation is obtained (Figure 6.16). The slope of this linear plot is $2/\tau_0$, which yields the relaxation times 107 and 99 ms in CYTOP and AL-1254 coated cells, respectively. The calculated rotational viscosities are 0.08 ± 0.01 and 0.10 ± 0.01 Pa s respectively, and agree within an experimental error due to the cell thickness measurement, the accuracy of which is within $\pm 5\%$. Rotational viscosity of this compound was also measured by using a transient current method by Imai *et al.* [16] and was slightly larger (0.14 Pa s) than our results. Finally we present the summary of the obtained quantities, anchoring strength (A), pretilt angle (α), and rotational viscosity (γ_1) in cells coated with CYTOP and AL-1254

6.3 Results and Discussion

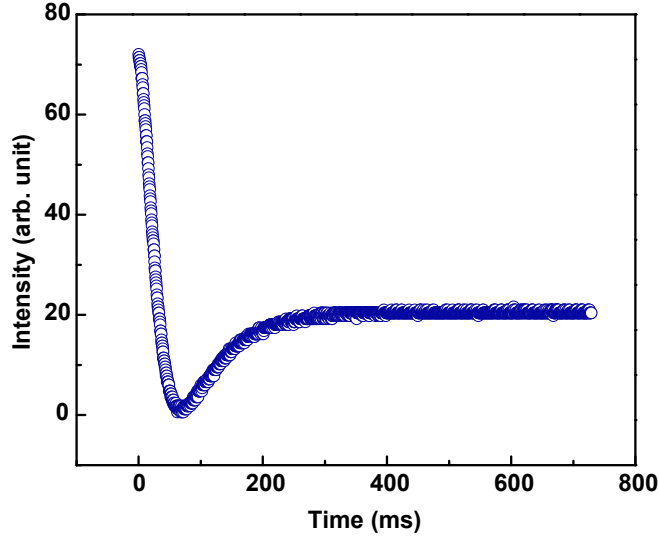


Figure 6.15: The variation of intensity as a function of time in CYTOP cell at room temperature.

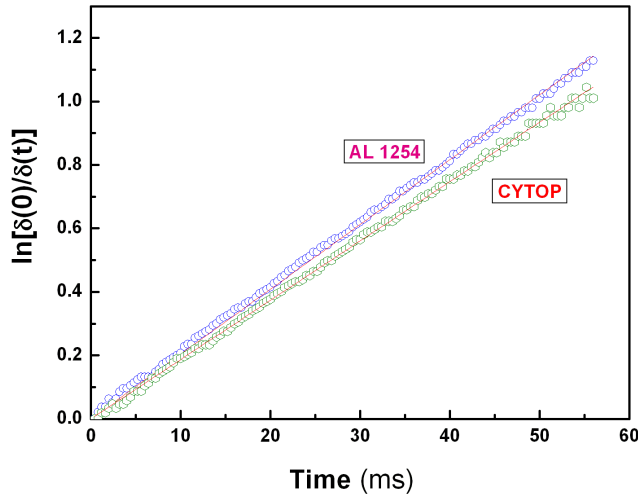


Figure 6.16: $\ln [\delta(0)/\delta(t)]$ versus time t for ZLI-2293 at room temperature. The open circles represent the experimental data for both alignment layers and the solid lines represent the best fit to the equation $\ln [\delta(0)/\delta(t)] = -2t/\tau_0$. Cell thickness $d = 9.5 \pm 0.5 \mu\text{m}$ (AL-1254) and $10.6 \pm 0.5 \mu\text{m}$ (CYTOP) respectively.

REFERENCES

	$A(\times 10^{-4} \text{ J/m}^2)$	$\alpha \text{ (deg)}$	$\gamma_1 \text{ (Pa s)}$
CYTOP	1.0	2	0.08
AL-1254	18.3	1	0.10

Table 6.1: Summary of the physical properties of ZLI-2293 on both alignment layer, CYTOP and AL-1254.

in Table I. It is noted that the anchoring energy in CYTOP coated cell is significantly low compared to AL-1254 coated cell.

6.4 Conclusions

In conclusion, our measurements show that CYTOP can be used as a planar alignment layer for ZLI-2293. It provides much lower surface anchoring energy than AL-1254. The low anchoring energy is attributed to the low surface free energy and is supported by the fact that CYTOP provides larger contact angle than other alignment layers for liquid crystals. The pretilt angles are not significantly different and hence suitable for the application. It is expected that the advantage of high transmission through CYTOP cell will be very useful for better performance of LCD. However, display performances using many other nematic mixtures should be studied for further details.

References

- [1] K. Takato, M. Sakamoto, R. Hasegawa, M. Koden, N. Itoh, and M. Hasegawa: *Alignment technologies and applications of liquid crystal devices*, Taylor and Francis, London, 2005.
- [2] M. E. Becker, J. Nehring, and T.J. Scheffer, “Theory of twisted nematic layers with weak boundary coupling”, *J. Appl. Phys.* **57**, 4539 (1985).

REFERENCES

- [3] L. M. Blinov and V.G. Chigrinov, *Electrooptic effects in liquid crystal materials*, Springer, New York, 1994.
- [4] G. P. B. Brown, E. L. Wood, and I. C. Sage, “Weak surface anchoring of liquid crystals”, *Nature (London)* **399**, 338 (1999).
- [5] H. Yokoyama and H. A. Sprang, “A novel method for determining the anchoring energy function at a nematic liquid crystal wall interface from director distortions at high fields”, *J. Appl. Phys.*, **57**, 4520 (1985).
- [6] T. J. Scheffer and J. Nehring, “Accurate determination of liquid crystal tilt bias angles”, *J. Appl. Phys.*, **48**, 1783 (1977).
- [7] M. Francon, *Handbuch der Physik*, Vol. XXIV, Springer, Berlin, pp. 441-445, 1956.
- [8] K. V. Le, S. Dhara, B. K. Sadashiva, Y. Takanishi and H. Takezoe, “Characterization of nematic phase of banana liquid crystal”, *Jpn. J. Appl. Phys.*, **45**, L1013 (2006).
- [9] S. T. Wu and C. S. Wu, “Experimental confirmation of the Osipov-Terentjev theory on the viscosity of nematic liquid crystals”, *Phys. Rev. A* **42**, 2219 (1990).
- [10] S. T. Wu, “Phase retardation dependent optical response time of parallel aligned liquid crystals”, *J. Appl. Phys.*, **60**, 1836 (1986).
- [11] J. L. Ericksen, “Conservation laws for liquid crystals”, *Trans. Soc. Rheol.* **5**, 23 (1961).
- [12] F. M. Leslie, “Some constitutive equations for liquid crystals”, *Arch. Ration. Mech. Anal.*, **28**, 265(1968).
- [13] S. M. Jeong, Y. Shimbo, F. Araoka, S. Dhara, Na Young Ha, K. Ishikawa, and H. Takezoe, “Perfluoropolymer surface for shock free homeotropic alignment of smectic liquid crystals”, *Adv. Mater.*, **21**, 1 (2009).

REFERENCES

- [14] D. H. You and S. D. Lee, “Temperature dependence of anisotropic surface anchorage of nematic liquid crystals”, *Mol. Cryst. Liq. Cryst.*, **316**, 215 (1998).
- [15] J. M. R. Tanner, S. Takayama, A. Sugimura, J. M. DeSimone, and E. D. Samulski, “Weak surface anchoring energy of 4-cyano-4'-pentyl-1,1'-biphenyl on perfluoropolyether Langmuir-Blodgett films”, *J. Chem. Phys.*, **126**, 244706 (2007).
- [16] M. Imai, H. Naito, M. Okuda, and A. Sugimura, “Determination of rotational viscosity of nematic liquid crystals from transient current: Numerical analysis and experiment”, *Jpn. J. Appl. Phys.*, **33**, 3482 (1994).

7

Alignment of unconventional nematic liquid crystals

7.1 Introduction

In the previous chapter we have discussed the alignment properties of a room temperature nematic liquid crystal mixture in CYTOP treated cells. In this chapter we will study the alignment behaviour of some unconventional nematic liquid crystals on various common alignment layers.

Uniform orientation of liquid crystal director on treated substrates is fundamentally as well as technologically very important. It is also an essential requirement for any quantitative measurement of various physical properties of liquid crystals. There are two types of alignment layers namely: planar (homogeneous) and vertical (homeotropic). Planar alignment layer provides planar orientation of the director i.e the director is parallel to the substrate. On the other hand homeotropic alignment layer provides homeotropic orientation of the director i.e the director is perpendicular to the substrate. These alignment layers are very much stable i.e. the director orientation does not change with time and temperature. Most of the uniaxial liquid crystals made of rod like molecules (calamitic) can be aligned easily in the nematic phase both in planar and homeotropic cells. Majority of the commercially available

liquid crystal display devices (LCDs) make use of these alignment layers. The liquid crystals which are made of other than rod like molecules (unconventional nematic liquid crystals) so far have not been used in LCDs. Recently, liquid crystals made of bent-core molecules has drawn much attention because of their many uncommon physical properties such as emerging biaxial nematic phase [1] unconventional electroconvection [2, 3], flexoelectric [4] and Kerr effect [5], sign inversion of elastic anisotropy [6], larger shear and rotational viscosities [7, 8], low pretilt angle [9], compared to the calamitic liquid crystals. Wiant *et al.* [2] have characterized three nonstandard electrohydrodynamic instabilities in nematic liquid crystals composed of bent-core molecules. In addition to their shape, these instabilities attributed to anisotropy in the electrical conductivity which changes sign as the frequency of the applied electric field changes. The similar type of instability observed by Tanaka *et al.* [3]. They reported electroconvection effect in a different type of a bent-core nematic liquid crystal with a very different molecular structure. In 2006 Harden *et al.* [4] have found giant flexoelectricity of bent core nematic liquid crystals. They used a direct method for measuring the flexoelectric coefficients of nematic liquid crystals via the electric current produced by periodic mechanical flexing of the nematic liquid crystals' bounding surfaces. Their results reveal that the bend flexoelectric coefficient of bent-core NLCs is more than 3 orders of magnitude larger than in calamitics. Dhara *et al.* [5] have measured the electro-optical Kerr constant (B) and the third-order nonlinear susceptibility ($\chi^{(3)}$) of a bent-core liquid crystal in the isotropic phase. Sathyanarayana *et al.* [6] have measured the temperature dependence of K_{11} and K_{33} of a pure bent-core liquid crystal and reported that they are significantly different from that in rodlike molecules and K_{33} is much lower compared to K_{11} . Dorjgotov *et al.* [7] have measured the rotational viscosity (γ_1) and found it is more than ten times larger than for calamitic liquid crystals, the flow viscosity is more than 100 times larger. Their results suggest that the large shear viscosity is primarily due not so much to the molecular size, but rather the shape. Recently, Sathyanarayana *et al.* [8] also have measured the rotational viscosity (γ_1) of a bent-core nematic liquid crystal with positive dielectric anisotropy as a function of temperature and

7.2 Experimental

found that γ_1 is slightly larger than that for the calamitic nematics. K.V. Le *et al.* [9] have reported the detailed optical and electrical characterizations of the nematic phase of a banana liquid crystal. They measured pretilt angle, optical and dielectric anisotropies, and pointed out the difference from those of rodlike molecules. In many of these measurements the director is aligned uniformly in planar cell. There are some reports which show that bent-core nematic liquid crystals do not align homeotropically with on conventional alignment layers [10, 11]. The reason for such behaviour is not studied and understood in detail. In this chapter we studied the alignment behaviour of some unconventional nematic liquid crystals, such as bent-core, T-shape, hockey stick-shaped etc., on some common alignment layers.

7.2 Experimental

For planar alignment we have used AL-1254, and for homeotropic alignment JALS-204 and SE-1211 were used as alignment layers. The ITO glass plates were spin coated with AL-1254 and then cured at 180°C for an hour. Similarly, we have spin coated ITOs with JALS-204 and SE-1211. After coating, ITOs were cured for an hour at 200°C and 180°C respectively. Planar alignment was achieved by rubbing glass plates antiparallel way. A UV curable adhesive with $\sim 5\mu m$ spacer was used to make cells. In this experiment we have used cells of thickness ranges from 4 – 8 μm . Samples were filled in the isotropic phase and cooled slowly across the nematic-isotropic transition.

Polar anchoring energy of the compound with $\Delta\epsilon = (\epsilon_{||} - \epsilon_{\perp}) < 0$ was measured in homeotropic cell by using a technique proposed by Nie *et. al* [12]. When the applied voltage exceeds a threshold, the liquid crystal director in the bulk is reoriented and the reorientation at the surface occurs at much higher voltage due to the finite surface anchoring. Nie *et. al* [12] showed that the anchoring energy in homeotropic cell can be measured from the voltage dependent retardation data when other material parameters are known. The sample capacitance and the retardation were measured simultaneously as a function of voltage. A schematic diagram and a photograph of the experimental set up to

measure birefringence and capacitance of liquid crystals is already represented in the previous chapter (Figure 6.6 and 6.7.). The sample was placed between two Glan-Thomson polarizers. A He-Ne laser (632.8nm) was used as light source. A narrow beam of light was extracted from pinholes and was allowed to incident on the LC cell. A temperature controller (Instec mK 1000) was used to maintain uniform temperature throughout the experiment. A LCR meter (Agilent E4980A) was connected to supply the voltage upto $20V_{rms}$ to the cell. The same LCR meter was used to measure capacitance of the sample. A photodiode is placed after the analyzer to measure transmitted intensity. The retardation was estimated from the measured intensity using equation 6.21. All the measurements were controlled with the help of a computer. The anchoring strength (A) is calculated from the following Equation [12]

$$\frac{R}{R_0} = -\frac{1}{CV} \frac{\xi}{\Delta n} I(b, \gamma, \nu, \pi/2) + \left(1 + \frac{2K_{33}}{Ad}\right), \quad (7.1)$$

where $\xi = (\epsilon_0 \epsilon_{\perp} S/d) \pi \sqrt{K_{33}/\Delta\epsilon}$ and

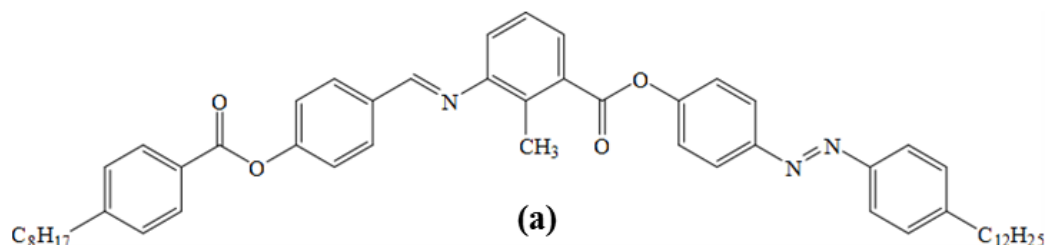
$$I(b, \gamma, \nu, \theta) = \frac{2}{\pi} \int_0^{\theta} \frac{1 - \nu + (1 - \nu)^{1/2}}{1 - \nu \cos^2 \phi + (1 - \nu \cos^2 \phi)^{1/2}} \times \frac{(1 + \gamma \cos^2 \phi)^2 (1 + b \sin^2 \phi)^{1/2}}{\sin \phi} d\phi, \quad (7.2)$$

where R_0 is the maximum retardation and R/R_0 is the normalized phase retardation. C , V , d and S are the sample capacitance, applied voltage, cell thickness and electrode area. $\nu = (n_e^2 - n_0^2)/n_e^2$ where n_e and n_0 are the extraordinary and ordinary refractive indices, $\gamma = (K_{11} - K_{33})/K_{33}$ and $b = (\Delta\epsilon)/\epsilon_0 \epsilon_{\perp}$. K_{33} is the bend elastic constant and is measured from the Freedericksz threshold voltage (V_{th}). $(\xi/\Delta n)I(b, \gamma, \nu, \pi/2)$ depends on the material parameters and is independent of voltage. Polar anchoring energy, A is determined from the intercept of the plot R/R_0 as a function of $1/CV_{rms}$.

7.3 Results and Discussion

Several compounds with unconventional molecular structures and in various temperature ranges of the nematic phase were chosen for this experiment. The compounds are named as C1, C2, C3, C4, C5 and C6 for convenience. Texture observation of these compounds was made by using a polarizing optical microscope (Olympus BX-51) connected with a Instec hotstage (Instec Inc.) and digital camera. Objective of 10X was used to observe the textures through out this experiment. The samples were cooled at the rate of 1°C/min. Textures obtained in planar and homeotropic cells for bent-core nematic liquid crystals are shown in Figure 7.1 to 7.3. The chemical name of C1 is (4-[(4-dodecylphenyl) diazenyl] phenyl 2-methyl-3-[4-(4-octylbenzoyloxy) benzylideneamino] benzoate. It has following phase transitions: Cr 77.8°C SmC 109.1°C N 173.4°C I. The chemical structure of the compound is shown in Figure 7.1(a). It has positive dielectric anisotropy of $\Delta\epsilon \simeq 1$ at $T_{NI} - T = 20^\circ$ and exhibits a large temperature range of the nematic phase. Various physical measurements on C1 such as anchoring transition, electro-optics properties, splay-bend elasticity and rotational viscosity have already been reported [6, 13–16]. Uniform planar and homeotropic alignments of the nematic director were obtained in planar and homeotropic cells respectively. The photomicrographs of planar and homeotropic alignments of the director of compound C1 are shown in Figure 7.1(b) and Figure 7.1(c). The homeotropic state is very stable in the entire nematic phase except for slight tilting of the director at much lower temperature in some parts of the sample, similar observation of this compound have also reported earlier on various other homeotropic alignment layers [13, 16]. The molecular structure of compound C2 is shown in Figure 7.2(a). C2 has hockey-stick shape and exhibits following phase transitions: SmX 97°C SmC_a 110.5°C SmA 114.5°C N 123.5°C I. It exhibits positive dielectric anisotropy of $\Delta\epsilon \sim 1.6$ at $T_{NI} - T = 4^\circ$. The synthesis [17] and measurements of physical properties [18] of this compound has already been reported. The photomicrographs of planar and homeotropic alignment of hockey-stick shape liquid crystal is shown in Figure 7.2(b) and Figure

Compound C1



Cr. 77.8°C SmC 109.1°C N 173.4°C I

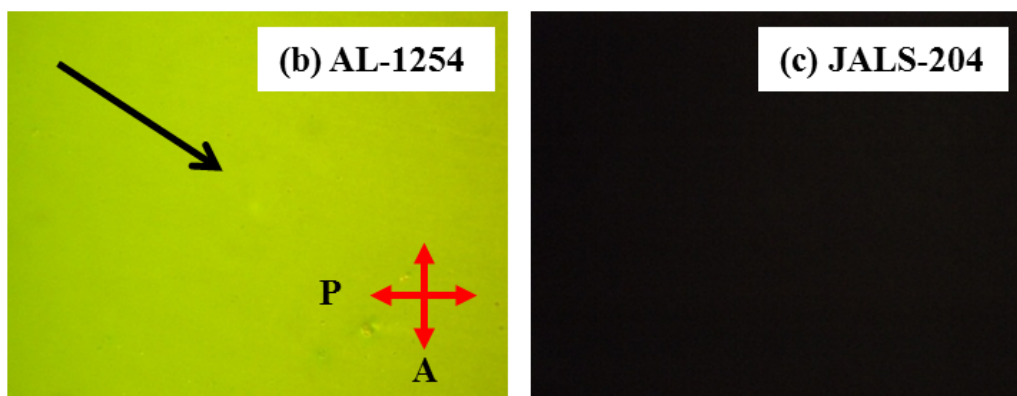
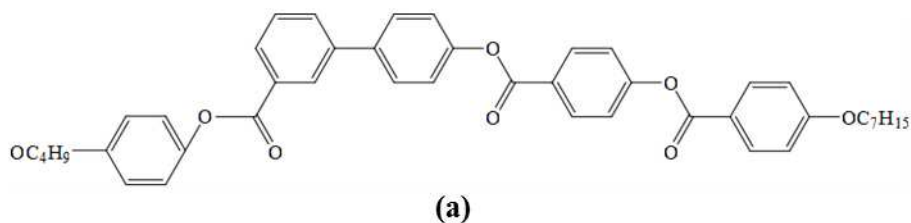


Figure 7.1: (a) Molecular structure and phase transition temperatures of compound C1 ($\Delta\epsilon > 0$). Textures observed in (b) planar and (c) homeotropic cells at a temperature 170°C. An arrow in Figure (b) denotes the rubbing directions. Cell thickness; 6.9 μm and 8 μm for planar and homeotropic cells respectively.

7.2(c). Uniform planar and dark homeotropic states were observed in planar and homeotropic cells respectively. The molecular structure of compound

7.3 Results and Discussion

Compound C2



SmX 97.0°C SmCa 110.5°C SmA 114.5°C N 123.5°C I

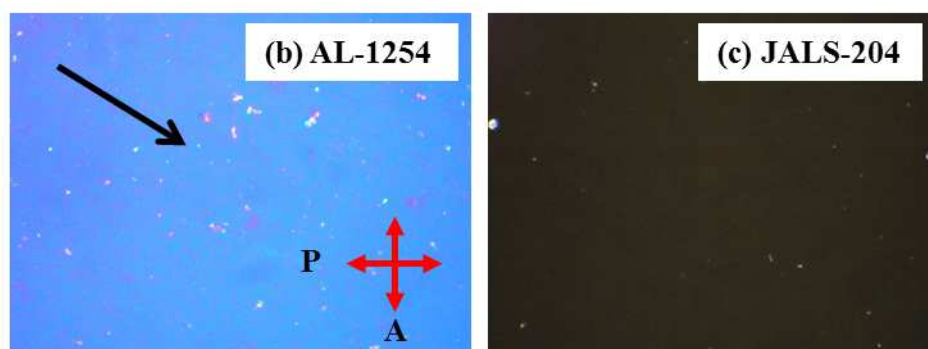
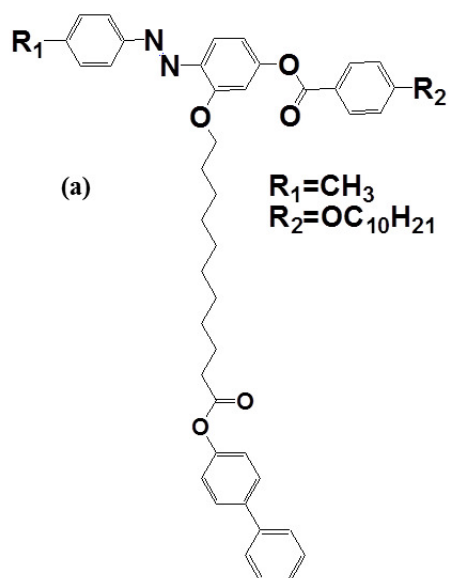


Figure 7.2: (a) Molecular structure and phase transition temperatures of compound C2 ($\Delta\epsilon > 0$) with hockey-stick shaped molecule. Textures observed in (b) planar and (c) homeotropic cells at a temperature 120 °C. An arrow in Figure (b) denotes the rubbing directions. Cell thickness; 7.1 μm and 4.2 μm for planar and homeotropic cells respectively.

C3 is shown in Figure 7.3(a). It is composed of branched molecules and has following phase transitions: Cr 90°C SmA 108°C N 128°C I. The chemical structure of this compound is shown in Figure 7.3(a). It exhibits positive dielectric anisotropy of $\Delta\epsilon \simeq 0.9$ at $T_{NI} - T = 4^\circ$ [19]. The molecule appears to be T-shaped though the optimized structure of a single molecule shows

Compound C3



Cr 90°C SmA 108°C N 128°C I

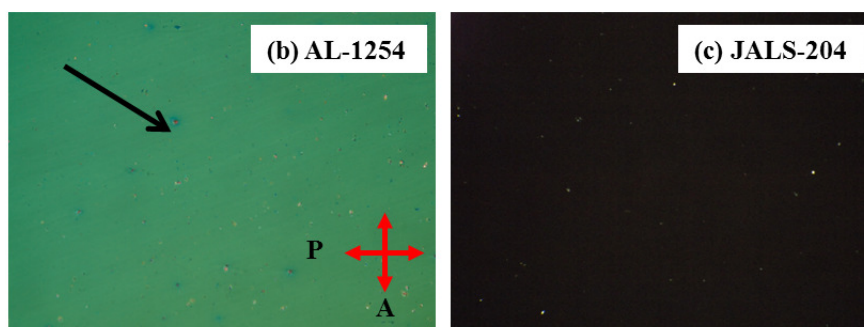
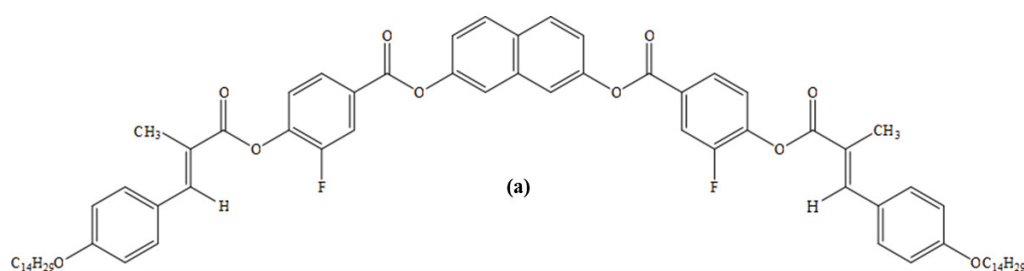


Figure 7.3: (a) Molecular structure and phase transition temperatures of compound C3 ($\Delta\epsilon > 0$) with branched (T-shaped) molecules. Textures observed in (b) planar and (c) homeotropic cell at a temperature 117°C. An arrow in Figure (b) denotes the rubbing direction. Cell thickness: 5.2 μm and 6 μm for planar and homeotropic cells respectively.

7.3 Results and Discussion

that the different parts of the molecule are not in the same plane [19]. The photomicrographs of planar and homeotropic alignment of compound C3 on respective alignment layers are shown in Figure 7.3(b) and 7.3(c). It also shows good planar and homeotropic alignment in cells.

Compound C4



Cr 99.6°C B₂ 114.5°C N 119.5°C I

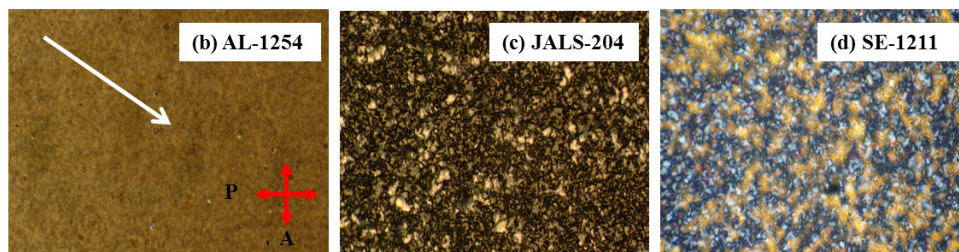
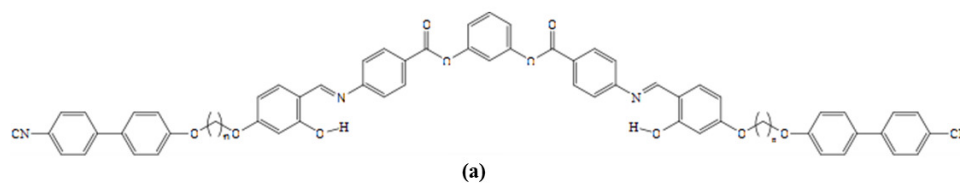


Figure 7.4: (a) Molecular structure and phase transition temperatures of compound C4 ($\Delta\epsilon < 0$). Textures observed in (b) planar and (c),(d) homeotropic cells at a temperature 117°C. An arrow in Figure (b) denotes the rubbing directions. Cell thickness: 5.4 μm for planar and 5.7, 5.3 μm for homeotropic cells respectively.

Textures obtained in planar and homeotropic cells for bent-core liquid crystal with negative dielectric anisotropy ($\Delta\epsilon = \epsilon_{\parallel} - \epsilon_{\perp} < 0$) are shown in Figure 7.4 to Figure 7.6. The chemical structure of compound C4 is shown in Figure 7.4(a). The compound C4 has following phase transitions: Cr 99.6°C B₂ 114.5°C N 119.5°C I. The dielectric anisotropy of C4 is $\Delta\epsilon \simeq -1$ at

Compound C5



Cr 139.3°C M 157.4°C N 211.7°C I

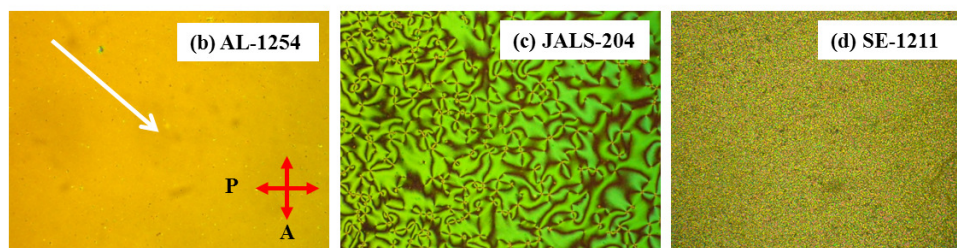


Figure 7.5: (a) Molecular structure and phase transition temperatures of compound C5 ($\Delta\epsilon < 0$). Texture observed in (b) planar and (c), (d) homeotropic cells at a temperature 207°C. An arrow in Figure (b) denotes the rubbing direction. Cell thickness: 5.3 μm for planar and 4.5, 5 μm for homeotropic cells respectively.

$T_{NI} - T = 3^\circ$ [9]. Uniform planar alignment of director is observed in planar cells as shown in Figure 7.4(b). In homeotropic cells as shown in Figure 7.4(c) and 7.4(d) the textures appear mostly dark and exhibits no schlieren texture suggesting that the sample is partially homeotropic. The molecular structure of compound C5 is shown in Figure 7.5(a). It has a larger number of phenyl rings. It exhibits following phase transition: Cr 139.3°C M 157.4°C N 211.7°C I, where M denotes unidentified smectic phase. It exhibits high temperature nematic phase and no Fredericksz transition (upto a frequency 1000 KHz) was observed in the nematic phase in a planar cell. It suggests that the dielectric anisotropy of C5 is negative. The director is uniformly aligned in a planar cell as shown in Figure 7.5(b) whereas no homeotropic

7.3 Results and Discussion

alignment is observed in homeotropic cells as shown in Figure 7.5(c) and 7.5(d).

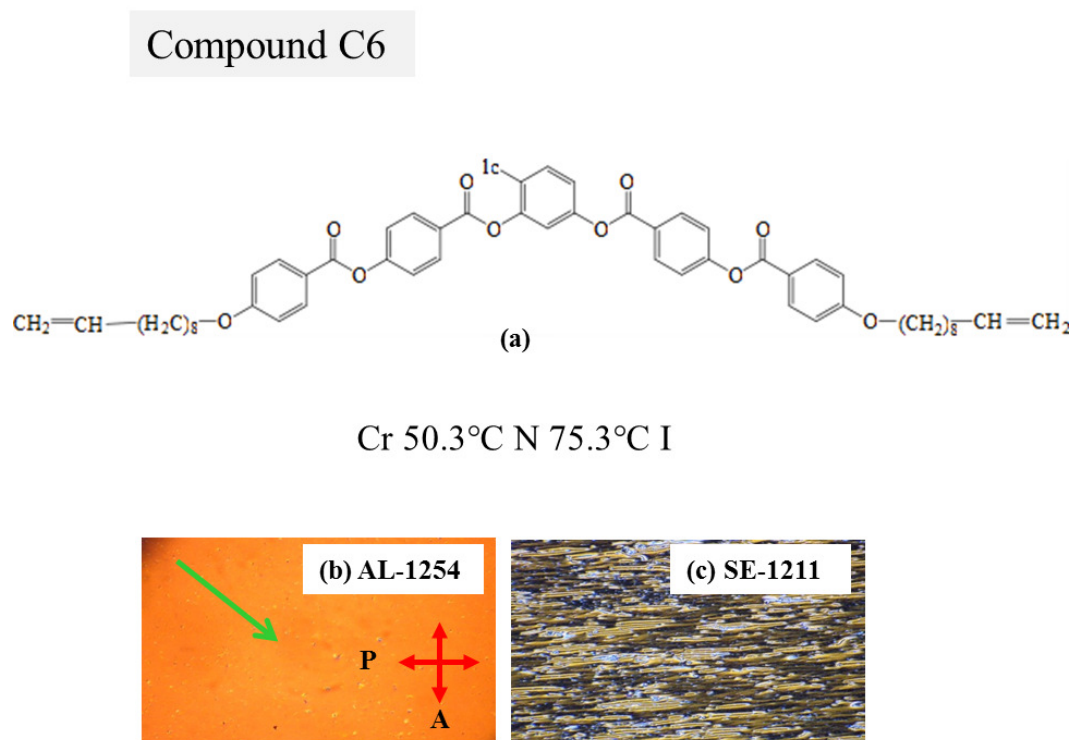


Figure 7.6: a) Molecular structure and phase transition temperatures of the compound C6 ($\Delta\epsilon < 0$). Textures observed in (b) planar and (c) homeotropic cell at 72°C. Arrow in Figure (b) denote the rubbing direction. Cell thickness: 7.1 μm for planar and 5.2 μm for homeotropic cells respectively.

We have also studied a bent-core nematic liquid crystal (C6) with phase sequence: Cr 50.3°C N 75.3°C I. The chemical structure of compound C6 is presented in Figure 7.6(a). It is a characterized bent-core nematic liquid crystal which has no higher order liquid crystalline phase at lower temperature [2–4, 20, 21]. It shows uniform planar alignment in a planar cell and as shown in Figure 7.6(b). No homeotropic alignment is observed in cells coated with SE-1211 as shown in Figure 7.6(c). In JALS-204 coated cells initially it shows a good homeotropic alignment up to 70°C when the sample is cooled

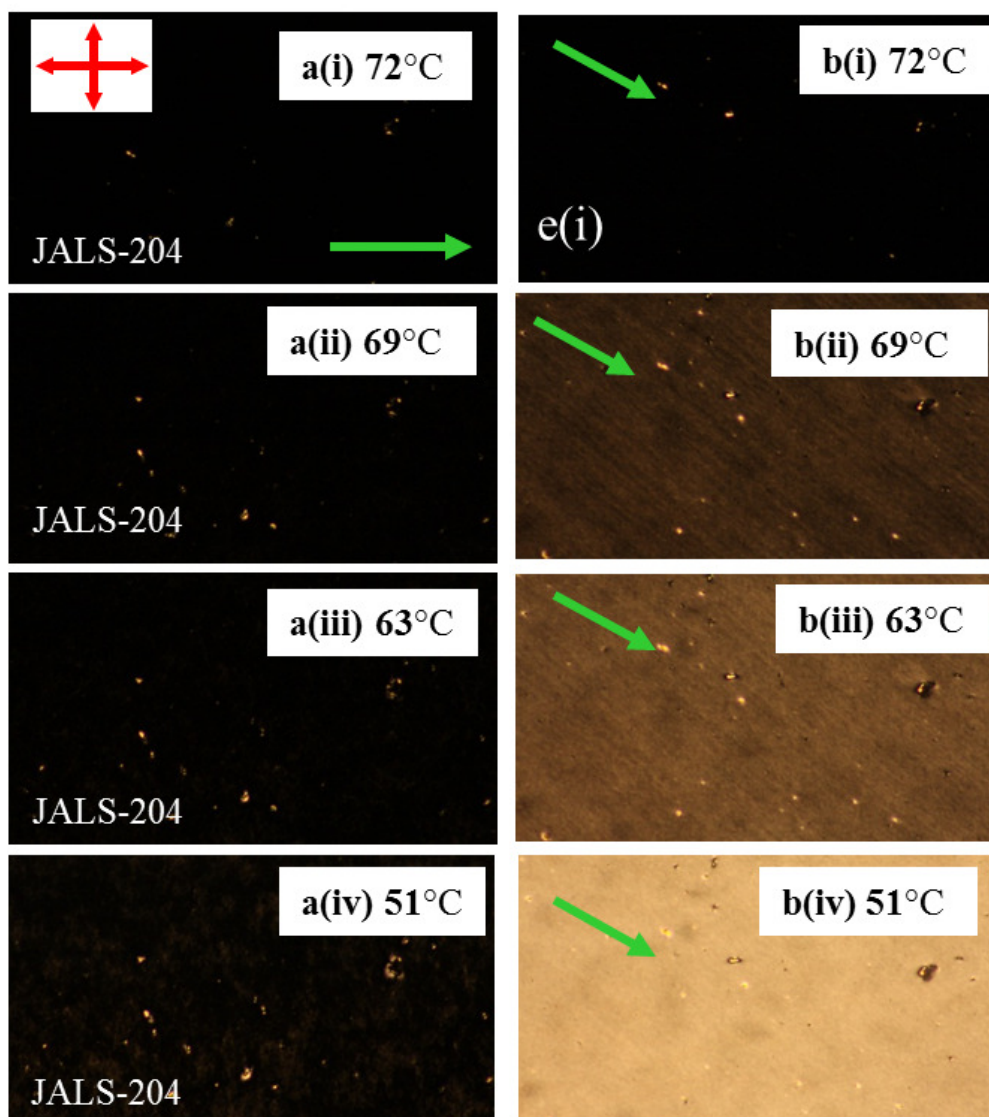


Figure 7.7: Textures observed in homeotropic cell (JALS-204) at various temperatures when rubbing direction is parallel (a(i)-a(iv)) and rotated by 45° (b(i)-b(iv)) with respect to the polarizer. Arrows in the Figure denote the rubbing direction. Cell thickness: $5.2\mu\text{m}$.

from the isotropic phase. The homeotropic alignment is shown in Figure 7.7(d). This compound exhibits continuous anchoring transition as it is cooled down further and finally becomes almost planar at 51°C as shown in Figure

7.3 Results and Discussion

7.7(a(i)-(iv)&b(i)-b(iv)). Similar continuous anchoring transition of calamitic nematic mixture (E7) on perfluoropolymer was reported by Patel *et al.* [22]. Thus from the texture observation of the compounds studied it appears that unconventional nematic liquid crystals show planar alignment irrespective of the sign of the dielectric anisotropy. The compound with positive dielectric anisotropy can be aligned uniformly in homeotropic cells whereas bent-core nematic materials with negative dielectric anisotropy in general cannot be aligned in homeotropic cells.

There are several interfacial forces that are responsible for the orientation of the liquid crystal molecules on the substrate surface such as steric interaction, short range dipolar and long range Van der Waals interactions. Steric interaction prefers planar alignment of the director [23, 24]. Long range Van der Waals interaction prefers the large polarisability direction (here the bow axis denoted by P in Figure 7.8) and is parallel to the substrate surface [25, 26]. Thus both the steric and Van der Waals interactions in bent-core liquid crystals always prefer planar alignment of the director. The short range dipolar interaction tends to make the dipoles normal to the interface to maximize their interaction with the charges at the surface and have opposite alignment effect depending on the strength and orientation of the resultant dipole moment with respect to the long molecular axis. It tends to align the long molecular axis (P) perpendicular to the surface when the direction of the resultant dipole moment (denoted by D in Figure 7.8(a)) is parallel to P. On the other hand it tends to orient the bow axis (P) parallel to the substrate when the direction of dipole moment (D) is perpendicular to P. In case of compounds with $\Delta\epsilon > 0$, D is parallel to P and has opposite alignment effect. However, if the dipolar interaction is relatively stronger than that of long range Van der Waals interaction it can lead to homeotropic alignment of the bent-core molecules as schematically shown in Figure 7.8(c). In case of bent-core compounds with $\Delta\epsilon < 0$, D is parallel to arrow axis i.e., almost perpendicular to P (Figure 7.8(b)) and both D and P have similar alignment effect i.e., planar alignment of the molecules as shown in Figure 7.8(d). As a result dielectrically-negative-type bent-core nematic compounds in general do not exhibit homeotropic alignment. The anchoring transition of the compound

shown in Figure 7.6 can be considered as a result of competition between these two major interactions as discussed above. Since most of the bent-core liquid crystals possess several phenyl rings, the polarisability is large and is strongly temperature dependent. Because of increased polarisability at lower temperatures the Van der Waals interaction can dominate over the dipolar interaction and an anchoring transition can occur. Compound C6

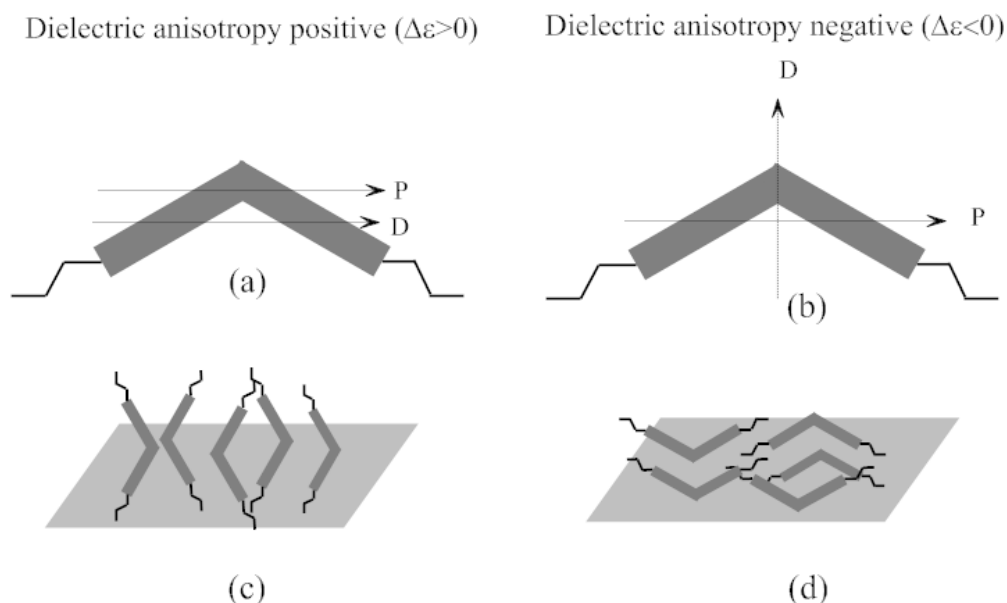


Figure 7.8: Schematic representation of bent-core molecules. The direction of resultant dipole moment and the large polarisability directions are denoted by D and P respectively. (a) Both D and P are parallel in materials with $\Delta\epsilon > 0$ (b) D and P are mutually perpendicular in materials with $\Delta\epsilon < 0$. (c) Homeotropic alignment of the director with $\Delta\epsilon > 0$. (d) planar alignment of the director with $\Delta\epsilon < 0$.

in Figure 7.7 shows unstable homeotropic state (from 75.3°C to 70°C) in the sense that below 70°C it exhibits continuous anchoring transition to planar state. We measured anchoring energy in homeotropic state of this compound. Retardation (R) and capacitance (C) were measured simultaneously to measure the anchoring energy (A) at a particular temperature.

7.3 Results and Discussion

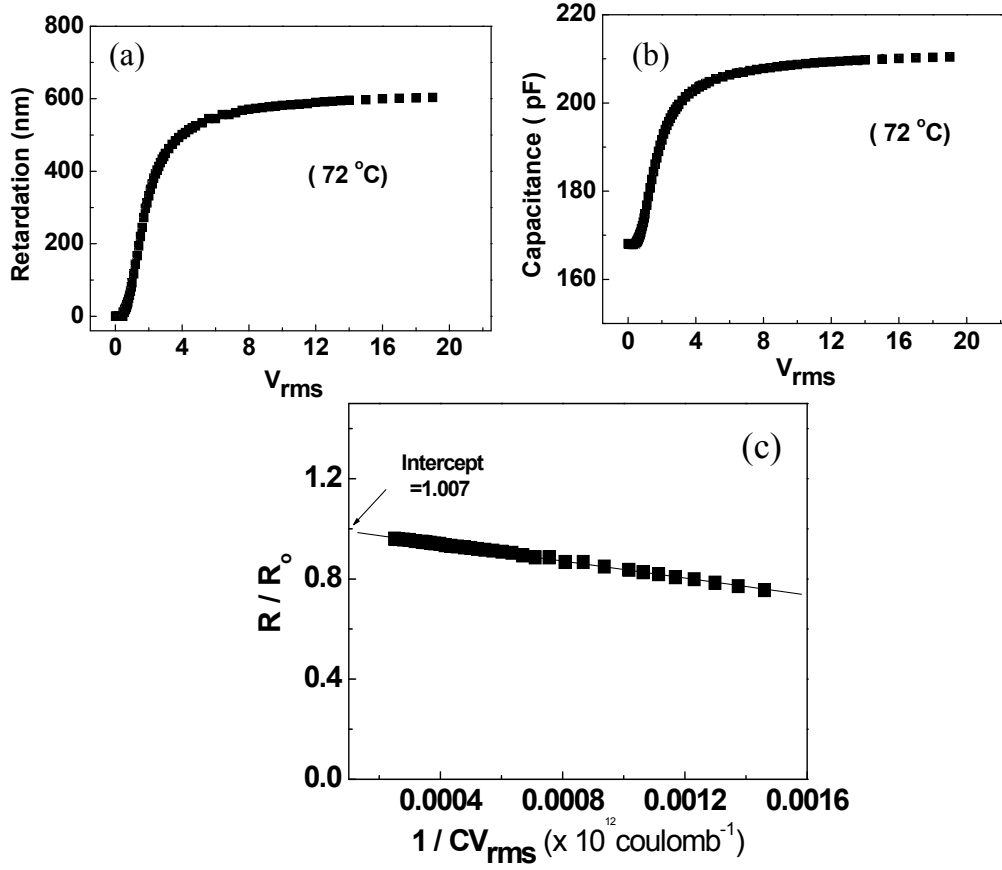


Figure 7.9: a) Retardation as a function of applied voltage measured in the homeotropic cell (at 72°C) (b) sample capacitance as a function of applied voltage at 72°C. (c) normalized retardation R/R_o as a function of $1/CV_{rms}$ at 72°C. Continuous line is the theoretical fit to equation 7.1. Cell thickness; 6.1 μm .

The variation of retardation and capacitance as a function of applied voltage is shown in Figure 7.9(a) and 7.9(b) respectively. Below the Freedericksz threshold voltage ($V_{th} = 0.47\text{V}$) the sample retardation is zero (homeotropic state) and the director tilts as the voltage is increased and finally becomes almost planar at higher voltages. The bend elastic constant of this compound was calculated by using the relation $K_{33} = (V_{th}/\pi)^2 \Delta\epsilon\epsilon_o$ where $\Delta\epsilon$ is the dielectric anisotropy. At 72°C, $\epsilon_{||} = 5.5$ and $\epsilon_{\perp} = 6.9$, which was measured

from the extrapolation of capacitance (C) with $1/V_{rms}$. The estimated K_{33} from the present Freedericksz threshold measurement is $\simeq 0.3 \times 10^{-12}$ N and comparable in magnitude with the reported values [27]. Similar value of K_{33} near the nematic-isotropic transition was also reported in other bent-core nematic liquid crystals [6]. Variation of the normalized retardation (R/R_o) as a function of $1/CV_{rms}$ is shown in Figure 7.9(c). The experimental data was fitted with the theoretical equation 7.1 by using a least square fitting method to estimate the intercept. The obtained anchoring energy A found to be $\sim 1.4 \times 10^{-5}$ J/m² and is significantly low compared to many known calamitic liquid crystals. The anchoring transition observed in this compound could be attributed to the low anchoring energy.

7.4 Conclusions

We have studied alignment properties of some bent-core, hockey-stick and T-shaped nematic liquid crystals with both positive and negative dielectric anisotropy. We found that these unconventional nematic liquid crystals with both positive and negative dielectric anisotropy can be aligned easily in planar cells whereas bent-core materials with negative dielectric anisotropy in general cannot be aligned homeotropically. The experimental results are explained by considering the steric interaction, short range dipolar and the Van der Waals interactions. The polar anchoring energy of a material with negative dielectric anisotropy is very small and perhaps lead to the anchoring transition as observed. Further it will be interesting to study and measure the surface related properties of bent-core nematic compounds with different shapes on various other alignment layers.

References

- [1] C. Tschierske and D. J. Photinos, “Biaxial nematic phases”, *J. Mater. Chem.*, **20**, 4263 (2010).

REFERENCES

- [2] D. Wiant, J. T. Gleeson, N. Eber, K. F. Csorba, A. Jakli and T. Toth-Katona, “Nonstandard electroconvection in a bent core nematic liquid crystal”, *Phys. Rev. E* **72**, 041712 (2005).
- [3] S. Tanaka, S. Dhara, B. K. Sadashiva, Y. Shimbo, Y. Takanishi, F. Araoka, K. Ishikawa and H. Takezoe, “Alternating twist structures formed by electroconvection in the nematic phase of an achiral bent core molecule”, *Phys. Rev. E* **77**, 041708 (2008).
- [4] J. Hardeen, B. Mbanga, N. Eber, K. Fodor-Csorba, S. Sprunt, J. T. Gleeson and A. Jakli, “Giant flexoelectricity of bent core nematic liquid crystals”, *Phys. Rev. Lett.*, **97**, 157802 (2006).
- [5] S. Dhara, F. Araoka, M. Lee, K. V. Le, L. Guo, B. K. Sadashiva, K. Song, K. Ishikawa and H. Takezoe, “Kerr constant and third-order nonlinear optic susceptibility measurements in a liquid crystal composed of bent shaped molecules”, *Phys. Rev. E* **78**, 050701R (2008).
- [6] P. Sathyanarayana, M. Mathew, Q. Li, V. S. S. Sastry, B. Kundu, K. V. Le, H. Takezoe and S. Dhara, “Splay bend elasticity of a bent core nematic liquid crystal”, *Phys. Rev. E* **81**, 010702R (2010).
- [7] E. Dorjgotov, K. F. Csorba, J. T. Gleeson, S. Sprunt and A. Jakli, “Viscosities of a bent core nematic liquid crystal”, *Liq. Cryst.*, **35**, 149 (2008).
- [8] P. Sathyanarayana, T. Arun Kumar, V. S. S. Sastry, M. Mathews, Q. Li, H. Takezoe, and S. Dhara, “Rotational viscosity of a bent core nematic liquid crystal”, *Appl. Phy. Exp.*, **3**, 091702 (2010).
- [9] K. V. Le, S. Dhara, B. K. Sadashiva, Y. Takanishi and H. Takezoe, “Characterization of nematic phase of banana liquid crystal”, *Jpn. J. Appl. Phys.*, **45**, L1013 (2006).
- [10] L. A. Madsen, T. J. Dingemans, M. Nakata and E. T. Samulski, “Thermotropic biaxial nematic liquid crystals”, *Phys. Rev. Lett.*, **92**, 145505 (2004).

REFERENCES

- [11] J. Matraszek, J. Mieczkowski, J. Szydłowska and E. Gorecka, “Nematic phase formed by banana shaped molecules”, *Liq. Cryst.*, **27**, 429 (2000).
- [12] X. Nie, Y. H. Lin, T. X. Wu, H. Wang, Z. Ge and S. T. Wu, “Polar anchoring energy measurement of vertically aligned liquid crystal cells”, *J. Appl. Phys.*, **98**, 013516 (2005).
- [13] K. V. Le, M. Mathews, M. Chambers, J. Harden, Q. Li, H. Takezoe and A. Jakli, “Electro-optic technique to study biaxiality of liquid crystals with positive dielectric anisotropy: The case of a bent-core material”, *Phys. Rev. E* **79**, 030701R (2009).
- [14] H. G. Yoon, S. W. Kang, R. Y. Dong, A. Marini, K. A. Suresh, M. Srinivasarao and S. Kumar, “Nematic biaxiality in a bent core material”, *Phys. Rev. E* **81**, 051706 (2010).
- [15] P. Sathyanarayana, T. Arun Kumar, V. S. S. Sastry, M. Mathews, Q. Li, H. Takezoe and S. Dhara, “Rotational viscosity of a bent core nematic liquid crystal”, *Appl. Phys. Exp.*, **3**, 091702 (2010).
- [16] B. Senyuk, H. Wonderly, M. Mathews, Q. Li, S. V. Shiyankovskii, and O. D. Lavrentovich, “Surface alignment, anchoring transitions, optical properties, and topological defects in the nematic phase of thermotropic bent-core liquid crystal A131”, *Phys. Rev. E* **82**, 041711 (2010).
- [17] S. Radhika, H. T. Srinivasa and B. K. Sadashiva, “Anticlinic smectic C phase in new and novel five ring hockey stick shaped compounds”, *Liq. Cryst.*, **38**, 785 (2011).
- [18] P. Sathyanarayana, S. Radhika, B. K. Sadashiva and S. Dhara, “Structure property correlation of a hockey stick shaped compound exhibiting N-SmA-SmC_a phase transitions”, *Soft Matt.*, **8**, 2322 (2012).
- [19] P. Sathyanarayana, M. C. Varia, A. K. Prajapati, B. Kundu and S. Dhara, “Splay bend elasticity of a nematic liquid crystal with T-shaped molecules”, *Phys. Rev. E* **82**, 050701R (2010).

REFERENCES

- [20] K. F. Csorba, A. Vajda, G. Galli, A. Jakli, D. Demus, S. Holly, and E. G. Baitz, “Ester type banana shaped monomers and investigations of their electro-optical properties”, *Macromol. Chem. Phys.*, **203**, 1556 (2002).
- [21] G. G. Nair, C. A. Bailey, S. Taushanoff, K. F. Csorba, A. Vajda, Z. Varga, A. Bota and A. Jakli, “Electrically tunable color by using mixtures of bent core and rod shaped molecules”, *Adv. Mater.*, **20**, 3138 (2008).
- [22] J. S. Patel and H. Yokoyama, “Continuous anchoring transition in liquid crystals”, *Nature (London)*, **362**, 525 (1993).
- [23] H. Kimura, “Statistical theory of surface tension and molecular orientations in nematic liquid crystals. III. On hard flat walls”, *J. Phys. Soc. Jpn.*, **62**, 2725 (1993).
- [24] E. D. Violette and P. G. de Gennes, “Local Frederiks transition near a solid/nematic interface”, *J. de Phys. Lett.*, **36**, L255 (1975).
- [25] E. D. Violette and P. G. de Gennes, “Effects of long range van der Waals forces on the anchoring of a nematic fluid at an interface”, *Colloid. Interface Sci.*, **57**, 403 (1976).
- [26] C. Chen, P. J. Bos and J. E. Anderson, “Anchoring transitions of liquid crystals on SiO_x ”, *Liq. Cryst.*, **35**(4), 465 (2008).
- [27] M. Majumdar, P. Salamon, A. Jakli, J. T. Gleeson and S. Sprunt, “Elastic constants and orientational viscosities of a bent core nematic liquid crystal”, *Phys. Rev. E* **83**, 031701 (2010).

List of Publications

1. **T. Arun Kumar**, K. V. Le, H. Takezoe and S. Dhara, “Anchoring transition in a nematic liquid crystal doped with chiral agents” (in preparation).
2. **T. Arun Kumar**, V. S. S. Sastry, K. Ishikawa, H. Takezoe, N. V. Madhusudana and S. Dhara, “Effect of Electric Field on Defects in a Nematic Liquid Crystal with Variable Surface Anchoring”, *Liq. Cryst.*, **38**, 971(2011).
3. **T. Arun Kumar**, K. V. Le, J. K. Kim, H. Takezoe and S. Dhara, “Alignment of Unconventional Nematic Liquid Crystals”, *Liq. Cryst.*, **38**, 917(2011).
4. **T. Arun Kumar**, H. Takezoe and S. Dhara, “Perfluoropolymer as Planar Alignment Layer for Liquid Crystal Mixtures”, *Jpn. J. Appl. Phys.*, **50**, 040203 (2011).
5. P. Sathyanarayana, **T. Arun Kumar**, V. S. S. Sastry, M. Mathews, Q. Li, H. Takezoe and S. Dhara, “Rotational Viscosity of a Bent-Core Nematic Liquid Crystal”, *Appl. Phys. Exp.*, **3**, 091702 (2010).
6. **T. Arun Kumar**, P. Sathyanarayana, V. S. S. Sastry, H. Takezoe, N. V. Madhusudana and S. Dhara, “Temperature and electric-field-induced inverse Freedericksz transition in a nematogen with weak surface anchoring”, *Phys. Rev. E* **82**, 011701 (2010).
7. S. Dhara, **T. Arun Kumar**, K. Ishikawa and H. Takezoe, “Thermotropic uniaxial nematic liquid crystal with $\pm 1/2$ strength disclinations: defect-antidefect production and correlation”, *J. Phys. Cond. Matt.*, **21**, 505103 (2009).

Conferences attended:

International

- 23rd International Liquid Crystal Conference (ILCC), 11th – 16th July 2010, Krakow, Poland.

National

- 16th National Conference on Liquid Crystals (NCLC), 26th – 28th Oct 2009, Lucknow, India.
- 15th National Conference on Liquid Crystals (NCLC), 13th – 15th Oct 2008, Bangalore, India.

Poster Presentations:

International

- A poster entitled "The Effect of Electric Field on the Anchoring Transition of a Nematic liquid Crystal on a Perfluoropolymer Treated Surface" was presented at 23rd ILCC-2011, Krakow, Poland.

National

- A poster entitled "Effect of Electric Field on Discontinuous Anchoring Transition in a Thermotropic Nematic Liquid Crystal" was presented at 16th National Conference on Liquid Crystals (NCLC) 2009, Lucknow, India.

Curriculum Vitae

Tatipamula Arun Kumar

C/O Dr Surajit Dhara
School of Physics
University of Hyderabad
Hyderabad, India 500 046
Email: tp.arunk@gmail.com

Education:

- Pursuing Ph.D. in Physics on "Study of Perfluoropolymer as an Alignment Layer for Nematic Liquid Crystals", since 2006, School of Physics, University of Hyderabad.
- M.Sc. Physics with First class, May 2003, Nizam College, Hyderabad, Andhra Pradesh, India.

Additional Research Experience:

Visited Prof. Hideo Takezoe laboratory, as a foreign young researcher in the Department of Organic and Polymeric Materials, Tokyo Institute of Technology under Global Center of Excellence (G-COE) program, Japan during the period 25th September to 23rd December, 2011.

Teaching Experience:

Assistant Professor of Physics for

- DRK Institute of Technology, Dec 2005-July 2006, Hyderabad.
- Royal College of Engineering, Feb 2004-Nov 2005, Medak.
- Bapuji Engineering College, July 2003-Feb 2004, Nirmal, Adilabad.

Experimental skills:

- Hands on experience in using Polarizing Optical microscopes (Nikon and Olympus)
- Photolithography to make patterns on ITO substrates
- Familiar with measurement of anchoring energy, rotational viscosity and pretilt angle.
- Atomic Force Microscope (SII Inc.) to study the polyimide and per-fluoropolymer treated surfaces.

Personal details:

Date of Birth : 25thFeb, 1980

Sex : Male

Nationality : Indian

Languages known: English, Hindi and Telugu

Computer skills : FORTRAN, MATHEMATICA and LabView

References:

- Dr. Surajit Dhara
School of Physics
University of Hyderabad
P.O. Central University, Hyderabad
Andhra Pradesh, India 500 046
Email: sdsp@uohyd.ernet.in
Phone No: 040-66794331
- Prof. V. S. S. Sastry
School of Physics

University of Hyderabad
P.O. Central University, Hyderabad
Andhra Pradesh, India 500 046
Email: vssssp@uohyd.ernet.in

- Prof. N. V. Madhusudana
INSA Scientist
Soft Condensed Matter Group
Raman Research Institute
C. V. Raman Avenue
P. O. Sadashivanagar
Bangalore 560 080-India.
Extension : 350
Email : nvmadhu@rri.res.in
- Prof. Hideo Takezoe
Department of Organic and Polymeric Materials
Tokyo Institute of Technology, Japan.
Tel: 03-5734-2436, Fax: 03-5734-2876
E-mail: takezoe.h.aa@m.titech.ac.jp